

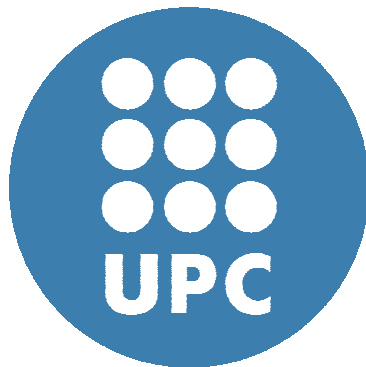
UNIVERSITAT POLITÈCNICA DE CATALUNYA

**Escola Tècnica Superior d'Enginyeria de
Telecomunicació de Barcelona**

ENGINYERIA DE TELECOMUNICACIÓ

Proyecto Fin de Carrera

**Design, Fabrication and Characterization of
Metal-Semiconductor Solar Cells**



Tutor:

Prof. Santiago Silvestre

Estudiante:

Elio Tirrito

Marzo 2011

CONTENTS

Chapter 1

INTRODUCTION	4
<i>Figure references chapter 1</i>	9

Chapter 2

MS JUNCTION, MS SOLAR CELL AND ITS PARAMETERS AND SIMULATION

2.1 Introduction to the chapter 2	10
2.2 Energy level and energy band.....	10
2.3 The Metal-Semiconductor junction	12
2.4 W depending on C	18
2.5 From the MS junction to the MS solar cell	20
2.6 Main parameters of a solar cell.....	24
2.6.1 <i>Basic concepts and definitions</i>	24
2.6.2 <i>Dark current and photocurrent</i>	26
2.6.3 <i>Quantum efficiency and spectral response</i>	33
2.6.4 <i>Solar cell efficiency</i>	33
2.7 PSpice simulation.....	35
<i>Figure references chapter 2</i>	45

Chapter 3

PROCESS EQUIPMENTS AND TECHNIQUES

3.1 Introduction to chapter 3	46
3.2 Sputtering	46
3.3 Photolithography	50
3.4 Evaporator	52
3.5 Laser	54
<i>Figure references chapter 3</i>	58

Chapter 4

EXPERIMENTAL MEASUREMENTS AND PROCESS DEVELOPMENT

4.1 Introduction to the chapter 4	59
4.2 The solar cell structure	59
4.3 ITO: general concepts and experimental measurements.....	61
4.3.1 <i>Definition and main characteristics of ITO</i>	61
4.3.2 <i>ITO deposition and experimental results</i>	62
4.4 Ohmic contact.....	71
4.4.1 <i>Definition of the main parameters and Au/Zn ohmic contact</i>	71
4.4.2 <i>Experimental process of deposition</i>	72
4.4.3 <i>Method of measurement and results</i>	73
4.5 Cleaning and passivation	83
4.6 Process P1.....	89
4.6.1 <i>Process description</i>	89
4.6.2 <i>V-I Characteristic of P1 cell</i>	92
4.7 Process P2.....	95
4.7.1 <i>Process variation</i>	95
4.7.2 <i>V-I Characteristic of P2 cell</i>	98
<i>Figure references chapter 4</i>	103

Chapter 5

CONCLUSION104

References109

1.

INTRODUCTION AND CONTEXT OF THE WORK

The air pollution problem always acquires more importance, both in public opinion and in government investment programs. Indeed, in these last years, the green power solutions market has been grown with an exponential trend in spite of the international economical crisis. Among the different renewable energy sources, one of the most important certainly is the solar cell. It cannot probably solve alone the air pollution problem, but has to play a central role in a mix of different green energy sources, to meet the entire populations energy demand without polluting. Investigation in different type of new and more efficient solar cells is on, but there is a question limiting the skyline of these researches carried out by William Bradford Shockley and Hans-Joachim Queisser in 1961, known as the Shockley-Queisser limit [1]. According with it, the maximum theoretical efficiency achievable by a solar cell is 40.7% (assuming a p-n junction and the band gap of Silicon, 1.1 eV). In other words, of the whole sun power arriving on the earth's surface (1,000 W/m² in AM1.5 sunlight), only 40.7% is convertible in electric energy by a "perfect"

solar cell. One of the most important contribution to this limit is the impossibility, for a certain material with a certain band gap, to absorb the whole solar radiation spectrum, especially, only the wavelength with energy greater than or equal to the solar cell materials band gap will be absorbed.

Starting from this consideration, researchers thought solutions to overcome this limit. Assumed, as said, that one of the most important problems for solar cell efficiency is in the unique well defined band gap for a given material, a consistent consequence is to direct efforts to find the way for making solar cell with more than one band gap: hence was born the intermediate band solar cell concept [2].

A traditional solar cell, in its simplest form, is made with a n-doped semiconductor and a p-doped semiconductor, forming a p-n junction. Sometimes, one of the two doped semiconductor materials (p or n), is replaced with a metal to finally form a metal-semiconductor junction working in the same way of a p-n junction (important is to underline how, staying metal on the top of the solar cell structure, it has to permit the passage of light through it). The used semiconductor (commonly Silicon or, for more efficient solar cell, GaAs) has a certain band gap that is the distance between its valence band (VB) forming the set of lower energy levels, and its conduction band (CB) forming the set of higher energy levels. Photon arriving from the sun and hitting the solar cell, can pump electrons from valence band toward conduction band. This happens when photon energy is high enough (higher than or equal to the band gap). For photons having an energy higher than the band gap, the exceeded energy is transformed in heat and is not useful to generate power. Photons having an energy lower than the material band gap do not have sufficiently energy to pump electrons till CB, therefore electrons will reach an intermediate position between CB and VB, then falling again toward VB.

As showed in Figure 1.1, in the intermediate band (IB) solar cells an energy level is introduced between CB and VB, therefore, electrons hit by low-power photons, instead of coming back to VB, will be collected in this intermediate energy level. Obviously, the hitting photons must have sufficient energy to enable this event (at least equal to E_H , that is the energy difference between VB and IB). Afterwards, others photons, with energy higher than E_L (energy difference between IB and CB), will carry the collected electrons up to CB,

an impurity can give an efficiency improvement and not simply non-radiative transition. In fact, it is known that impurities introduce trap centers, causing Shockley-Read-Hall (SRH) recombination, hence degrading solar cells efficiency (both radiative and non-radiative recombination affect the efficiency but, while the first one is not generally unavoidable, because is the balance counterpart of the light absorption process, the second one can theoretically be suppressed).

When electrons stay in the CB or in the VB, their charge extends across the whole crystal and, moreover, these electrons are characterized by the same wave function: this is an equilibrium state. When an electron passes to trap centers a certain change in movement is necessary, its wave function change, its charge is concentrated at a point (not staying in CB or VB, but into the band gap) and, since this is no longer an equilibrium state, crystal lattice starts to vibrate seeking a new equilibrium. But when the trap centers raise considerably at the same energy level, electrons are not trapped at a point, but they can move from a trap center to another. In practice, if the trap density increases, an extended state is produced with a wave function unique for all the impurities. In this situation, carriers passing from the CB to the impurity band, will not need a large change in movement preventing strong disequilibrium states, and then, losses.

Despite is not easy to draw an equivalent electronic circuit representing the IB solar cells functioning, the [1] proposes the one shown in Figure 1.2. On the left (the part circled in red) there are three current generators and three diodes. Obviously the generators represent the generated photocurrent, while the diodes represent losses related to recombination phenomena. But photons emitted by these recombination process are not always a loss factor, indeed can occur that some of them can be reabsorbed raising the generated photocurrent. This increasing factor of the photocurrent is represented by generators inside the blue box. The diodes inside the same area, are always connected with recombination processes. In the central part of the figure, there are other current generators inside a green box: they are related with the earlier introduced energy transference mechanism.

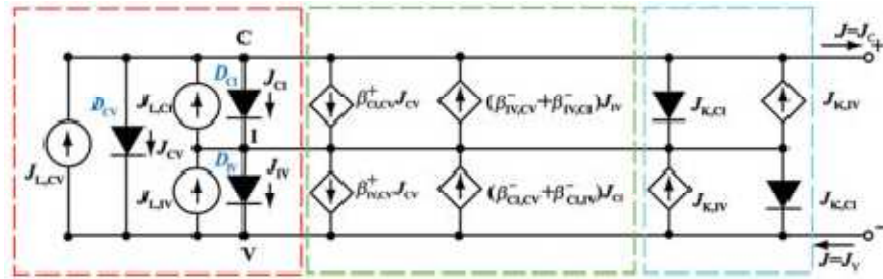


Figure 1.2: equivalent circuit for an IB solar cell.

Different solutions have been proposed to introduce an intermediate band in a solar cell substrate. One of these proposals is the usage of quantum dot structures, with which has been proved it is possible to obtain IBs, but the complexity of this structure probably do not make them easily marketable: the final aim of technologies is to change life styles, without taking the risk of relegate itself to be laboratory stuff. Furthermore, quantum dot solar cell, has been proved to have low efficiency due to different reasons, among which, weak absorption (probably due to the low IB state density) is one of the most important.

In this prospective, another proposed solution was to place intermediate band materials (that generally are compounds) in simple structures, like those ones yet used today. In other words the aim is to use the same structures, but with materials that can efficiently catch more photon wavelengths. The project in which the present work is collocated, follows this research path.

In [11] and [12] some theoretical simulations have been done, using the density functional theory (DFT), to study crystal lattices, with the final aim to find materials suitable to incorporate intermediate bands. In particular two different cells, candidate to host IBs, have been examined: Ga_4As_3Ti and Ga_4P_3Ti . The results of the simulations show as for both Ga_4As_3Ti and Ga_4P_3Ti the IB is actually present.

The project in which the present work is collocated has the final aim to prove experimentally these theoretical concepts and simulations, in particular using Ti impurities in GaAs substrate.

The work, here presented, has just the objective to develop a solar cell structure, suitable to test substrates for proving if they really are intermediate band materials, and than allowing analysis about possible advantages. But it is out of our scope to test IB materials in the developed structure. In spite of that, in this section we have retained useful to contextualize our work, to give a broad idea about their objectives and to make it more understandable on the whole.

In the next chapters, we will introduce first theoretical concepts concerning the developed solar cell structure, afterwards, information about the fabrication process, and eventually the results of our experimental measurements.

Figure references chapter 1

Figure 1.1, 1.2 are from [1].

2.

MS JUNCTION, MS SOLAR CELL AND ITS PARAMETERS AND SIMULATION

2.1 Introduction to the chapter 2

We have already mentioned the way a solar cell works in the introduction chapter, but it is probably advisable to explain it in more detail, that is what we will do in this section. Beyond the theoretical background, we will provide a PSpice simulation to give a broad idea about the typical values concerning solar cell parameters.

2.2 Energy level and energy band

Each atom has some energy levels where electrons move, when two equal atoms are moved close, each quantized energy level splits into two energy levels really close together. If we image to move close hundreds, thousands or more atoms, each energy level will splits in so many energy levels, very close to each other, that we can practically consider them a continuous band: what is formed is an energy band.

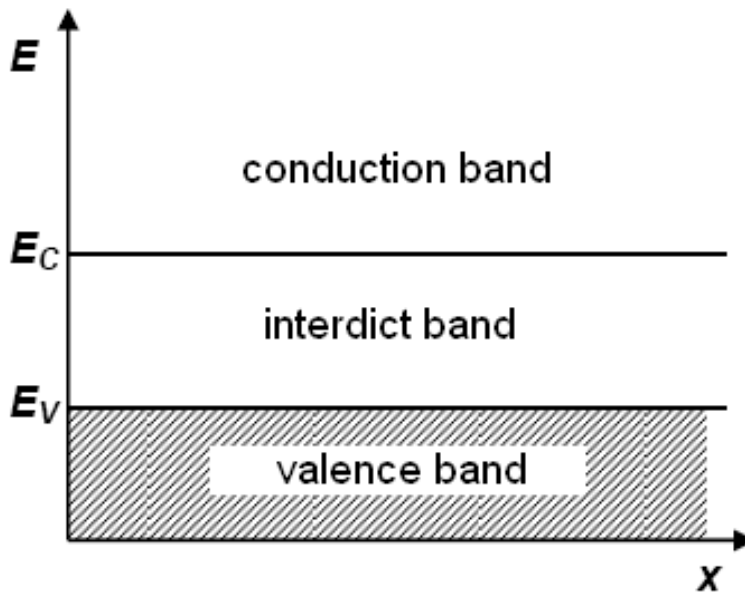


Figure 2.1: energy band in solid material.

In a homogeneous solid, perfectly smooth, without impurities and constituted by a crystal lattice, we call valence band (VB) the last band filled by electrons, and conduction band (CB) the next one, normally empty. The band gap (E_G) is the distance between this two energy bands. It is called interdict band because it is forbidden to electrons.

The Figure 2.1 shows the energy bands described above. E_V is the highest energy level of the valence band, while E_C is the lowest energy level of the conduction band. As said, electrons generally stay at the valence band but, when they receive sufficient energy, they can overcome the interdict band reaching the conduction band. It is well-known that the process of electrical conduction in a solid material consists of a motion of electrons in the direction of the external electric field, but electrons can only move in conduction band. With regard to the last statement, it is important to underline that the energy band structure is different in insulator, conductor and semiconductor materials. In insulators E_G is really high, so that it is pretty improbable (or even impossible) that an electron can pass to the conduction band. Vice versa in a conductor, VB and CB are partially overlapped, so that electrons can easily reach the conduction band with a low quantity of energy. The intermediate case is that one of the semiconductors, in which VB and CB are not overlapped, but the distance is not excessively high (about 1 eV). In a semiconductor with an electric field externally applied, conduction is only possible when an adequate energy (higher than E_G) is provided to the electrons staying in the valence band.

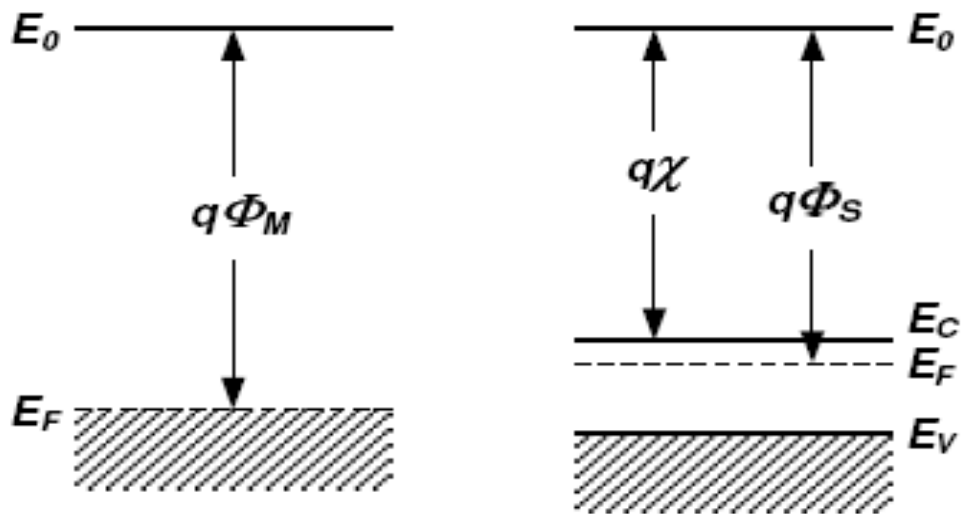


Figure 2.2: energy band in metals (left) and in semiconductors (right).

When an electron passes to the CB, leaves a hole in the VB, and when an electric field is externally applied, the electron in the CB will move in the direction of it, while the hole will move in the opposite direction. Obviously it is not the hole that moves, but its motion is the result of the VB electrons' motion. They go in the electric field direction, filling holes and creating new holes, so that the external feeling is that holes are moving in the opposite direction of the electric field.

2.3 The Metal-Semiconductor junction

The "Fermi level" is the highest energy level where electrons are present at absolute zero temperature. More generally, at temperatures different than zero, it is the energy level having 50% of probability to be filled by an electron. When a semiconductor is doped, E_F changes its position. In fact, for n-doped materials, electron density is higher than hole density, therefore, higher is the probability to meet an electron: E_F goes nearer E_C ; for p-doped materials, electron density is lower than hole density, therefore, lower is the probability to meet an electron: E_F goes nearer E_V .

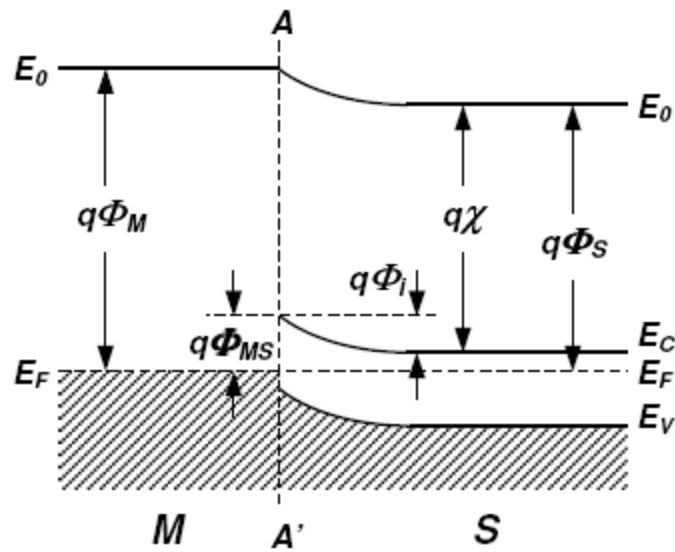


Figure 2.3: energy band in metals (left) and in semiconductors (right).

E_0 , that we call reference level, is that energy level for which the difference between E_0 and E_F gives the extraction work. The extraction work is the minimum energy needed to remove an electron from a solid. In the Figure 2.2 is shown the energy band structure of a semiconductor (on the right) and a metal (on the left). In the figure the extraction work of the metal is called $q\phi_M$, the extraction work of the semiconductor is called $q\phi_S$, and the electronic affinity, given by the difference between E_0 and E_C , is called $q\chi$. Among the two last mentioned magnitudes ($q\phi_S$ and $q\chi$), electronic affinity is the only one to be independent of the doping material, because E_C is independent of it, but not E_F (the higher the doping, the higher E_F). The question is now to see what happens when these two structures are put in contact. To do that it is important to consider three important characteristics: the first one is that E_F is constant through the junction, the second one is that the reference level E_0 cannot be a continuous function at the point; the last one is that the electron affinity of semiconductors is constant with the x -coordinate. The resulting energy band structure of a Metal-Semiconductor junction is shown in Figure 2.3. In the figure we can see a discontinuity between the energy states allowed to the electrons:

$$(2.1) \quad q\Phi_{MS} = q(\Phi_M - \chi)$$

and it depends on the metal and semiconductor materials chosen, and not on the doping. $q\Phi_i$, the other new magnitude showed in Figure 2.3, instead, depends on the doping. From the figure it is easy to deduce that it is equal to:

$$(2.2) \quad q\Phi_i = q(\Phi_M - \Phi_S) = q(\Phi_M - \chi) - |E_C - E_F|/n$$

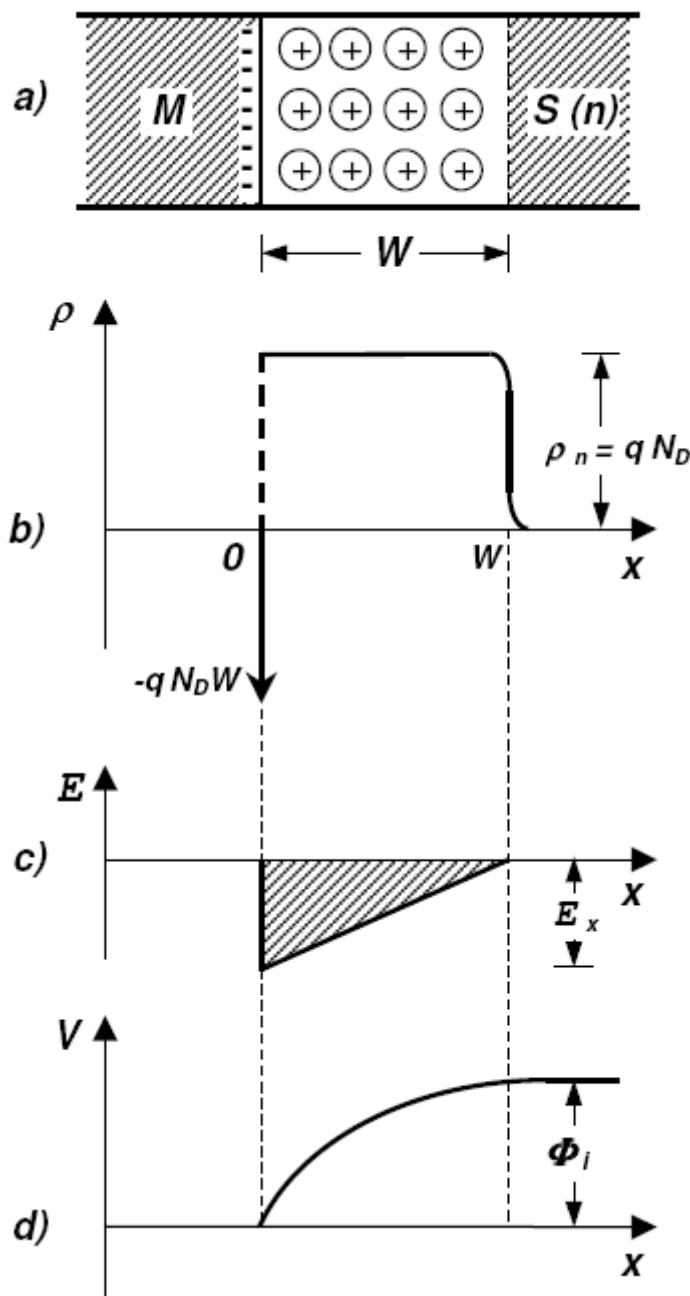


Figure 2.4: a) charge distribution in M-S junction; b) charges density distribution; c) electric field; d) electric potential.

and it is created by the electrons transit from the semiconductor to the metal. In particular, the electrons staying in the conduction band of the semiconductor, with energy higher than the free energy state of the metal, will fill that free energy level causing the bands flexion (and then the formation of $q\Phi_i$). Electrons pass from the semiconductor toward the metal because $\Phi_M > \Phi_S$, in other words, because the semiconductor electrons are more energetic than metal electrons. Due to the high density of electrons in the metal material, the negative charge arriving from the substrate is located in a layer of infinitesimal thickness, while in the semiconductor, for its lower electron density, the total charge occupies a much greater thickness (see Figure 2.4 a). In this case the charge is positive, and due to the

ionized donor atoms. The electrons transit finishes when the electric field E , generated for the two above mentioned space charge regions, compensates the electrons energy-difference of metal and semiconductor, that is, compensates the carriers flow.

Doing the approximation of total emptying, and uniform doping in the semiconductor, we can calculate the electric field E . In particular, we use the Poisson equation for the one-dimensional case:

$$(2.3) \quad \frac{dE}{dx} = \frac{\rho(x)}{\epsilon_s}$$

where ϵ_s is the dielectric constant ($\epsilon_0 \cdot \epsilon_t$) and $\rho(x)$ is the total charge density. From the Figure 2.4 b and the Poisson equation reported above, we easily obtain that:

$$(2.4) \quad E_x = -\frac{qN_D W}{\epsilon_s}$$

and rounding out the electric field, we calculate the potential difference Φ_i in the junction:

$$(2.5) \quad \phi_i = |E_x| \frac{W}{2} = \frac{qN_D W^2}{2\epsilon_s}$$

From this equation we can also calculate the thickness of the space charge region of the semiconductor as follows:

$$(2.6) \quad W = \sqrt{\frac{2\epsilon_s}{q} \frac{1}{N_D} \phi_i}$$

For calculating the total charge in the semiconductor we have to consider the junction area (A), so that we obtain:

$$(2.7) \quad Q_S = AqN_D W$$

and substituting equation (2.6) in (2.7), it results in:

$$(2.8) \quad Q_S = A\sqrt{2\epsilon_s q N_D \phi_i}$$

We have said the electrons pass from the semiconductor to the metal when the two solids are put in contact (forming diode schottky contact), but it is not always true. It depends on the values of Φ_M and Φ_S and on the doping of the semiconductor. We have considered the case of an n-doped substrate with $\Phi_M > \Phi_S$, and in this condition what we obtain is just a diode schottky contact but, under different conditions, it is also possible to obtain an

ohmic contact. In particular, there are two different ways to obtain it: taking an n-doped substrate with $\Phi_M < \Phi_S$ or using the tunnel effect. Firstly we will see what happens in the first case (figures 2.5 and 2.6). When the metal end semiconductor materials came in contact, being the metal electrons more energetic (by reason of $\Phi_M < \Phi_S$), they will pass toward the semiconductor, creating in it a negative charge layer, of infinitesimal thickness, located at the interface. To balance the negative charge area, a similar one, but of opposite sign, is established in the metal surface. In this case there is not the $q\Phi_{MS}$ barrier, as previously seen in the case of n-doped substrate with $\Phi_M > \Phi_S$, so that, applying an external positive voltage (that is, with the positive pole on the metal side), carriers will be free to move from a region to another.

Different is the situation for an ohmic contact realized using the tunnel effect (Figure 2.7). When a substrate is highly doped, the Fermi level goes closer to the E_C and the W thickness decreases. When it reaches a dozen of Angstroms, electrons start to pass through the barrier $q\Phi_{MS}$ without overcoming it, filling energy states of equal energy, available in the other side of the barrier: this is the so called Tunnel Effect.

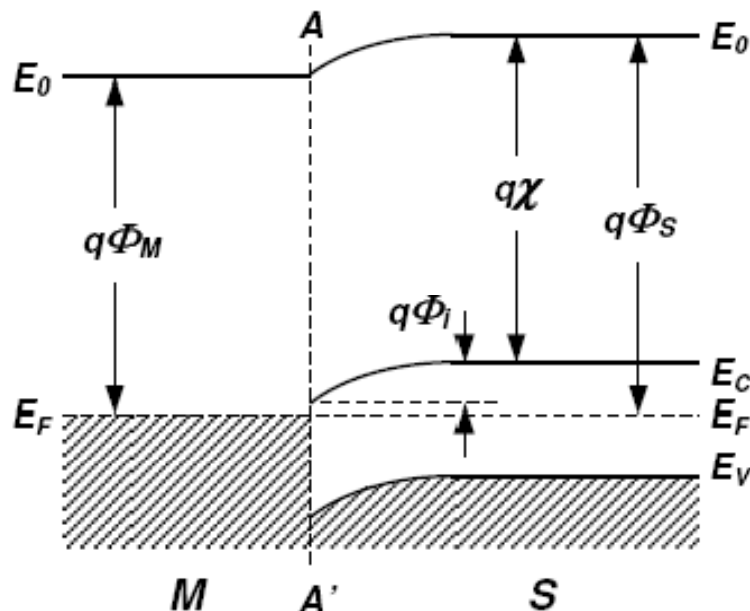


Figure 2.5: MS junction with $\Phi_M < \Phi_S$.

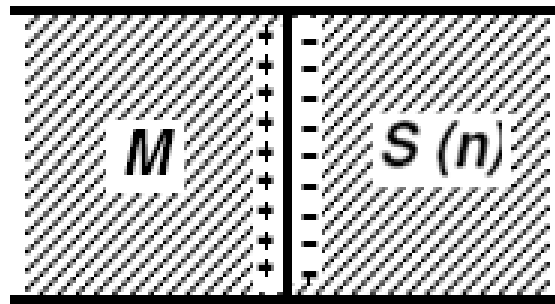


Figure 2.6: MS junction with n-doped semiconductor and $\Phi_M < \Phi_S$.

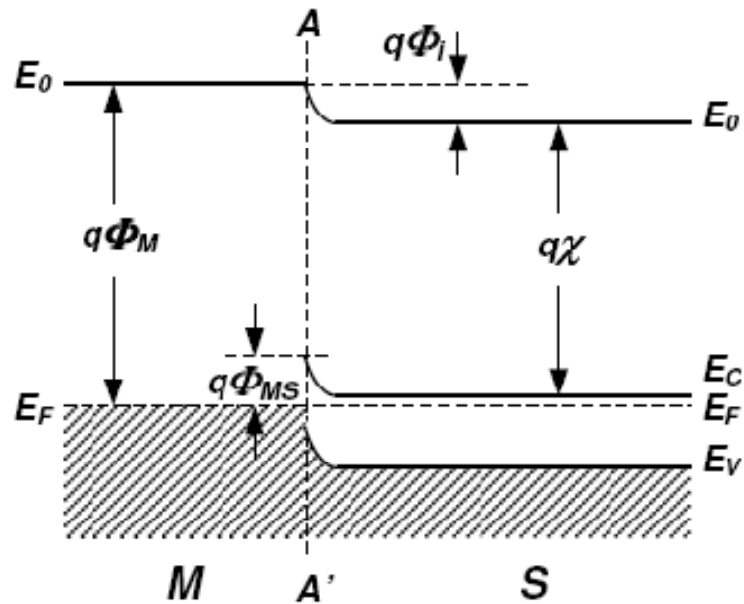


Figure 2.7: MS junction with high doped semiconductor.

For both cases of schottky contact and tunnel effect, it is easy to understand as, applying a positive external voltage, electrons will pass continuously toward the semiconductor because no barrier stop them (schottky contact) or because it is so thin to be easily crossed (tunnel effect): anyway, this is because the ohmic contact is established.

We have analyzed a Metal-Semiconductor Junction with n doped semiconductor. The question now is, what happens if we use a p-semiconductor: exactly the same. And what said above is valid also in this circumstance, with few obvious changes. In the case of n-doped material we said is necessary to have $\Phi_M > \Phi_S$ to establish a diode schottky contact. On the contrary, for a p-doped material, we need $\Phi_M < \Phi_S$ to establish it. This is because, with $\Phi_M < \Phi_S$, electrons pass from metal to semiconductor, filling the semiconductor hole at the interface, leaving negative charged ions. To compensate this negative charge in the semiconductor, a positive charge of infinitesimal thickness, is established in the metal. The theoretic development, with which we have obtained the formulas for n-doped semiconductors, is the same taking in consideration that the charge (in metal and in semiconductor) are now inverted. De facto, the only thing to change is N_D (donor atoms; positive charge from the n-doped semiconductor space charge region), with N_A (acceptor atoms; negative charge from the p-doped semiconductor space charge region).

Conversely, to obtain an ohmic contact with a metal and a p-semiconductor, it is necessary to have $\Phi_M > \Phi_S$. In other word, passing from n to p semiconductor, we have to change the condition on Φ_M and Φ_S , and the charge sign.

2.4 W depending on C

Applying an external inverse potential V to a Metal-Semiconductor junction, the total charge of the space charge region will be:

$$(2.9) \quad Q_S = A\sqrt{2\epsilon_s q N_D (\phi_i + V)}$$

hence, the differential barrier capacity results in:

$$(2.10) \quad C_{\Delta} = \frac{dQ_S}{dV} = A\sqrt{\frac{q\epsilon_s N_D}{2(\phi_i + V)}} = A\frac{\epsilon_s}{W}$$

having considered:

$$(2.11) \quad W = \sqrt{\frac{2\epsilon_s (\phi_i + V)}{q N_D}}$$

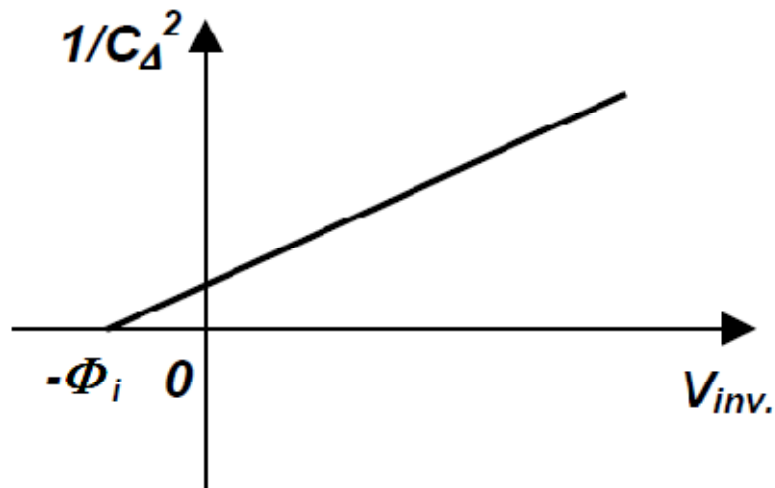


Figure 2.8: Reciprocal of the capacity squared as a function of the external potential applied (inverse voltage).

Equation (2.11) is the same of Equation (2.6) for an external potential applied. Rewriting Equation (2.10), and isolating $\phi_i + V$, we obtain:

$$(2.12) \quad \phi_i + V = A^2 \frac{q\epsilon_s N_D}{2C_\Delta^2}$$

If we subject a Metal-Semiconductor junction to different tension values, measuring the differential capacity in correspondence of each potential value applied, using the (2.11), we can obtain a graph such as the one shown in Figure 2.8 (V_{inv} stays for inverse voltage).

From the graph equation, setting $1/C_\Delta^2$ to zero, we obtain the value of the potential barrier at the junction. This value is important because gives us an idea about the maximum open circuit voltage (V_{OC}) achievable. In fact, as we will see in the next section, having a Metal p-semiconductor junction, and an increasing light hitting it, the higher the light, the higher the carriers generated, and then, the higher the photocurrent. The carriers flowing at the junction will partially fill the space charge region, making it thinner; therefore the barrier potential decreases and the external one increases: this is the normal working cycle of a solar cell. But when the load is high, tending to infinity, the carriers generated by light sources are all used to fill the space charge region (no charge is used to feed the photocurrent, equal to zero), so that it will be even thinner, and the external V_{OC}

higher. In Figure 2.9 are shown three different cases, considering the light arriving on the junction surface rising from A (case with no photon arriving) to C (case with a high photon intensity on the junction surface), and a load tending to infinity: increasing the photon intensity, the barrier potential decreases and V_{OC} increases. The maximum value for V_{OC} (achieved in Figure 2.9 C) is just the value of ϕ_i in the case A (without light). Certainly we cannot assess that ϕ_i is always equal to V_{OC} (because V_{OC} depends also on the light intensity) but, measuring the potential barrier, we can have an idea about the maximum open circuit voltage value achievable by a specific junction, in ideal conditions, and without voltage drop in the materials.

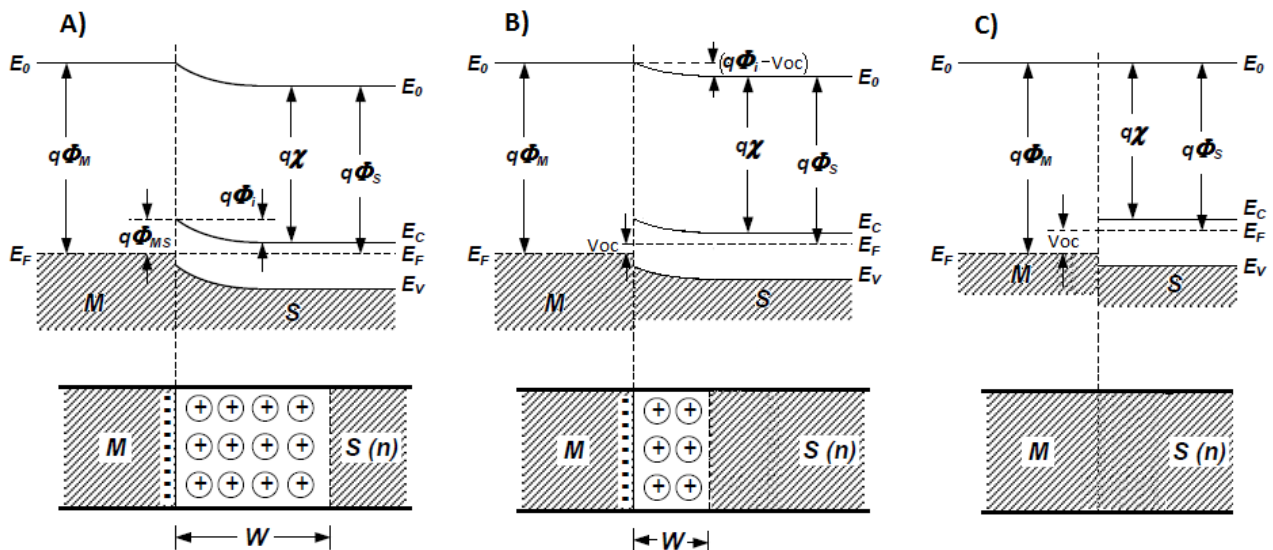


Figure 2.9: MS junction with increasing light intensity (from A to C) and infinity load.

2.5 From the MS junction to the MS solar cell

In section 2.3, we have seen the theoretic aspects concerning a MS junction, now we will see how it works in a solar cell to generate power. A solar cell is like a big diode (in our case MS diode), and then the V-I characteristic is the same of a normal diode (Figure 2.10).

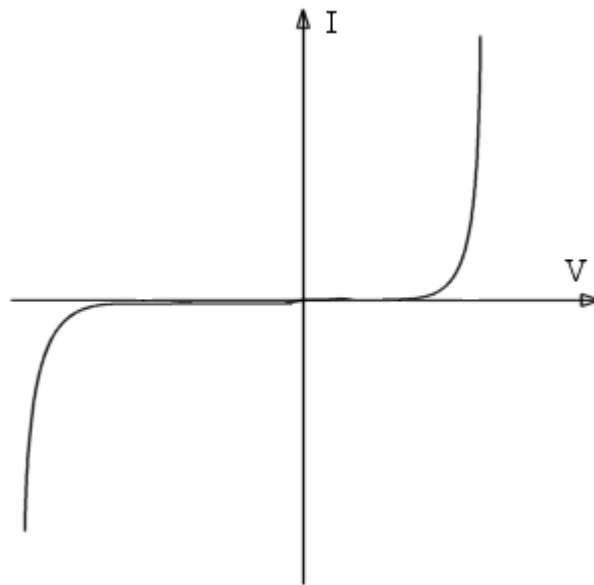


Figure 2.10: Diode and solar cell characteristic (without light).

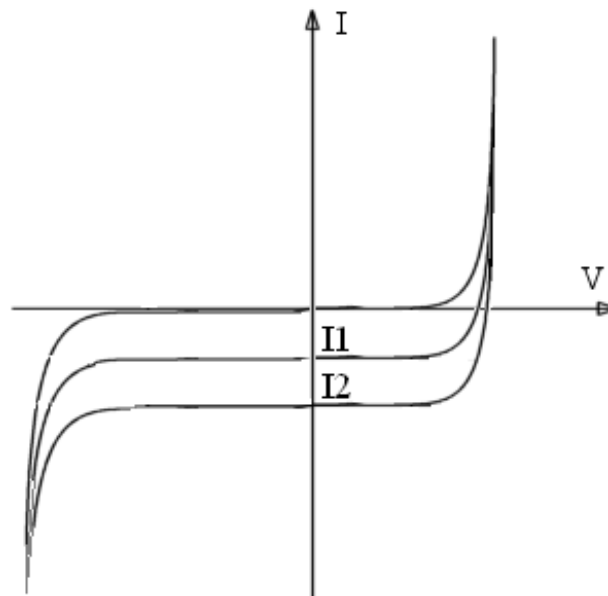


Figure 2.11: Solar cell characteristic with two light intensity
(intensity for $I_2 >$ intensity for I_1).

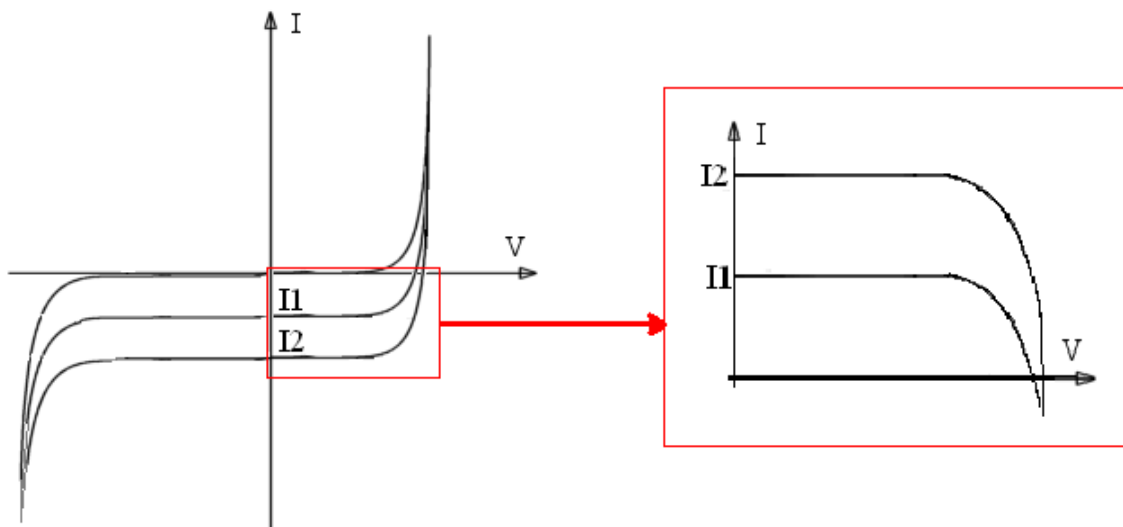


Figure 2.12: Solar cell characteristic usually shown (fourth quadrant inside the red box).

In the Figure 2.5 is shown the solar cell characteristic in presence of photon hitting it, and is easy to infer how the variation from the diode characteristic is in the current: the more the photon intensity, the more the current flowing through it (if photons have sufficient energy E_f to pump electrons toward the conduction band: $E_f > E_G$). Here is the point: unlike the diode one, in the solar cell characteristic there are points where the dissipated power is negative, namely, the power is generated. That happens in the fourth quadrant, where the current is negative and the voltage positive: this means that when the device works in that part of its characteristic, it generates power. That is why, when its characteristic is shown, it is common to draw only the fourth quadrant, that is the most interesting in the solar cell field (Figure 2.12).

The question now is about the possibility to have negative current and positive voltage in a solar cell. Thinking to the Metal-Semiconductor junction features, reported in the section 2.3, it is not hard to answer this question. As said, in a diode, the presence of two space charge regions of opposite sign (positive in n, negative in p) leads to the creation of an electric field, perpendicular to the junction plane, in such a direction to cross the charge flow due to the diffusion (taking place when metal and semiconductor came in contact). In equilibrium, at each point of the space charge region, the electric field effect exactly compensates the difference in concentration, therefore the total flow of mobile

charges is zero. However, in the space charge region can be formed electron-hole pairs by thermal agitation and, in this case, by reason of the electric field E , electrons are swept toward the metal region and hole toward the p-semiconductor region. This flow of charges leads to a small reverse current, but if photoelectric effect is added to the thermal one, electron-hole pairs gradually increase and, with them, the reverse current (Figure 2.13). Raising the number of electrons passing toward metal and the number of holes passing toward the p-semiconductor, as well as the current increases, the potential barrier decreases (for the reasons explained in section 2.4) and then, ultimately, there is a positive voltage across the cell, with the positive pole on the metal and, the negative one on the p-semiconductor. Eventually, what we have is a device with a voltage across it, with a current entering from the positive pole: that is a power generator.

For completeness we say it is not true that electron-hole pairs have to appear in the space charge region to be useful to fell the photocurrent. In fact they can appear wherever in the semiconductor, granting that theirs diffusion length is long enough to reach the area where the electric field is present.

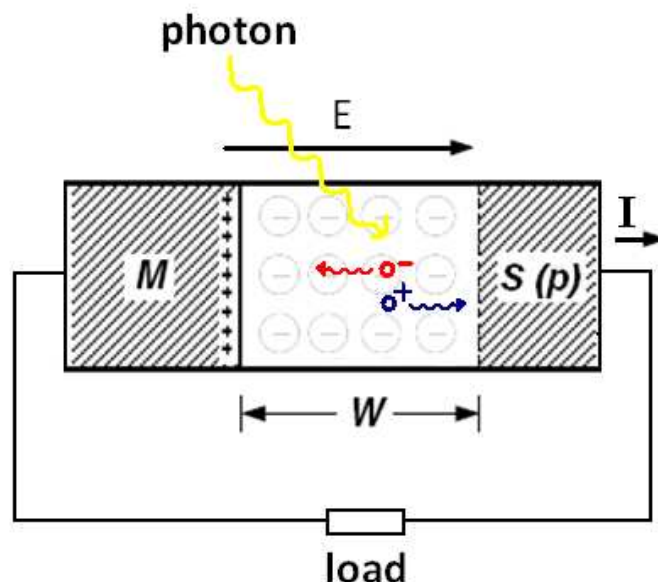


Figure 2.13: Photocurrent generation in solar cells.

2.6 Main parameters of a solar cell

2.6.1 Basic concepts and definitions

In this section we introduce some basic concepts concerning solar cells field, useful to be familiar with the matter treated in this work.

The power $P(t)$ is expressed in Watt (W), and its time-integral gives the Energy value (E), usually expressed in Joules:

$$(2.13) \quad E = \int_{t_1}^{t_2} P(t) dt$$

There are also other units of measurement used for E, in particular, the most commonly used in energies business is the KWh:

$$(2.14) \quad E = \int_{t_1}^{t_2} P(t) dt = \int_{hour} P(t) dt = [kWh_hour]$$

And its relation with J unit is:

$$1KWh = 10^3 W \cdot 3600s = 3.6 \cdot 10^6 J$$

Photovoltaic modules efficiency, sometime is expressed in terms of KWh produced per square meter. But is not always clear the reference used to express it, because is known that the produced energy is related to the energy arriving on the panel surface, in other word, it is related to the effective sun spectrum considered.

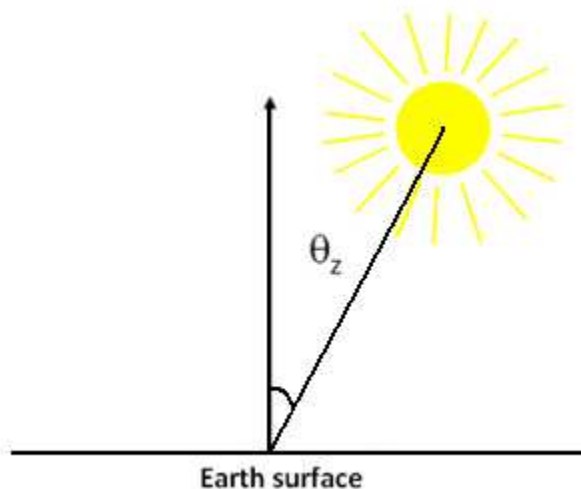


Figure 2.14: ϑ_z representation.

Defining θ_z as the angle between the perpendicular to the earth surface and the sun direction from the same earth point (Figure 2.14), we can define the AIR MASS x (AM x) unit:

$$(2.15) \quad x = \frac{1}{\cos \theta_z}$$

For example the sun spectrum AR0 is that one outside the atmosphere: it is used for space applications. For earth's applications is generally considered the spectrum AM1.5 shown in Figure 2.15 (obtained with $\theta_z=48.19^\circ$).

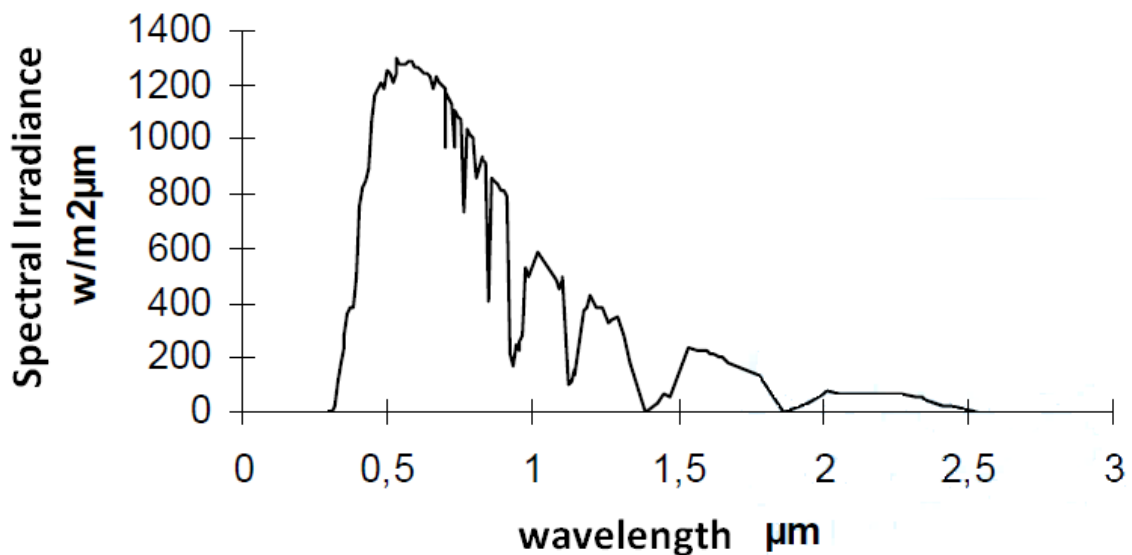


Figure 2.15: Spectral irradiance AM1.5.

The sun spectrum is the value of the spectral irradiance as a function of wavelength. Spectral Irradiance (I_λ) is defined as the power density per unit area and unit wavelength, received on a surface (unit of measurement: $W/m^2\mu m$). Irradiance I , is given by the integral of the irradiance extended to all the wavelength range of interest (unit of measurement: W/m^2 , that is, power density). Finally, Radiation (H) is given by the time integration of the irradiance (unit of measurement: J/m^2_day or kWh/m^2_day).

The I_λ measured values, are usually normalized so that $I=1000W/m^2$ (AM 1.5).

2.6.2 Dark current and photocurrent

To calculate the current flowing through a solar cell, we have to start speaking about the free charge concentration in a solid. We have said a solid has some energy states, so that the electrons concentration is given by the probability to find both an electron and an energy state in the solid. Considering all the energy states of interest we can write:

$$(2.16) \quad n = \int D(E) f(E) dE$$

Where $D(E)$ is the density of states and $f(E)$ is the probability to find an electron. $F(E)$ is called Fermi Function and its expression is:

$$(2.15) \quad F(E) = \frac{1}{1 + e^{\frac{(E-E_F)}{kT}}}$$

Where E is the generic energy level, E_F the Fermi level, K the Boltzmann constant and T the absolute temperature. In Figure 2.16 is shown the variation of $f(E)$ with T .

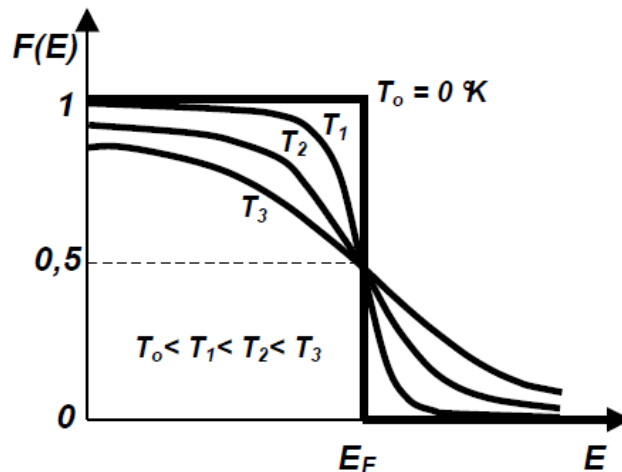


Figure 2.16: variation of the Fermi Function with T .

Taking into consideration the case of an energy level sufficiently higher than E_F (for example considering an energy state in the conduction band E_c) it is possible to introduce the following approximation:

$$(2.16) \quad e^{\frac{E-E_F}{kT}} \gg 1$$

$$(2.17) \quad f(E) \approx e^{-\frac{(E-E_F)}{kT}}$$

Considering another time the case of the conduction band, $D(E)$ is given by

$$(2.18) \quad D(E) = A_C (E - E_C)^{\frac{1}{2}}$$

$$(2.19) \quad A_C = 4\pi(2m_c)^{3/2} / h^3$$

Where m_c is the electron mass and h is the constant of Plank. Substituting (2.17) and (2.18) in (2.16) we obtain:

$$(2.20) \quad n = A_C \int_{E_C}^{E_{Top}} (E - E_C)^{\frac{1}{2}} e^{-\frac{(E-E_F)}{kT}} dE$$

Calculating the integral also for the holes in valence band (having a similar integral to calculate) the concentrations result in:

$$(2.21) \quad n = N_C e^{-\frac{(E_C-E_F)}{kT}}$$

$$(2.22) \quad p = N_V e^{-\frac{(E_V-E_F)}{kT}}$$

$$(2.23) \quad N_C = A_C (kT)^{\frac{3}{2}} \sqrt{\frac{\pi}{2}}$$

$$(2.24) \quad N_V = A_V (kT)^{\frac{3}{2}} \sqrt{\frac{\pi}{2}}$$

Where E_C is the lowest energy level of the CB, and E_V is the highest energy level of VB.

Multiplying n and p come out the following equation ($np=n_i^2$ is called mass equation and it is valid for both intrinsic and extrinsic semiconductor because it does not depend on the doping concentration):

$$(2.25) \quad n \cdot p = n_i^2 = N_C N_V e^{-\frac{E_G}{kT}}$$

Where n_i^2 (that is an important factor for the solar cells performances) is the intrinsic concentration. In particular, a semiconductor is called intrinsic if the number of electrons in the CB is the same of the holes number in the VB. In an intrinsic material E_F stays in the center of the band gap and, in this particular case, it is indicated with E_{Fi} . Hence, considering an intrinsic material, we have:

$$(2.26) \quad n = N_C e^{-\frac{E_C-E_{Fi}}{kT}} = p = N_V e^{-\frac{E_V-E_{Fi}}{kT}}$$

$$(2.27) \quad E_{F_i} = \frac{E_C + E_V}{2} + \frac{kT}{2} \ln \frac{N_V}{N_C}$$

We have calculated the electron concentration in the CB and the hole concentration in the VB, but we want to obtain the solar cell current, so we have to consider the movement of these charges subjected to the electric field present in a p-n or Metal-Semiconductor junction (forming a schottky diode junction). Holes move in the Electric Field (E) direction, despite electrons in the opposite one, so we can write:

$$(2.28) \quad \vec{J}_n = qn\mu_n \vec{E}$$

$$(2.29) \quad \vec{J}_p = qp\mu_p \vec{E}$$

Where J_n and J_p are the current densities of electrons and holes, q is the electron charge and, μ_n and μ_p , the mobility of electrons and holes respectively. Summing the two precedent equations we obtain the total current density:

$$(2.30) \quad \vec{J}_{tot} = \vec{J}_n + \vec{J}_p = q\vec{E}(n\mu_n + p\mu_p) = \sigma \vec{E}$$

$$(2.31) \quad \sigma = q(n\mu_n + p\mu_p)$$

σ is the conductivity, and its reciprocal is the resistivity.

Beyond the above calculated current (drift current), there is another component to sum: the diffusion current. It is due to the different charge concentration in the semiconductor. In an n-doped semiconductor the electron flux (considering only the x coordinate), will be:

$$(2.32) \quad F_n = -D_n \frac{dn}{dx}$$

where D_n is the diffusion constant and dn/dx is the concentration gradient. The minus sign means that the flux is proportional, but in the opposite direction, to the current concentration gradient. D_p is linked to the mobility by the Einstein relations (k is the Boltzmann constant and T the absolute temperature):

$$(2.33) \quad D_n = \frac{\mu_n kT}{q}$$

From the flux is easy to obtain the current density, just multiplying for the electron charge q :

$$(2.34) \quad J_n = qD_n \frac{dn}{dx}$$

Equivalently for a p-doped semiconductor:

$$(2.35) \quad J_p = -qD_p \frac{dp}{dx}$$

Equation (2.34) has a positive sign because the negative flux is multiplied for a negative charge (electron charge); equation (2.35) is negative by reason of the positive sign of the holes charge, remaining negative the flux.

The total density currents (for electrons and for holes) are then:

$$(2.36) \quad J_p = q(\mu_p pE - D_p \frac{dp}{dx})$$

$$(2.37) \quad J_n = q(\mu_n nE + D_n \frac{dn}{dx})$$

When a light beam hits a semiconductor surface, it causes a charge generation. Therefore there is a charges generation dues to the light (G), added to the one dues to thermal effects (G_{th}). This generation phenomena are compensated by the recombination (R). The net charge resulting is the charge time-variation:

$$(2.38) \quad \frac{dp}{dt} = G + G_{th} - R = G_L - U$$

Referring with U ($R-G_{th}$) to the effective recombination velocity. The bigger the excess charge, the bigger U, so we can write:

$$(2.39) \quad \frac{dp}{dt} = G - \frac{p - p_0}{\tau_p}$$

Where τ_p is the charge lifetime of holes, and τ_n is the time charge lifetime of electrons.

But, for the continuity law, the time-variation of the charge is proportional also to the density current variation; Then, doing the same reasoning for holes, we obtain:

$$(2.40) \quad -\frac{\partial p}{\partial t} = \frac{1}{q} \frac{\partial J_p}{\partial x} + \frac{p - p_0}{\tau_p} - G(x)$$

$$(2.41) \quad -\frac{\partial n}{\partial t} = \frac{1}{q} \frac{\partial J_n}{\partial x} + \frac{n - n_0}{\tau_n} - G(x)$$

Now we have to seek the $G(x)$ equation. A photon beam hitting a solid surface is absorbed exponentially inside it, than the photon flux decays with the same law. Calling $\phi(x)$ the photon flux with the x coordinate, and α the absorption coefficient, said law results in:

$$(2.42) \quad \phi(x) = \phi(0)e^{-\alpha x}$$

Also known as Lambert's law.

Considering that each photon differential $d\phi$ absorbed in a dx is converted in an electron-hole pair, we can write:

$$(2.43) \quad G(x, y) = -\frac{d\phi(x, y)}{dx} = \alpha(\lambda)\phi_0(\lambda)e^{-\alpha(\lambda)x}$$

From the continuity equation of electrons, considering: $E=0$ (because of the constant doping and because we consider the condition without external potential applied), and

then, from (2.37) $\frac{\partial J_n}{\partial t} \frac{1}{q} = D_n \frac{dn^2}{dx^2}$; steady state, namely, $\frac{\partial n}{\partial t} = 0$; for G the equation (2.34);

$n-n_0=n'$; low injection condition (minority charges injected are lower than the majority charge concentration, than the charges variation is relevant also for minorities), we obtain:

$$(2.44) \quad D_n \frac{d^2 n'}{dx^2} - \frac{n'}{\tau_n} = -\alpha\phi_0 e^{-\alpha x}$$

We can now consider also one contribution to the diffusion current (the only component, having set to zero the electric field E , and then the shift current). This is because, it can be shown that the inverse current (that is the one of interest in a solar cell, than, the one we want to calculate) in a diode junction, is almost completely given by the carriers of the less doped area. Therefore, in a p-n junction with n-doping concentration higher than p doping concentration, or in a metal p-semiconductor junction, the inverse current is given by the electros of the p side.

What we have to do at this point is to consider the case of a junction (and not of an isolated material) and to calculate the n-doping concentration from (2.44), to put it in the equation of the diffusion current for n-carriers.

Fist, we calculate the root of the homogeneous equation:

$$(2.45) \quad D_n r^2 - \frac{1}{\tau_n} = 0$$

$$(2.46) \quad r = \pm \sqrt{\frac{1}{D_n \tau_n}} = \pm \frac{1}{L_n}$$

$$(2.47) \quad L_n = \sqrt{D_n \tau_n}$$

Where L_n is called diffusion length. The solution of the homogeneous equation is then:

$$(2.48) \quad n'_p = Ae^{-\frac{x}{L_n}} + Be^{\frac{x}{L_n}}$$

The boundary conditions are:

- $(n_p - n_{p0})_0 = n_{p0} \left(e^{\frac{V}{V_T}} - 1 \right)$ (schottky injection)
- $\lim_{x \rightarrow \infty} n'_p(x) = 0$

Where V is the polarization and $V_T = KT/q$. From the second boundary condition we obtain that $B=0$, so that:

$$(2.49) \quad n'_p = Ae^{-\frac{x}{L_n}}$$

Considering now the first boundary condition, and then, the particular solution, the final equation results in:

$$(2.50) \quad n'_p = n_{p0} (e^{V/V_T} - 1) e^{-x/L_n} + \frac{\alpha \tau_n \phi_0}{L_n^2 \alpha^2 - 1} (e^{-x/L_n} - e^{-\alpha x})$$

and finally, applying the equation of the diffusion current for electrons we obtain:

$$(2.51) \quad J_n = qD_n \left. \frac{dn'_p}{dx} \right|_{x=0} = -q \frac{D_n}{L_n} n_{p0} (e^{V/V_T} - 1) + \frac{q\alpha L_n \phi_0}{L_n \alpha + 1}$$

So we have two components contributing to the total current. The first one, negative, is the dark current (proportional to the polarization and independent of the photon flux), the other one, positive, is the photocurrent (proportional to the photon flux and independent of the polarization).

Redefining the dark current, and the photocurrent we have:

$$(2.52) \quad J = -J_0 (e^{V/V_T} - 1) + J_L$$

$$(2.53) \quad J_0 = q \frac{D_n}{L_n} n_{p0}$$

$$(2.54) \quad J_L = \frac{q\alpha L_n \phi_0}{L_n \alpha + 1}$$

As we can see from the equation (2.54) the main effects on the photocurrent are:

- Absorption: the absorption coefficient α depend on the semiconductor nature (direct or indirect), and on its bandgap value;
- Reflectance: modifies ϕ_0 , and depends on the surface shape and coating (antireflection coating);
- Drift-diffusion parameters: carrier lifetime (L_n and L_p) and mobility (μ_n and μ_p);
- Surface recombination.

It can be shown that the recombination coefficient is equal to:

$$(2.55) \quad R = \frac{r_0^2 + r_{sc}^2 + 2r_0 r_{sc} \cos 2\beta}{1 + r_0^2 r_{sc}^2 + 2r_0 r_{sc} \cos 2\beta}$$

$$(2.56) \quad r_0 = \frac{n_{ar} - n_0}{n_{ar} + n_0}$$

$$(2.57) \quad r_{sc} = \frac{n_{sc} - n_{ar}}{n_{sc} + n_{ar}}$$

$$(2.58) \quad \beta = \frac{2\pi}{\lambda} n_{ar} d$$

Where n_0 is the refraction coefficient of the air, n_{sc} is the refraction coefficient of the coated material, n_{ar} is the refraction coefficient of the coating material, λ is the wavelength of the photon to be absorbed, and d is the thickness of the antireflection coating (Figure 2.17). The R equation is equal to zero (the ideal condition) when:

$$(2.59) \quad d = \frac{\lambda}{4n_{ar}}; \frac{3\lambda}{4n_{ar}}; \frac{5\lambda}{4n_{ar}}; \dots$$

$$(2.60) \quad n_{ar} = \sqrt{n_0 n_{sc}}$$

Afterwards, considering the first equation for d , the conditions to set R to zero are:

- Refraction coefficient of the antireflection coating equal to the geometric average of the refraction coefficient of the two adjacent materials;

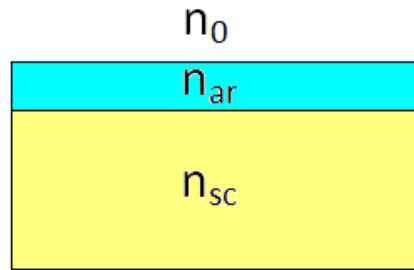


Figure 2.17: Antireflection coating.

- Thickness of the coating approximately the same as a quarter wavelength.
- These elements are considered to make antireflection coating.

2.6.3 Quantum efficiency and spectral response

Other two important parameters in the solar cell field are the quantum efficiency (QE) and the spectral response (SR), both generally given as a function of λ . QE is defined as the ratio of the generated photocurrent density to the photon spectral density multiplied for the electron charge q :

$$(2.61) \quad QE(\lambda) = \frac{J_{sc}(\lambda)}{q\phi_0(\lambda)}$$

SR is instead defined as the ratio of the generated photocurrent density, multiplied for the electron charge q , to the incident power (spectral irradiance):

$$(2.62) \quad SR = q \frac{J_{sc}(\lambda)}{I(\lambda)}$$

It can be shown that they are related by the following equation:

$$(2.63) \quad SR = 0.808 \cdot \lambda \cdot QE$$

With $SR=[A/W]$ and $\lambda=[\mu m]$.

2.6.4 Solar cell efficiency

We have yet spoken about the factors affecting the photocurrent, but now, in this section, we want to focus the attention on losses factors affecting both photocurrent and other

efficiency parameters, like the open circuit voltage V_{OC} . More generally speaking, we will analyze the solar cell efficiency (η) equation. It is given by the ratio of the generated power, to the entering power:

$$(2.64) \quad \eta = \frac{P_{\max}}{P_{in}}$$

The maximum power generated is equal to the multiplication of the maximum current (I_m) and the maximum voltage generated (V_m). Considering: A the total solar cell area, A_c the part of it that is covered (for example because of the fingers); $I_m V_m = I_{sc} V_{OC} FF$ and $I_{sc} = (A - A_c) J_{SC}$, P_{\max} results in:

$$(2.65) \quad P_{\max} = (A - A_c) J_{sc} V_{oc} FF$$

P_{in} , instead, is equal to the irradiance, multiplied for the total area:

$$(2.66) \quad P_{in} = A \int I(\lambda) d\lambda = A \cdot G$$

Substituting (2.65) and (2.66) in (2.64), we obtain:

$$(2.67) \quad \eta = \frac{A - A_c}{A} \frac{J_{sc} V_{oc} FF}{\int_0^{\infty} I(\lambda) d\lambda} = \left(1 - \frac{A_c}{A}\right) \frac{J_{sc} V_{oc} FF}{\int_0^{\infty} I(\lambda) d\lambda}$$

where J_{SC} is given by:

$$(2.68) \quad J_{sc} = J_{sc \max} (1 - R^*) \eta_{col} \eta_d$$

R^* is the average reflection coefficient (average of all the reflection coefficients for each wavelength); η_{col} is the collection efficiency (not all the carrier generated are actually collected to feed the photocurrent); η_d is the absorption efficiency, it considers that not all the photons can be absorbed by reason of the solar cell finite dimension; $J_{SC \max}$ is the maximum short circuit current, considering the case in which all the generated carriers are usefully used to feed the photocurrent. It takes into consideration only the absorbed photons (wavelengths of interest) and not all the spectrum:

$$(2.69) \quad J_{sc \max} = q \int_0^{\lambda_g} \phi_0(\lambda) d\lambda$$

Substituting (2.68) in (2.67) and multiplying and dividing for E_G and for $\int_0^{\lambda_g} I(\lambda) d\lambda$, it comes out the following equation for the total efficiency:

$$(2.70) \quad \eta = \frac{\int_0^{\lambda_g} I(\lambda) d\lambda}{\int_0^{\infty} I(\lambda) d\lambda} \frac{E_g \int_0^{\lambda_g} \phi_0(\lambda) d\lambda}{\int_0^{\lambda_g} I(\lambda) d\lambda} \left(1 - \frac{A_c}{A}\right) (1 - R^*) \eta_{col} \eta_d FF \frac{qV_{oc}}{E_g}$$

In (2.70) we observe eight “efficiency factor”:

- Partial absorption of the sun’s spectrum: $\frac{\int_0^{\lambda_g} I(\lambda) d\lambda}{\int_0^{\infty} I(\lambda) d\lambda}$;

- Partial conversion of the photon energy: $\frac{E_g \int_0^{\lambda_g} \phi_0(\lambda) d\lambda}{\int_0^{\lambda_g} I(\lambda) d\lambda}$;

- Surface coverage: $\left(1 - \frac{A_c}{A}\right)$;

- average reflection: $(1 - R^*)$;

- η_{col} ;

- η_d ;

- FF ;

- Voltage factor: $\frac{qV_{oc}}{E_g}$.

2.7 PSpice simulation

Before to show and analyze the experimental results, it is probably better to get a more theoretical approach, to give a broad idea about typical values of solar cell parameters (the values we reasonably expect to obtain), to finally compare expected and experimental results. Clearly we cannot care about all the aspects concerning solar cell simulation with PSpice; for a deepening about the matter, we relates to [3]. PSpice models reported in this section are from the same paper.

Before arriving to the final electric circuit to simulate, we have to introduce equations and definitions useful to draw, or simply better understand, the equivalent circuit. We will start from the ideal cell equivalent circuit, adding element of non-ideality, finally arriving to the most complete circuit to simulate (at least for our scope). As seen, The most general equation describing a solar cell behavior is the following (considering current density):

$$(2.71) \quad J = -J_0(e^{V/V_T} - 1) + J_L$$

Considering a solar cell of area A, multiplying said area for the above equation, we obtain the same one with currents instead of current densities:

$$(2.72) \quad I = -I_0(e^{V/V_T} - 1) + I_L$$

What we want from PSpice simulation is the I-V characteristic but, beyond the above reported equation, there are important parameters we should take into consideration related to it. The Figure 2.18 reports the I-V characteristic and the above mentioned parameters: I_{SC} , I_m , V_{SC} , V_m , P_m , FF.

I_{OC} is the current flowing through the solar cell when the voltage across it is zero:

$$(2.73) \quad I_{SC} = -I_0(e^{0/V_T} - 1) + I_L = I_L$$

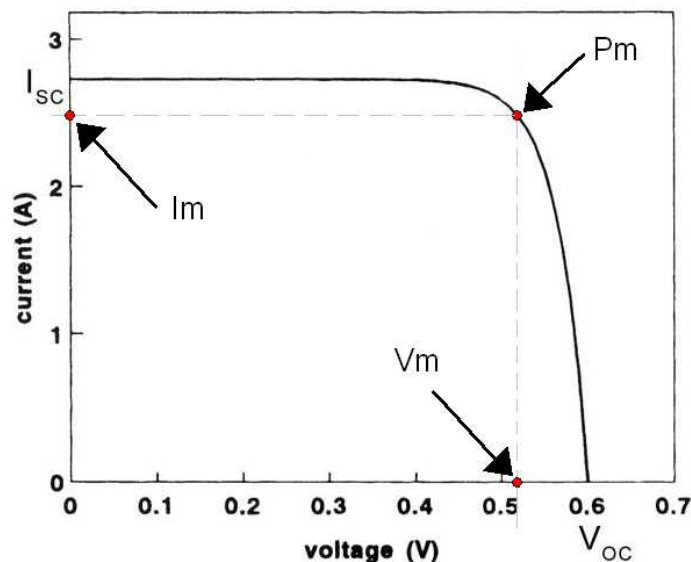


Figure 2.18: I-V characteristic of a solar cell and its most important parameters.

The open circuit voltage V_{OC} , is that voltage obtained when the external load to which the cell is connected, tends to infinity, namely, the current is zero:

$$(2.74) \quad 0 = -I_0(e^{V_{OC}/V_T} - 1) + I_L$$

And isolating V_{OC} from the last equation it becomes:

$$(2.75) \quad V_{OC} = V_T \ln\left(1 + \frac{I_L}{I_0}\right)$$

If we want to calculate the maximum power (P_m), we have to derivate the power (VI) and set it to zero.

$$(2.76) \quad \frac{dVI}{dV} = \frac{d}{dV} \left\{ -VI_0(e^{V_{OC}/V_T} - 1) + VI_L \right\} = 0$$

$$(2.77) \quad I_L + I_0 - I_0 e^{V_m/V_T} \left(1 + \frac{V_m}{V_T}\right) = 0$$

Where V_m is the voltage in correspondance of P_m . The above obtained is a transcendental equation, so we can calculate it with a numerical methods. From the above equation we can obtain the coming after, useful to calculate V_m ;

$$(2.78) \quad V_{OC} = V_m + V_T \ln\left(1 + \frac{V_m}{V_T}\right)$$

That is obviously another time a transcendental equation. Obtained V_m , we should calculate I_m (current in correspondance of P_m) from the following equation:

$$(2.79) \quad I_m = -I_0(e^{V_m/V_T} - 1) + I_L$$

There are also other simpler models to calculate I_m and V_m . We propose two of them. The first one is the following:

$$(2.80) \quad V_m = V_{OC} - 3V_T; \quad I_m = -I_0(e^{V_m/V_T} - 1) + I_L$$

and the other one is the succeeding:

$$(2.81) \quad \frac{V_m}{V_{OC}} = 1 - \frac{1 + \beta}{2 + \beta} \frac{\ln(1 + \beta)}{\beta}; \quad \frac{I_m}{I_{SC}} = 1 - \frac{1 - (1/\beta)}{\beta}; \quad \beta = \ln\left(\frac{I_{SC}}{I_0}\right)$$

Another important parameter is the Fill Factor (FF), defined as the coefficient between the maximum rectangles, inscribed and circumscribed of the I-V curve (Figure 2.19):

$$(2.82) \quad FF = \frac{V_m I_m}{V_{OC} I_{SC}}$$

Substituting the function of V_m/V_{OC} and I_m/I_{SC} reported before, FF results in:

$$(2.83) \quad FF = \left(1 - \frac{1 - \beta}{\beta}\right) \left(1 - \frac{1 - \beta}{2 + \beta} \frac{\ln(1 + \beta)}{\beta}\right); \quad \beta = \ln\left(\frac{I_{SC}}{I_0}\right)$$

And with some approximations, we obtain:

$$(2.84) \quad FF_0 = \frac{v_{oc} - \ln(v_{oc} + 0.72)}{1 + v_{oc}}; \quad v_{oc} = \frac{V_{OC}}{V_T}$$

Where sub-index “0” indicates that it is the FF value for an ideal solar cell, without taking into consideration the resistances effects we will introduce later.

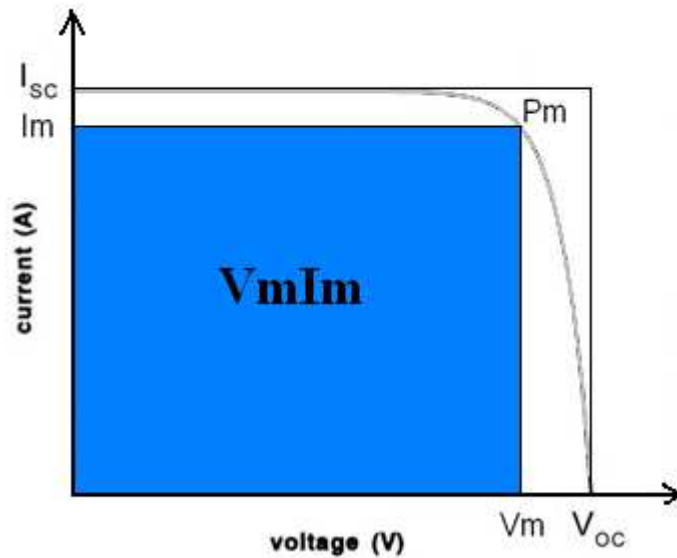


Figure 2.19: Fill Factor representation.

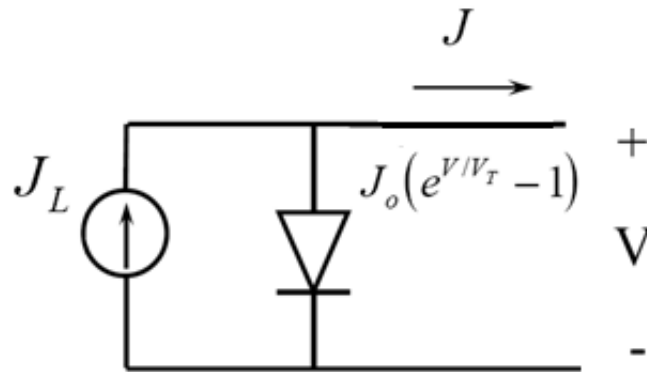


Figure 2.20: Equivalent circuit for an ideal solar cell.

The circuit representing the functioning of an ideal solar cell is the one shown in Figure 2.20. It considers the simplest equation $I=f(v)$, that is:

$$(2.85) \quad I = -I_0(e^{v/V_T} - 1) + I_L$$

But solar cells are not ideal, so we need to add some elements to this first simple circuit model, to represent as more faithfully as possible their functioning. In particular, we have to take into consideration three non-ideality phenomena:

- series resistance;
- shunt resistance;
- recombination in the space charge region.

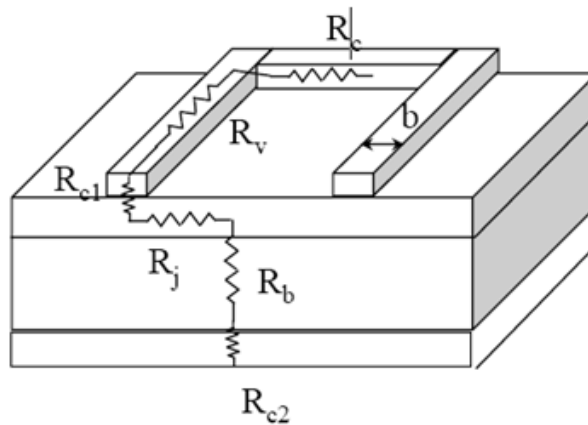


Figure 2.21: Series resistance components.

The components of the series resistance are represented in Figure 2.21: R_b is the resistance due to the substrate; R_c represents the bus collector resistance, that is the resistance of the central finger; R_v is the resistance of the thinner fingers, branching out from the central one; R_j is the square resistance of the emitter (terminal coating the substrate); R_{c1} and R_{c2} are the front contact and back contact resistances respectively.

The $I=f(V)$ equation resulting taking into consideration the series resistance (R_S) effects is as follows:

$$(2.86) \quad I = -I_0(e^{\frac{V+IR_S}{V_T}} - 1) + I_L$$

and the related equivalent circuit is shown in Figure 2.22.

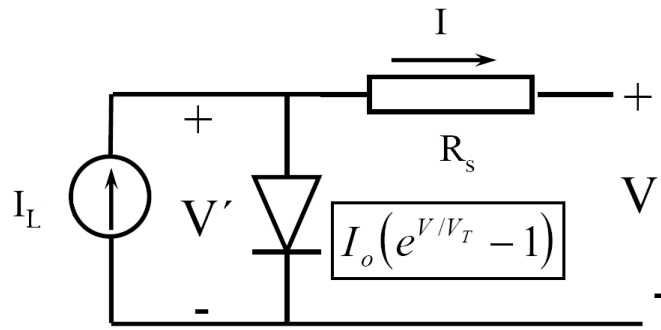


Figure 2.22: Equivalent circuit for a solar cell considering series resistance effects.

An important deduction we can do from the above reported equation is that V_{OC} is independent of series resistance.

Is interesting to see how series resistance affects to the P_m and to the FF. To do that we define P_m the maximum power with $R_s=0$, and P'_m the maximum power with $R_s>0$. Therefore:

$$(2.87) \quad P'_m = P_m - I_m R_s = V_m I_m - I_m^2 R_s$$

$$(2.88) \quad P'_m = P_m \left(1 - \frac{I_m}{V_m} R_s\right)$$

With the hypothesis $V_m/I_m = V_{OC}/I_{SC}$ we can write:

$$(2.89) \quad \frac{I_m}{V_m} R_s = \frac{R_s}{V_m / I_m} \approx \frac{R_s}{V_{OC} / I_{SC}} = r_s \frac{I_m}{V_m} R_s = \frac{R_s}{V_m / I_m} \approx \frac{R_s}{V_{OC} / I_{SC}}$$

and then:

$$(2.90) \quad P'_m = P_m (1 - r_s)$$

As we can see, the power losses are approximately linear with R_s .

The FF equation changes are immediate:

$$(2.91) \quad FF = \frac{P'_m}{V_{OC} I_{SC}} = \frac{P_m}{V_{OC} I_{SC}} (1 - r_s)$$

$$(2.92) \quad FF = FF_0 (1 - r_s)$$

In Figure 2.23 is shown the I-V characteristic of a solar cell with the change of R_s : rising R_s , V_{OC} , I_{SC} , I_m practically do not change; what changes is V_m , and then, P_m (dropping).

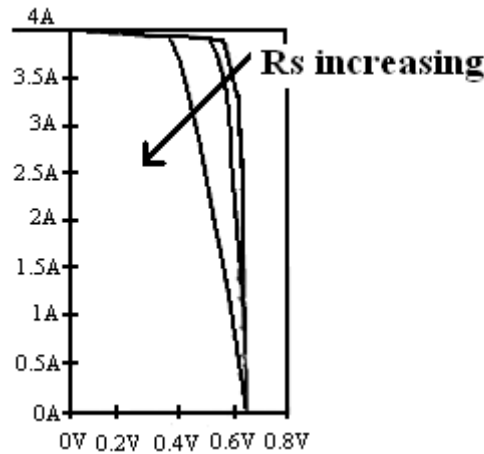


Figure 2.23: I-V characteristic of a solar cell with the change of R_s .

Another phenomenon affecting the solar cell performance, as said, is the shunt resistance (R_{sh}). It is due mainly to junction defects and border effects that cause current recombination, namely, losses. Considering also this losses effect, the $I=f(V)$ equation becomes:

$$(2.93) \quad I = -I_0 \left(e^{\frac{V+IR_s}{V_T}} - 1 \right) + I_L - \frac{IR_s + V}{R_{sh}}$$

The resulting equivalent circuit is shown in Figure 2.24, while in Figure 2.25 is shown the I-V characteristic of a solar cell with the change of R_{sh} : rising R_{sh} , the slopes of the curve changes (before and after P_m), V_{OC} , V_m and I_m rise and then, rises P_m .

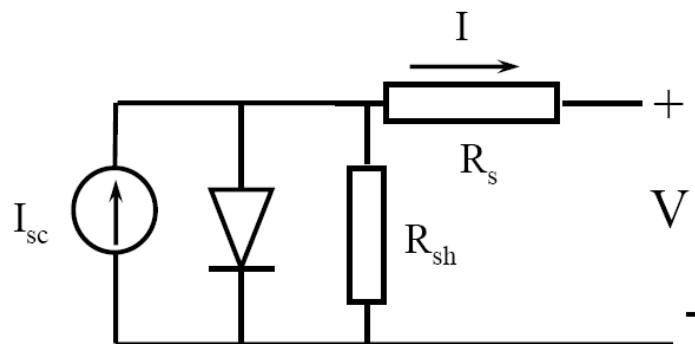


Figure 2.24: Equivalent circuit for a solar cell considering series and shunt resistance effects.

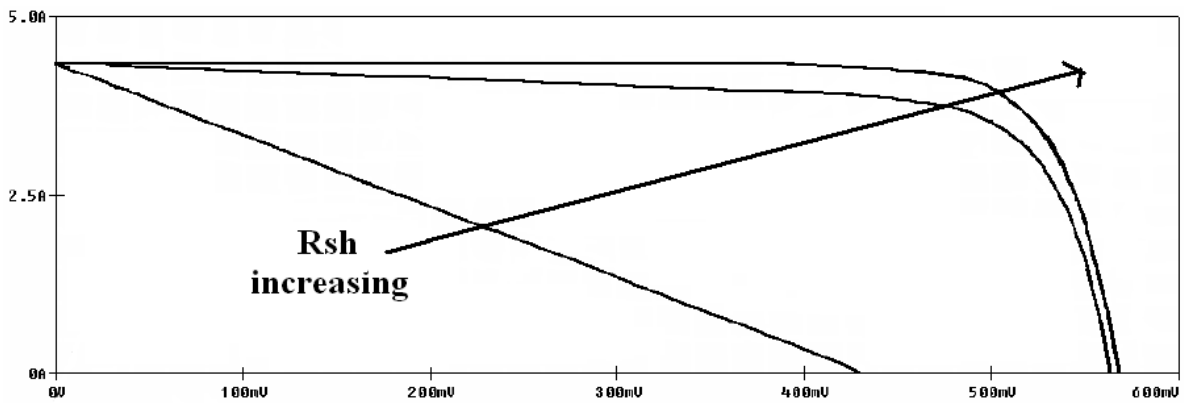


Figure 2.25: I-V characteristic of a solar cell with the change of R_{sh} .

Now we have to introduce the last losses component: recombination in the space charge region. We model it adding a diode to the equivalent circuit (Figure 2.25), so that the current flowing through that diode ($I_0'(e^{\frac{V+IR_S}{nV_T}} - 1)$) is subtracted to the total photocurrent (as shown in Figure 2.27, the total photocurrent will be reduced and, with it, the efficiency). The $I=f(V)$ equation taking into consideration this last losses factor is:

$$(2.94) \quad I = -I_0(e^{\frac{V+IR_S}{V_T}} - 1) - I_0'(e^{\frac{V+IR_S}{nV_T}} - 1) + I_L - \frac{IR_S + V}{R_{sh}}$$

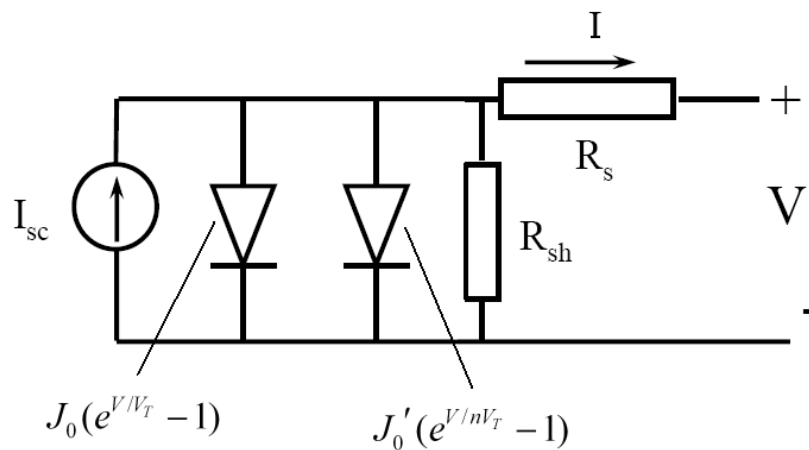


Figure 2.26: Equivalent circuit for a solar cell considering series resistance, shunt resistance and recombination effects.

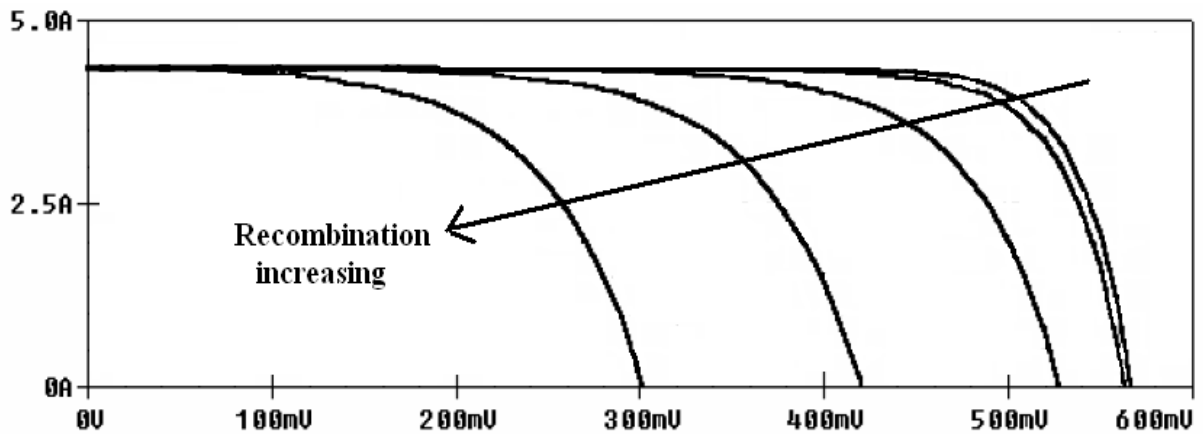


Figure 2.27: I-V characteristic of a solar cell with the change of the recombination in the space charge region.

This last circuit (shown in Figure 2.26) is the one we will simulate. To do that we call the nodes as shown in Figure 2.28, considering “girrad” the value of the irradiance (W/m^2). It is equal to:

$$(2.94) \quad girrad = \frac{J_{sc}A}{1000} G$$

Where G is simulated with a voltage generator, as we will see later. The code used to describe the circuit of Figure 2.28, is show in Figure 2.29 (we give to the parameters a default value of “1”).

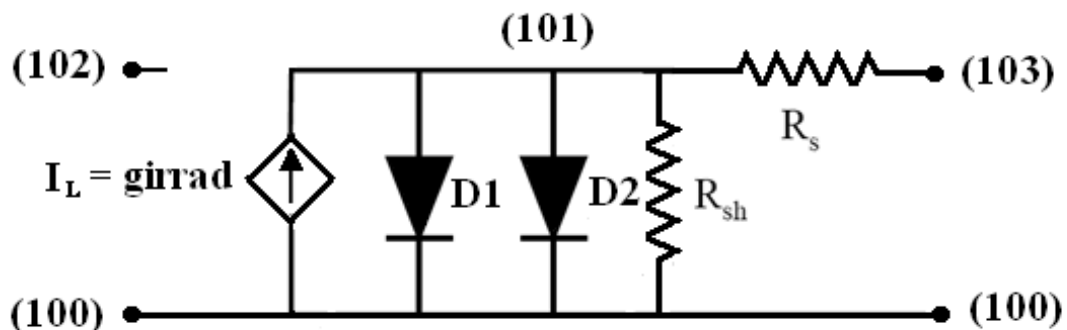


Figure 2.28: Circuit to simulate with names assigned to the nodes.

```
.subckt solar_cell 100 103 102 params:area=1, j0=1, jsc=1, j02=1, rs=1, rsh=1
r1 101 103 {rs}
r2 101 100 {rsh}
girrad 100 101 value={{jsc/1000}*v(102)*area}
d1 101 100 diode
.model diode d(is={j0*area})
d2 101 100 diode2
.model diode2 d(is={j02*area})
.ends solar_cell
```

Figure 2.29: Circuit description in PSpice.

Now we have to connect two generators to the circuit and assign the values (typical value) to the parameters. So we call the subcircuit of Figure 2.27 in another one, adding the two generators: the resulting circuit is shown in Figure 2.30. The PSpice code to call the subcircuit, to connect the two generator (V_{irrad}-Input; V_{bias}-Output), and to set the components to the wanted values (area=126.6 j₀=1e-11 j₀₂=1e-9 jsc=0.0343 rs=0.001 rsh=100000) is shown in Figure 2.31.

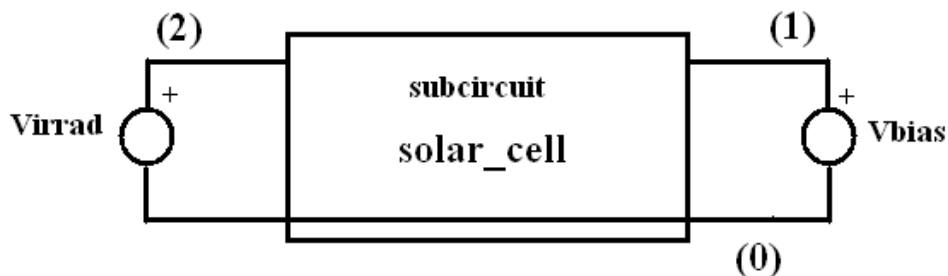


Figure 2.30: Circuit to simulate with generators connected.

```
.include cell.lib
xcell 0 1 2 solar_cell params:area=126.6 j0=1e-11 j02=1e-9 jsc=0.0343 rs=0.001 rsh=100000
vbias 1 0 dc 0
virrad 2 0 dc 1000
.plot dc i(vbias)
.dc vbias -0.1 0.6 0.01
.probe
.end
```

Figure 2.31: PSpice description of the circuit of Figure 2.30.

The results of our simulation is finally reported in Figure 2.32.

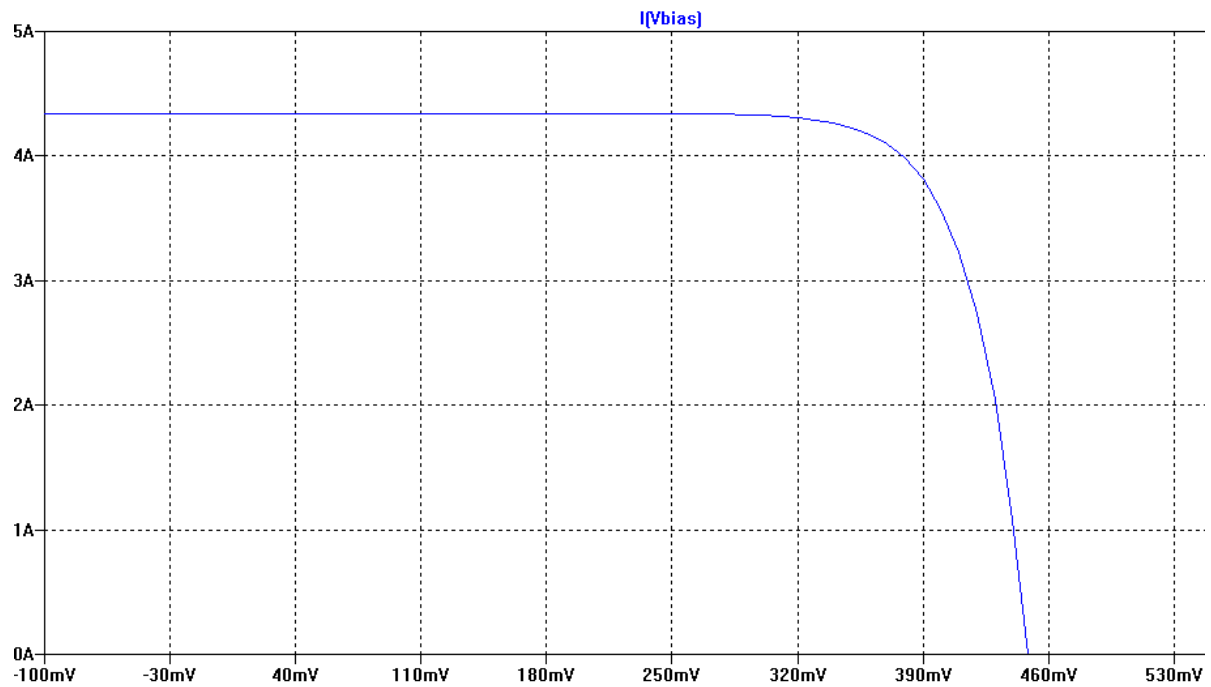


Figure 2.32: Results of the PSpice simulation representing $I(V_{bias})$.

Figure references chapter 2

Figures 2.1, 2.2, 2.3, 2.4, 2.5, 2.6, 2.7, 2.8 are from [5];

Figures 2.15, 2.21 are from [13];

Figures 2.16 is from [5].

3.

PROCESS EQUIPMENTS AND TECHNIQUES

3.1 Introduction to chapter 3

Our process involves different equipments and techniques we will introduce in the present chapter. We will start describing how a sputtering machinery works, which is probably the most important equipment in our manufacturing process, and afterwards we will introduce the other ones: photolithography, evaporator and laser. This section has no intention to introduce the way the equipments are used in the manufacturing process. It just want grant a broad background useful to well understand the process which will be introduced afterwards.

3.2 Sputtering

Sputtering is a technique used to deposit thin film materials, on substrates [4,9]. In the upper part of a close room, is put the substrate where the thin film will be deposited, while at the bottom of it, is placed the source material (the material we want to deposit), called

“target”. The closed room, after a period of air cleaning, while it is brought to a wanted pressure, a neutral gas is put in it (generally Argon - Ar). As shown in Figure 3.1, a negatively charged electrode staying under the target, accelerates the electrons present inside the room away from it. When accelerated electrons hit neutral Ar, this loses the outer shell electrons, so that it remains ionized (in the example shown in Figure 3.1, Ar loses one electron becoming Ar^+). When Ar is positively ionized, forming the so called plasma inside the sputter room, it is attracted by the negatively charged electrode (Figure 3.2), till it reaches and hits the target. Therefore, some particles of the target material are released for the impact together with other free electrons. The additional free electrons hit other neutral Ar atoms creating new positive charged ions. In this manner the loop that feeds the plasma is enabled. Not all the generated electrons feed the plasma, some of them meet positive charged ions of Ar, that change back into its neutral state, releasing energy in the form of photons. This is what makes the plasma glowing (see Figure 3.3).

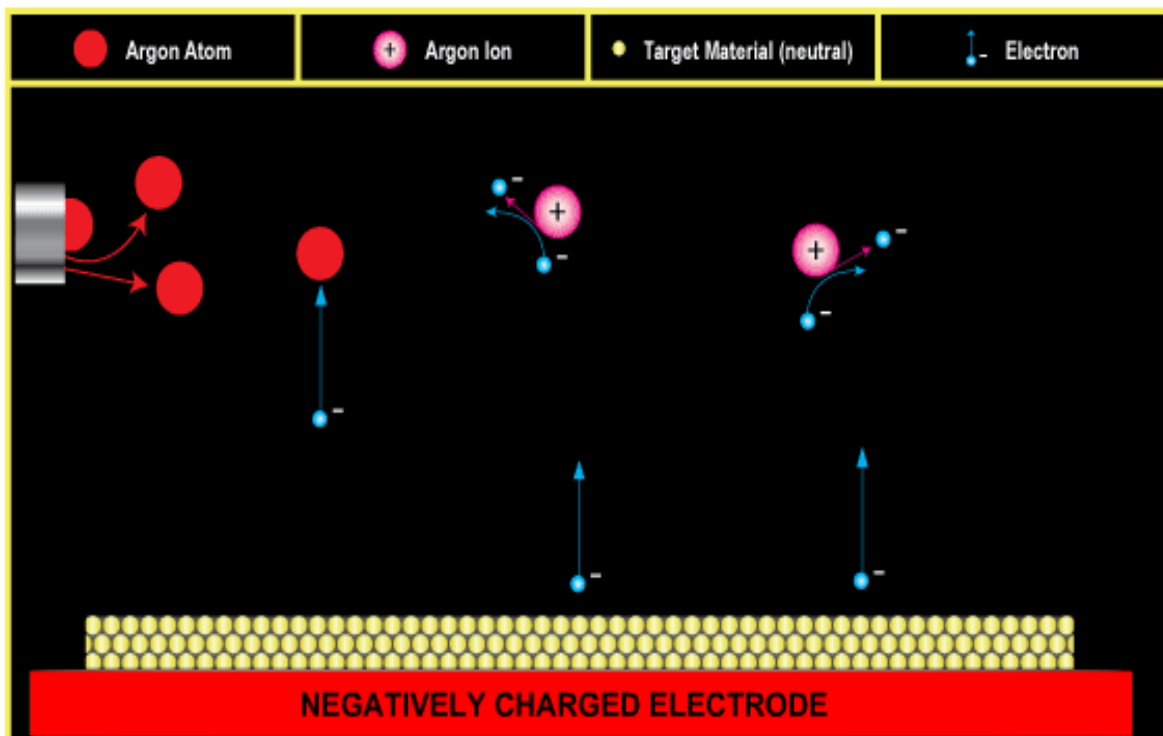


Figure 3.1: Sputtering; plasma making into a sputter room.

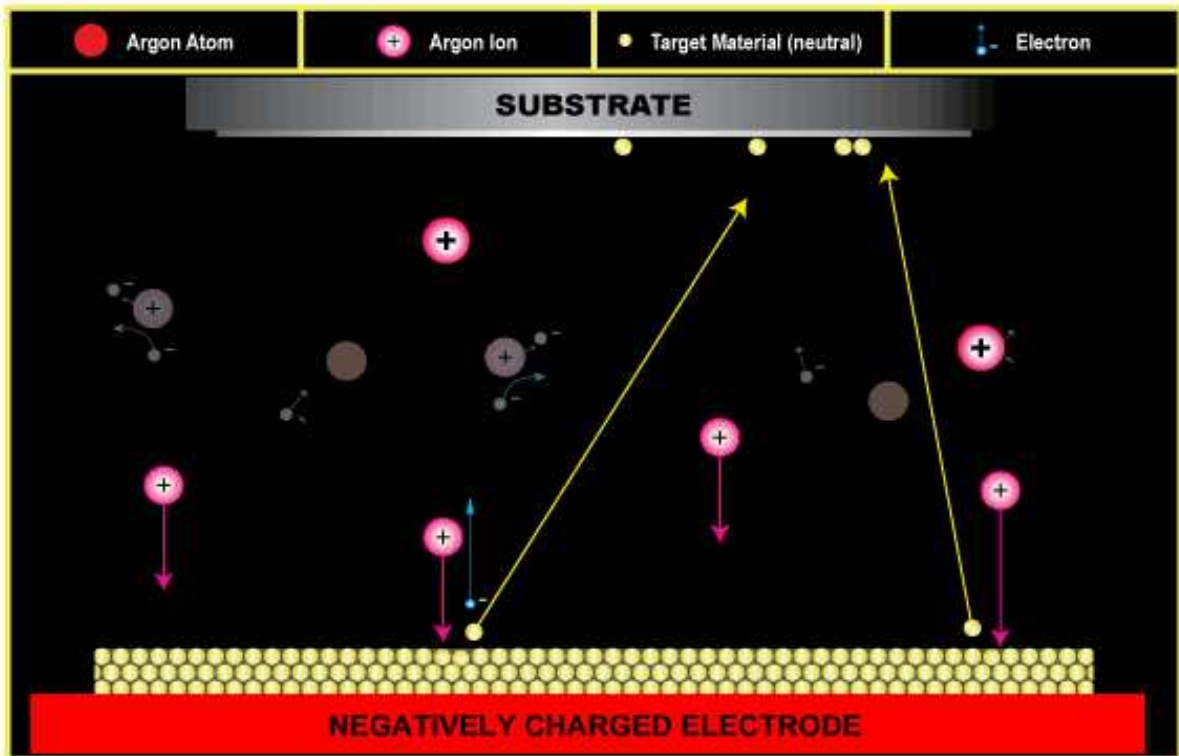


Figure 3.2: Sputtering; target hitting and deposition.

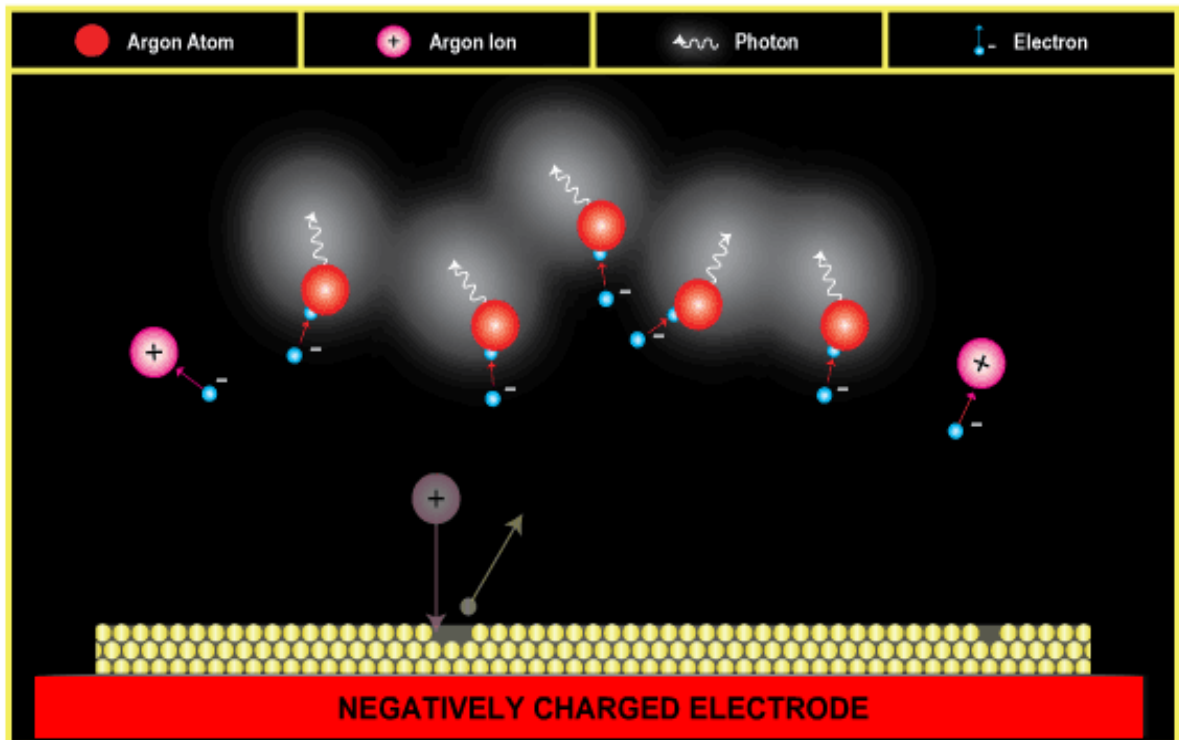


Figure 3.3: Sputtering; photon emission for electrons-ions recombination.

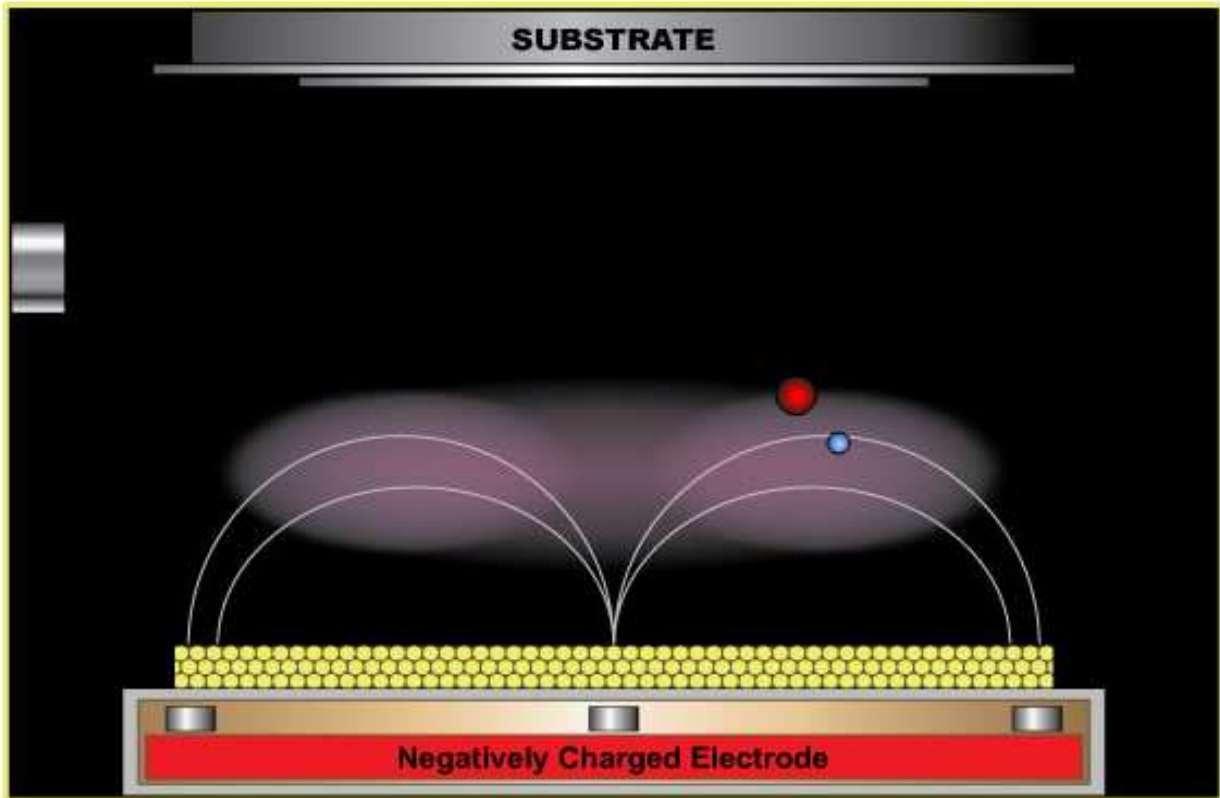


Figure 3.4: Magnetron sputtering.

The described sputtering technique, called “diode sputtering”, is certainly an efficient deposit technique, but it has two important problems. First of all the deposition rate is slow, causing long deposition time, secondly the accelerated electrons can hit the substrate causing its overheating and even damages on the surface. To overcome these problems the magnetron sputtering has been developed (that is the type of sputtering we use in our process). Using magnets located behind the cathode, free electrons will be trapped in the magnetic field generated by it, consequently electrons will not be free to bombard the substrate and, moreover, they will meet neutral Ar atoms more frequently, enhancing prominently the Ar ions formation. In the Figure 3.5 is shown the sputtering equipment we used in our process.



Figure 3.5: Sputtering equipment used in our process.

3.3 Photolithography

Photolithography [5] is a technique widely used in electronic manufacturing to remove, with high precision, certain shape of thin film materials deposited on a substrate. It is also used to define areas where deposit said thin film materials.

After a film of a certain material is deposited on the slice of substrate (for example 400 μm of Si or GaAs), it is necessary to remove some areas of it to create the desired device with the desired connections and physic characteristics (as said, another option is to define certain window on the substrate, where to deposit a thin layer of the desired material, for example with a sputtering equipment). This selective area definition is done with the use of a photosensitive material called "Photoresist", which is a liquid polymer that turns into a monomer when illuminated with Ultraviolet (UV) light. Hereinafter in this paragraph, we will describe a possible way to operate in a lithographic process.

In a photolithography process the first step is to put few drops of photoresist on a pre-polished wafer of substrate material, equally depositing it with a centrifuge (Figure 3.6). The photoresist is spread evenly, forming a film of thickness around microns. Then, it is placed a photo mask above the slice (usually of glass or plastic material), having transparent and opaque areas, corresponding respectively to areas where photoresist has to be removed, and area where it has to be left. The perfect alignment between the mask



Figure 3.6: Centrifuge for photoresist deposition.

and the slice is made with optical methods, using a machinery (mask aligner) like that showed in Figure 3.7. After the alignment, with the same equipment, the wafer is exposed to ultraviolet light: opaque areas of the mask will absorb the light, preventing it from reaching the wafer surface, while no protected area will be reached by the light and transformed into monomers. Eventually, the exposed wafer is put in a solution removing the photoresist turned into monomer.

Depositing a thin film material on the so treated wafer, only in the free photoresist areas it will get in contact with the substrate. After the film deposition, it



Figure 3.7: Mask aligner.

is possible to remove the photoresist protected by the black areas of the mask, leaving the wafer with the deposited material only in the area it is attached.

The described process is the so-called "positive". There is a different process, called "negative", in which windows are generated in correspondence with the non-illuminated areas of the wafer covered by resist.

3.4 Evaporator

An evaporator [7,8,9] is an equipment used to coat substrates with thin film materials (Figure 3.8). In general, it works evaporating (liquid) or sublimating (solid) in vacuum the material to be deposited, allowing its solidification on the target face. There are different evaporation methods: electron-beam method, in which the material to be evaporated is



Figure 3.8: Thermal evaporator.

heated by an high energy electron beam (up to 15 keV); flash evaporation method, in which a fine wire of material is continuously put in contact with a hot ceramic bar enabling its evaporation; resistive evaporation, that works injecting an high current in a resistive wire or foil, containing the material to be deposited; thermal method (the one we use in our process), that uses the thermal evaporation concept, namely, the evaporator works raising the temperature inside a closed room, till achieve the one for which the pressure is high enough to allow the atoms (or molecules) to split off from the surface. When split off, particles go toward the vacuum area upon them, moving through it, to finally achieve the target object (substrate), where they condense back to a solid state and form the mentioned coating. Evaporation seems give similar results to sputtering deposition, but there are some relevant differences: an evaporator equipment deposits faster than a sputtering machinery, and it is also cheaper, because of its less complexity. On the other hand, using the thermal effects, it has higher consumes and the density of the deposited films is lower. Moreover, with the thermal evaporation, targets may be decomposed by high temperature. But we have to state that also in sputtering the target surface should be damaged, especially for high power deposition.

heated by an high energy electron beam (up to 15 keV); flash evaporation method, in which a fine wire of material is continuously put in contact with a hot ceramic bar enabling its evaporation; resistive evaporation, that works injecting an high current in a resistive wire or foil, containing the material to be deposited; thermal method (the one we use in our process), that uses the thermal evaporation concept, namely, the evaporator works raising the temperature inside a closed room, till achieve the one for

3.5 Laser

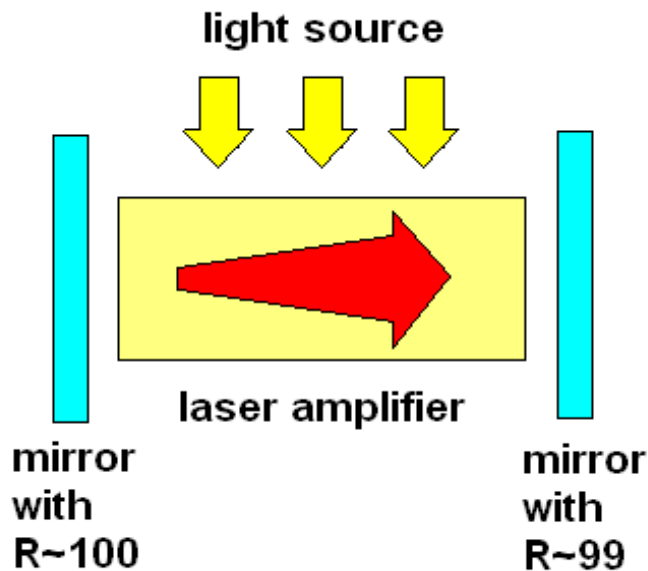


Figure 3.9: LASER oscillator.

A laser (Light Amplification by Stimulated Emission of Radiation) [8] or, more properly said, a laser oscillator, is an emitter light equipment formed by a laser media (amplifier) and a cavity (filter and feedback system). An optical media, or optical amplifier, generally is a material (dielectric and without free charges in it) that allows the amplification of the light getting through it. On the other hand, a cavity is a structure able to keep

an electromagnetic field at a given frequency.

To well understand the “optical amplification” concept (at the basis of the laser devices functioning), it is important to describe the most general optical amplification structure (Figure 3.9). It has two reflecting mirrors at two opposite extremes of the laser structure (the cavity), with a light amplifier in the middle (laser media). When in same way a light beam is generated (from an external light source), it continually goes through it, because of the window reflection, increasing in intensity until an equilibrium condition is reached. To send out part of the amplified beam, only one of the amplifier reflects mirror are totally reflective, the other one (the one that allow the light to go out) is partially reflective: it reflects about 99% of the incident light. In the dielectric light amplifier two physic phenomena take place: spontaneous emission and stimulated emission. Spontaneous emission is the process by which a light source, such as an atom in an excited state, undergoes a transition to the ground state and emits a photon. One way to excite

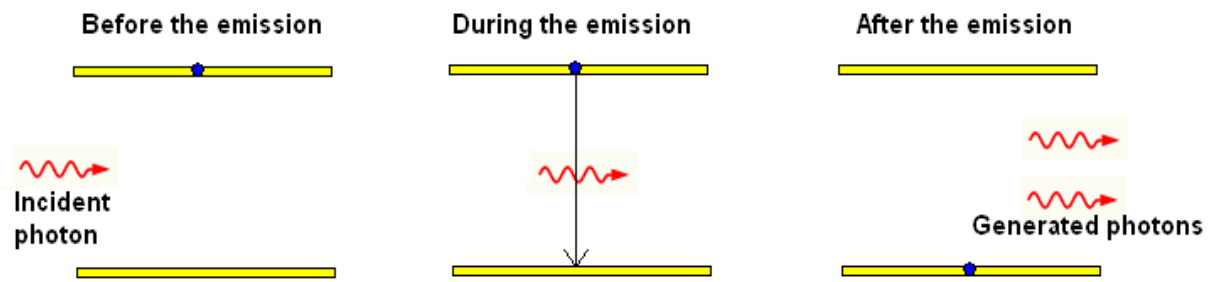


Figure 3.10: Stimulated photon emission.

light sources is the light itself. This occurs because of the matter structure formed by atoms, consisting of dense, central nucleuses surrounded by a cloud of negatively charged electrons, which should stay at different energy levels. The closer an electron to the nucleus, the lower the energy levels. When an electron absorbs enough energy, it passes to an higher energy level (instable state), and after, coming back to the original energy level (stable state) it emits photons (the corpuscular nature of the light). In any way the most important phenomenon in a laser is not spontaneous emission but stimulated emission (the phenomenon that causes light amplification). When energy is absorbed in the gain medium (that we have called light amplifier), as seen, it produces excited states in the atoms, and when the number of particles in one excited state exceeds the number of particles in the ground state, population inversion is achieved and the mechanism of stimulated emission can take place. Stimulated emission (Figure 3.10) is the process by which an electron, perturbed by a photon having the correct energy, may drop to a lower energy level, resulting in the creation of another photon. So it is similar to spontaneous emission but with two important difference: it is generated for a perturbation of a photon and it generates a new photon. The result is that from one photon (the incident) are emitted two photons (the incident more the generated): this is the way by which the light gain is achieved in an optical amplifier. The final result of this process is the optical pumping of the laser device at a certain wavelength.

Obviously the above description is far away to be complete, it wants just to give a general description of the laser equipment parts and a broad idea about how it works. For instance, we have presented the laser emission process using two energy levels. A rigorous analytical treatment (out of our scope) shows that actually, it is not possible to obtain a

laser emission with two energy levels but, to take place, it needs at list three of them. In practice are common lasers with three or four energy levels producing stimulated emission.

There are different types of laser oscillator, the one we use in our solar cell process (shown in Figure 3.11), is the Nd:YAG (neodymium-doped yttrium aluminium garnet; $\text{Nd:Y}_3\text{Al}_5\text{O}_{12}$). It is a laser belonging to Neodymium family (one of the most versatile and widely used laser), in which the medium amplifier is the YAG (Yttrium Aluminium Garnet $\text{Y}_3\text{Al}_5\text{O}_{12}$). As shown in Figure 3.12, it has a four energy levels structure and its emits photons at the wavelength of $1.06 \mu\text{m}$.



Figure 3.11: Laser oscillator Nd:YAG.

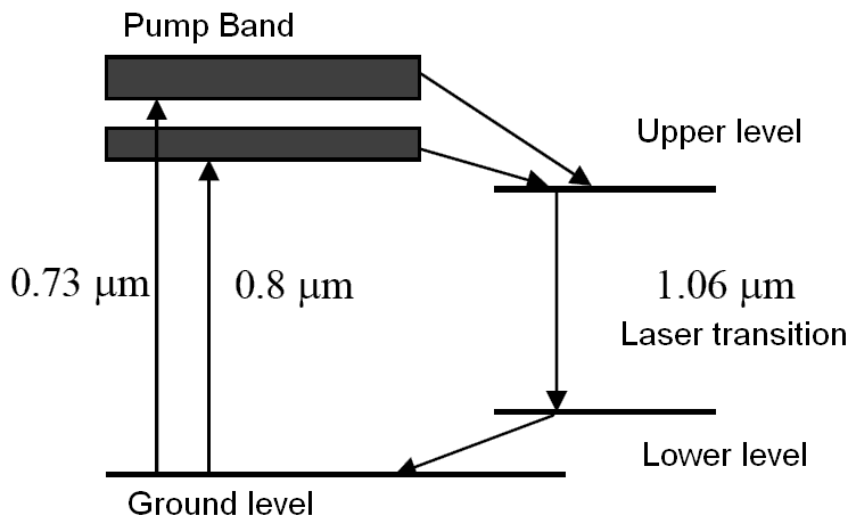


Figure 3.12: Stimulated emission in Neodymium laser (four energy levels structure).

In order to well understand the laser parameters setting we use in our process, is important to spend few more words about this device. There are two possible working regimes for a laser: continuous wave and pulsed, with the second one greatly more intensive because all the energy is concentrated in thin pulses. In our process we work in pulsed regime (Figure 3.13). Therefore in order to modulate the intensity we can vary two parameters: the pulse repetition rate (f_{rate}), and the maximum intensity of the pulse.

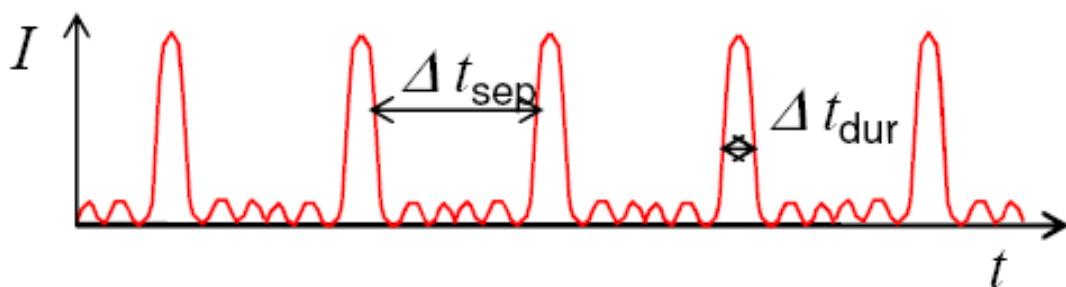


Figure 3.13: Pulses of a pulsed laser oscillator.

Figure references chapter 3

Figures 3.1, 3.2, 3.3, 3.4 are from [5];

Figures 3.12, 3.13 are from [10].

4.

EXPERIMENTAL MEASUREMENTS AND PROCESS DEVELOPMENT

4.1 Introduction to the chapter 4

This chapter is about the experimental measurements involved in our work, with the relative information extracted. We will provide also the description of the first manufacturing processes, reporting drawback and possible improvements. First of all, we will introduce the general structure of our solar cell, and then, we will report about the work done to develop it.

4.2 The solar cell structure

The structure of our Metal - Semiconductor solar cell (shown in Figure 4.1) has, as main constituting parts, the metal (ITO - Indium tin oxide) and the semiconductor substrate (p-doped GaAs). In the back side of the substrate, the ohmic contact is done with a layer of Zn

covered by Au. Zn is also the element used to dope the GaAs substrate, so the idea is to obtain an high doped GaAs area in the back side of the substrate covered by Au, to finally obtain the ohmic contact. In the front site of the GaAs substrate, ITO is deposited in order to make the metal (ITO) – semiconductor (GaAs) junction. Eventually, on the ITO layer, an Au coating opportunely shaped is put (planar view of Figure 4.1).

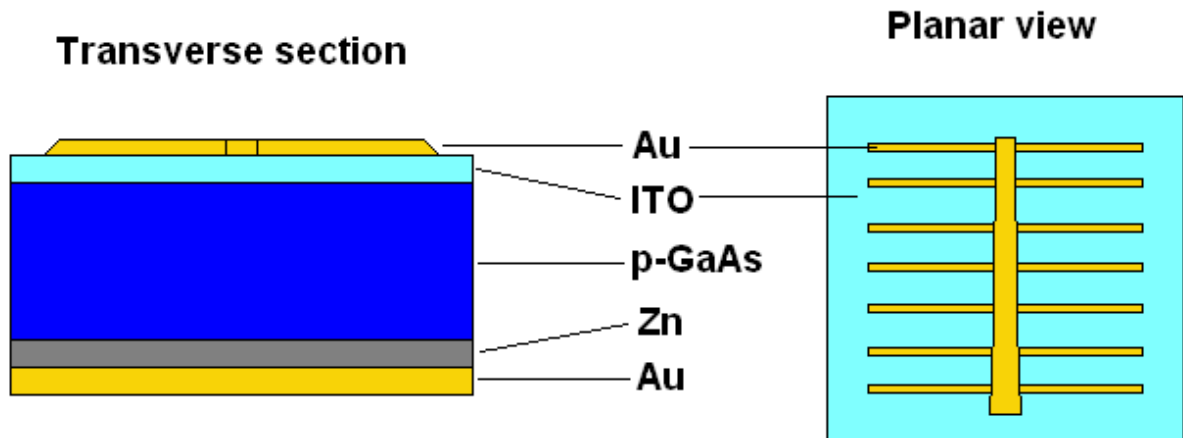


Figure 4.1: Metal-Semiconductor solar cell structure.

Despite the simplicity of the structure, its development involves a lot of different experimental tests and measurements. In particular, different parts of the making process have to be investigated, before the fabrication of the solar cell on the whole. We first developed singularly three different aspects involved in the fabrication:

- ITO deposition;
- Ohmic contact making process;
- Cleaning and passivation.

Only at the end of this investigation phase, we can be reasonably able to make the entire process. Indeed, first we will relate the information coming out from the experimental measurements carried out for each singular aspect reported above, and finally we will propose some complete processes of fabrication, relating limits and possible improvements.

4.3 ITO: general concepts and experimental measurements

The ITO deposition is probably the most important aspect of our work, in fact we have to meet the best deposit conditions in order to do not damage the GaAs interface, but also we have to obtain good resistivity values for the ITO layer. In fact, ITO is used as metal in a Metal-Semiconductor junction, but to behave actually as a metal, it must have a good resistivity (namely, a low resistivity). In the following two sections, we will report some important theoretical aspects of the ITO material and, afterwards, our experimental results related with them.

4.3.1 Definition and main characteristics of ITO

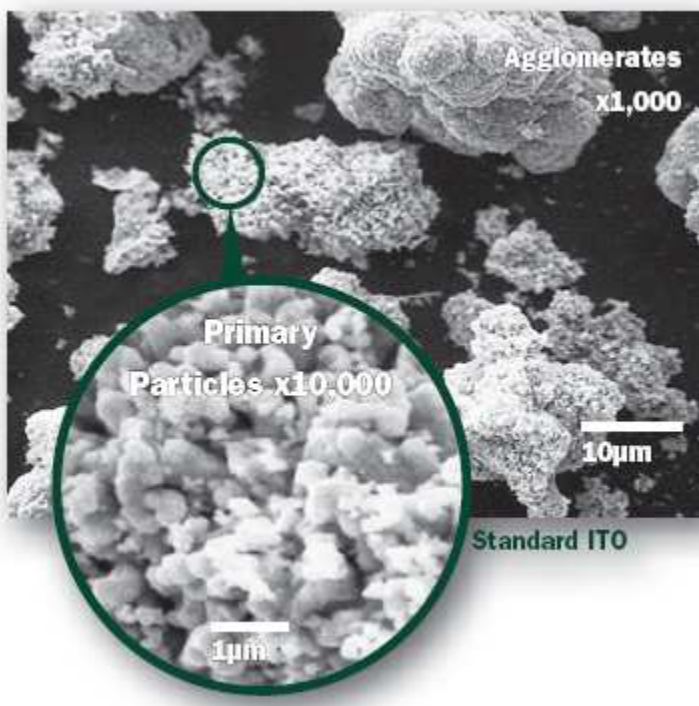


Figure 4.2: ITO seen under a microscope.

ITO (Indium Tin Oxide – Figure 4.2) is a solid material composed of Indium Oxide (In_2O_3), and an inorganic compound, the tin oxide (SnO_2). Typical percentage values of weight composition are In_2O_3 - 90%, SnO_2 - 10% [28]. It is generally used as a transparent conductive material, in fact, it has the particular properties of excellent visible light transparency and high

electrical conductivity. More precisely, ITO is a heavily doped n-type semiconductor with a bandgap between 3.5 and 4.3 eV (depending on its composition and preparation method) and, with such a bandgap, it allows the passage of light for wavelength higher than 400 nm (transmitting between 70% and 90% of radiation). For wavelengths below 310 nm it is

completely opaque to light [29]. These characteristics make ITO a material of crucial importance for some applications in photovoltaic and optical devices field.

ITO deposition can be carried out by a number of methods (by electron beam evaporation, physical vapor deposition, or a range of sputter deposition techniques) among which the magnetron sputtering is the one used in our process. It is necessary to note that a compromise has to be reached during ITO film depositions, as an high concentration of charge carriers causes an improvement of the ITO layer conductivity (that is a positive point for us), but also a fall in its transparency (that is, on the contrary, a drawback) [26].

An important aspect of the ITO deposition is the thickness we want to obtain. When the film thickness decreases below a critical value, the electrical properties of the indium oxide and ITO films were found to deteriorate drastically. This value depends on the control parameters used for the deposition process, but generally we can assume that a “good value” for ITO thickness is about 100 nm, also considering the optical properties [26-27-30]. In fact, results reported in [30] show that the percentage of transmitted light is equal to 80% for a 90 nm thick ITO film, and 92% (peak value) for a 640 nm thick film (transmittance measurements of deposited-ITO films, on glass substrates, have been found to exhibit an increase in transmittance in said range, 90 – 640 nm, so that for our process of deposition we assume to chose a value in this range). Although the best value for the transmittance of ITO layers is about 640 nm, the thickness of the highly transmittive ITO layer which is required if the layer is to be used as antireflective coating on GaAs solar cell was calculated to be around 90 nm. Hence, considering that ITO plays an important role in our process also as antireflection coating, we assume to find (for our cell) a thickness of about 90-100 nm.

4.3.2 ITO deposition and experimental results

The experimental results concerning the ITO deposition are about its resistivity when deposited on a substrate (that in this stage is a microscope slide of plastic, but in the final process will be the GaAs wafer). It is not possible to calculate directly the resistivity value, so that we have first calculated the sheet resistance values, afterwards we have eliminated

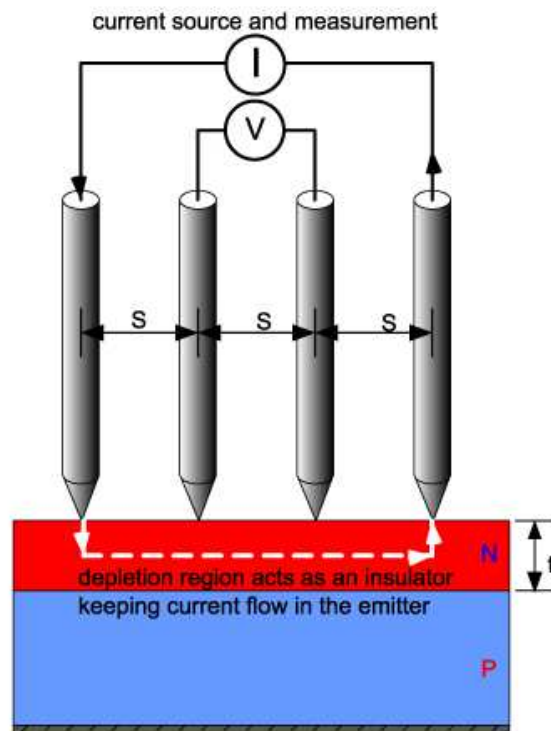


Figure 4.3: Four point probe for sheet resistance measurement.

some defined area of ITO (using lithography process) and, eventually, calculated the ITO thickness: from the sheet resistance and the thickness values is then easy to calculate the resistivity of the deposited ITO.

It is Known that, for a general sample with well known dimensions and resistivity value, we can calculate the resistance as

$$(4.1) \quad R = \rho(L/A)$$

where R is the resistance of the sample, ρ is its resistivity, L its length, and A its cross-section area.

We know also that

$$(4.2) \quad A = W \cdot t$$

where W is the width and t the thickness, then we can also write

$$(4.3) \quad R = \rho \frac{L}{Wt}$$

However, by grouping t in ρ , we obtain

$$(4.4) \quad R = R_s \frac{L}{W}$$

where $R_s = \rho/t$ is the sheet resistance.

From the last formula, knowing R_s and t , we obtain ρ (that is our scope). As said, t is calculated after a lithography process, with thickness measurement equipment, while the sheet resistance is calculated with four point probe equipment (Figure 4.3). It works injecting a current through the outer probes and measuring the value of the induced voltage through the inner probes: dividing the voltage by the current it calculates the sheet resistance value. It is important to note, as this kind of measurement is possible for thin layer material (for small values of t , namely from $t \sim 10^{-9}$ to $t \sim 10^{-6}$). This is because for thicker layer, the current distribution is not homogeneous inside the material (it changes with t), so that the above reported formulas for the sheet resistance calculation, are not still valid.

The ITO deposition has been carried out using an ESM100 Edwards & RFS5 Generator-300 W sputtering system with the following condition: base pressure equal to $4 \cdot 10^{-3}$ mbar; Ar flux equal to 10 sccm; RF input power varying from a minimum of 14 W to a maximum of 30 W.

In Figure 4.4 the bar chart of the resistivity values (in Ωm) with different power deposition values (in W) is shown. As we should expect, the resistivity values heavily depend on the power deposition; lower the deposition power, higher the resistivity. The difference is considerably: the values spread from about $1.7 \cdot 10^{-3}$ Ωm for a deposition power equal to 30 W, up to 0.1 Ωm in correspondence of 14 W. This is a bad trend for us, because we want a low resistivity, but also a low deposition power, for preventing substrate surface damages (we refer to the substrate upon which the ITO layer is deposited). The optimal trade-off is to be found, but we generally want to avoid a power as high as 30 W, trying to attain sufficiently good resistivity value using power depositions lower than 20 W.

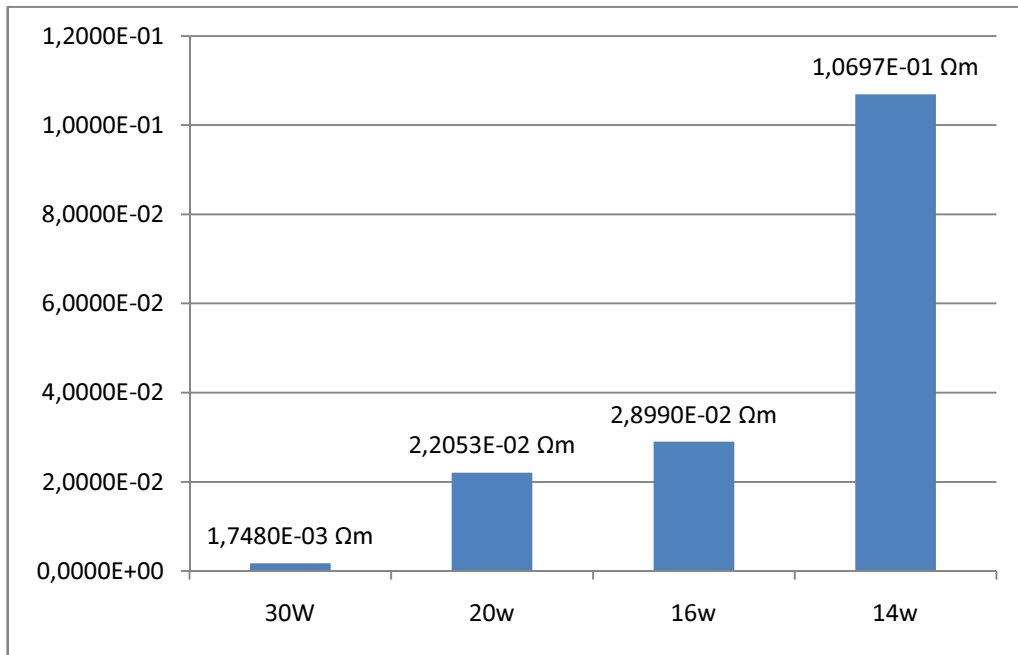


Figure 4.4: resistivity value as a function of the deposition power.

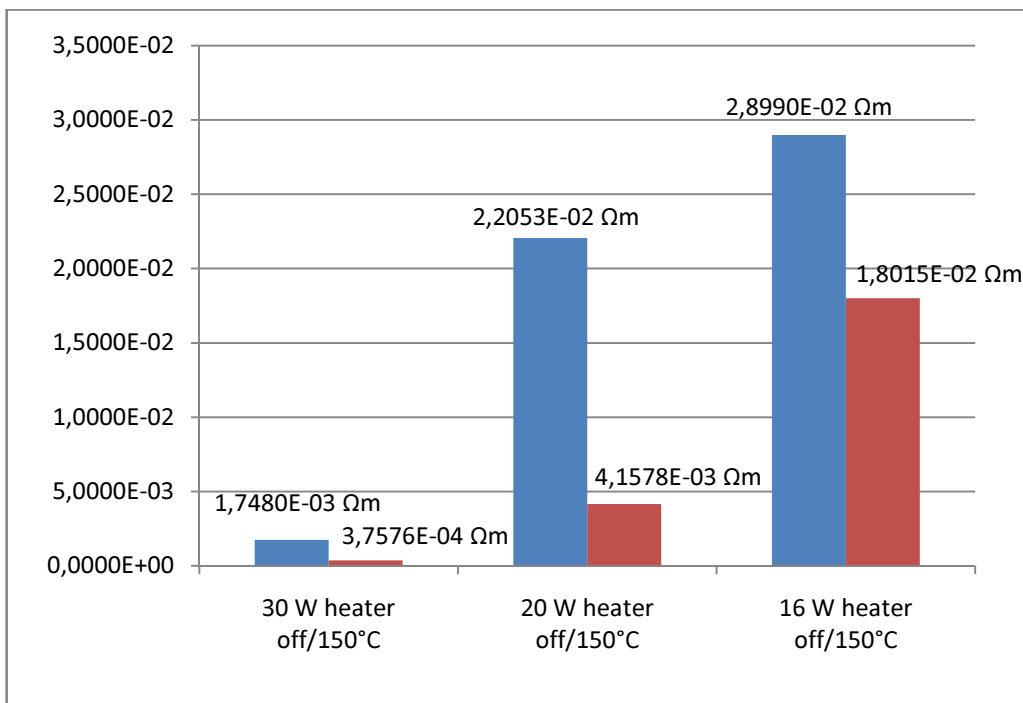


Figure 4.5: resistivity value as a function of the power for room temperature and 150 °C depositions.

Another factor affecting the resistivity is the temperature of deposition. We tried to deposit both, at room temperature and at 150 °C (the temperature value commonly claimed to be the ideal one for ITO deposition). The results actually show a dependence of the resistivity on the deposition temperature. Also in this case, we cannot be sure of using the best condition in term of temperature (that is 150 °C) for the final process. In fact, high temperatures can damage the surface where the ITO layer is deposited and, moreover, can create forces such as strain, so that the advantages got by using higher temperatures should be replaced or even overtaken by the interface irregularities. The questions about the ITO deposition temperatures and, more broadly, about the temperature effects on the process on the whole, will be revised in the sections relating to the solar cell fabrication processes.

We observe that not all the achieved improvement at 150 °C can be imputed to the higher temperature. In fact, to assure higher deposition temperatures, we need to use a heater supporter, having a distance from the target of 4.5 cm, while the distance for the normal supporter (without heater device) is one centimeter more (about that, we have to remark as the values reported in Figure 4.5 have been calculated for depositions carried out using the heater support, once off and once keeping a temperature of 150 °C). As we can see in Figure 4.5, just for a little variation in distance (in our case, 1 cm), the variation in resistivity is considerable, particularly, resistivity is almost the half for the shorter distance. The values reported in Figure 4.6 have been obtained for a deposition power of 20 W.

Although the deposition carried out with a closer support seems to be the right choice, it is probably necessary to take into consideration as a closer distance should bring more surface damages, because the particles leaving the target arrive with higher velocity.

Another important factor affecting the resistivity is the pressure obtained in the camera of the sputtering machinery before the deposition process. In particular, lower values of pressure allow lower resistivity values (Figure 4.7; values obtained for a deposition power of 20 W). This is the only factor (among the ones affecting the ITO resistivity), that does not seem to have contraindications, so that, even if we have to take into consideration also the other factors (temperature, distance, power deposition) always

seeking a compromise, we can reach good resistivity values (even in absolute term) just bringing the camera as a minimum value of pressure as possible, before the deposition stage. To tell the truth, the better results achieved with low residual pressures, are not completely for free. To obtain Lower values of pressure is necessary more time to reaching it, and the dependence with the resistivity is not linear, but has an exponential trend. In this view, the compromise is to use a low pressure not too hardly achievable in term of time.

As final annotation, we do not have to confuse the pressure we have spoken about in this section, with the deposition pressure; the first one is the pressure to which the camera is brought before the deposition (residual pressure), the second one is that one kept by the camera during the deposition process. The residual pressure is related to a first “cleaning camera” process, for which the camera is bring to low pressure and contaminant particles are sucked away from it, indeed, lower the pressure, lower the impurity rate inside the camera during the deposition.

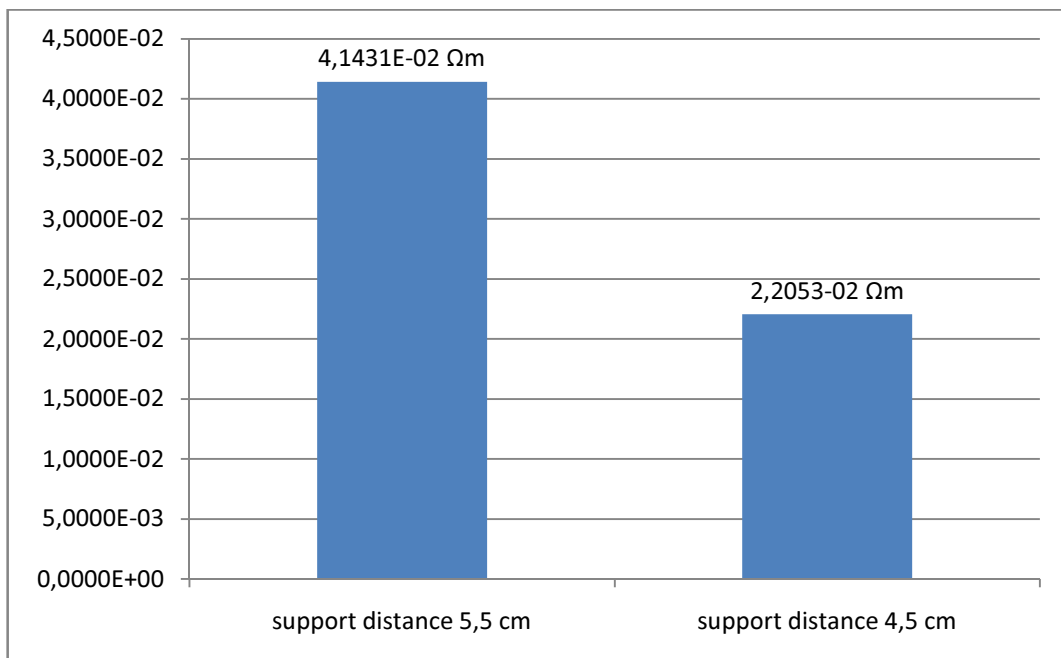


Figure 4.6: resistivity value as a function of the microscope slide distance from the target.

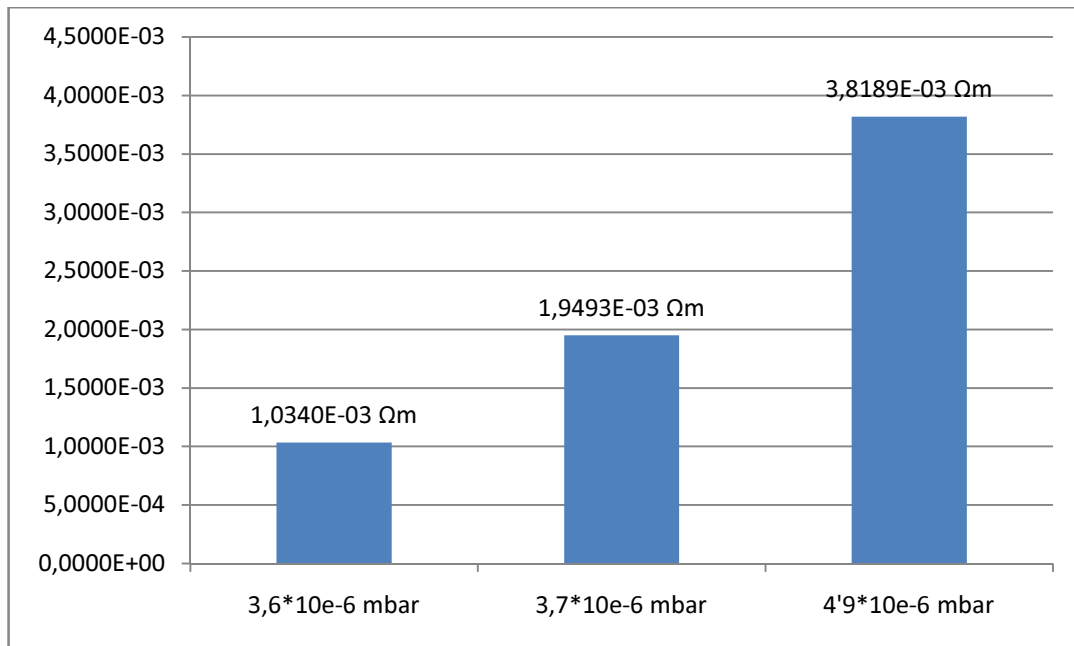


Figure 4.7: resistivity value as a function of the camera pressure before the deposition phase.

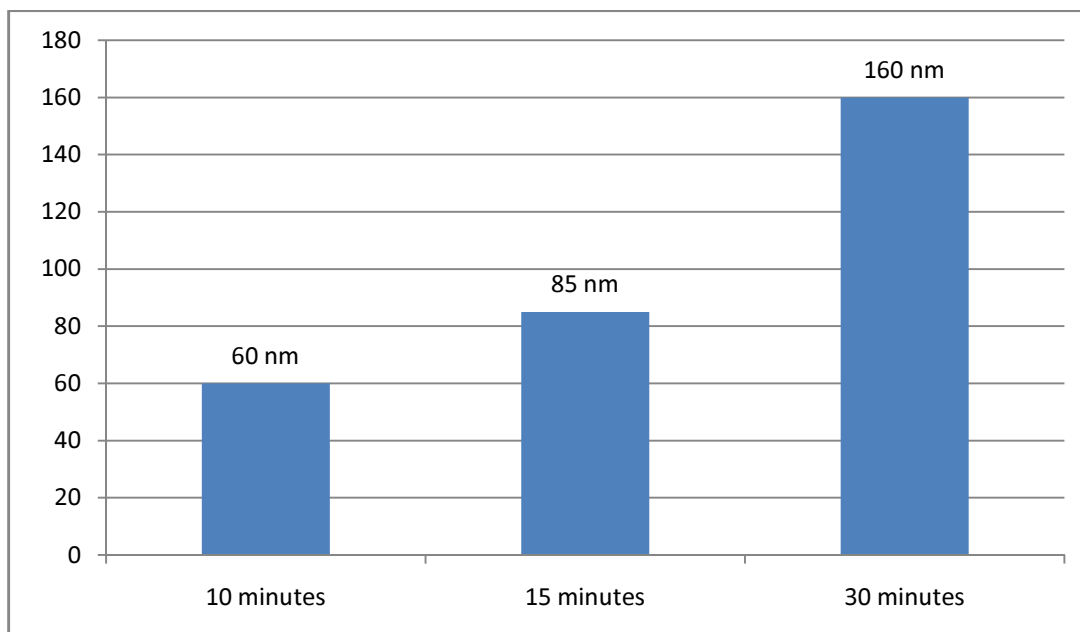


Figure 4.8: ITO thickness as a function of the deposition time.

As the ITO thickness is important in the context of our work, we have analyzed its variation in terms of time (the most important affecting factor). Figure 4.8 shows a bar chart reporting three thickness values for three different deposition times (the values are for a power deposition of 20 W). As we want ITO layers of about 100 nm, we have to use a deposition process lasting 15-20 minutes.

We have presented the ITO material, as a transparent material, but we need to analyze how much transparent it is. Namely, we need to analyze the transmittance of the ITO layers (deposited on the microscope slides that, for approximation, we assume to have a transmittance of 100%). Transmittance (T) is defined as the fraction of incident light passing through a sample, and it is generally represented as a function of wavelength. If I_i is the input intensity, and I_o is the light at the end of the sample:

$$(4.5) \quad T = \frac{I_o}{I_i}$$

and, in percentage terms,

$$(4.6) \quad T(\%) = \frac{I_o}{I_i} \cdot 100$$

Moreover, as we have said before, we should find a compromise between ITO resistivity and ITO transmittance, so that, we have to analyze if this compromise is met for the sample reporting the best resistivity values (or at list, the best values representing a compromise considering also the resistivity factor).

The results of our experimental measurements show that there is not a strong variation of the transmittance among our different deposited-ITO samples (obtained for different deposition conditions). In this view, we can assume that transmittance is not a critical problem in our process. In Figure 4.9 is shown the transmittance on function of wavelength for an ITO layer deposited on a substrate of glass material with the following conditions: power 20 W, pressure during deposition $4 \cdot 10^{-3}$ mbar, pressure before deposition $2.3 \cdot 10^{-6}$ mbar, Ar flux equal to 10 sccm, time of deposition 15 minutes, target-support distance equal to 4.5 cm, room temperature. As we can see from the Figure 4.9, the transmittance values are pretty good for all the wavelength of interest. There is a 100% of transmittance from about 440 nm to about 420 nm and, for wavelength values higher

than 420 nm, transmittance is always floating between 85 and 95%. After 1,1 μm , the resulting transmittance is a little lower, but never below 80%.

The transmittance results obtained from the other samples are almost the same of the ones shown in Figure 4.9. So that we can assume to have a good transmittance in our deposition conditions.

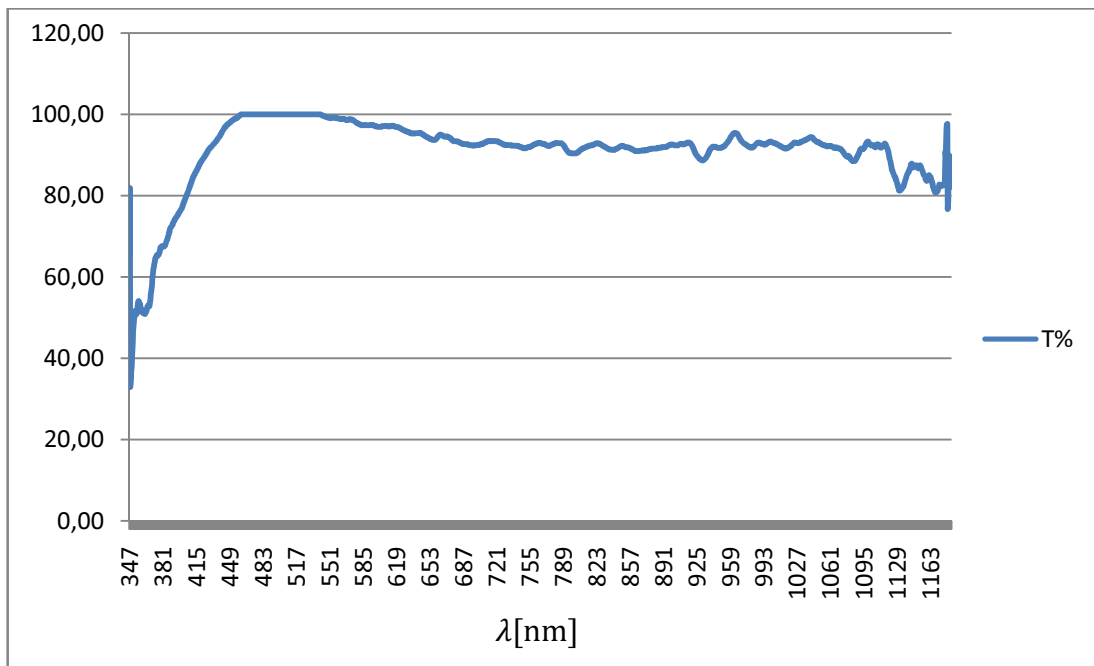


Figure 4.9: ITO transmittance as a function of the wavelength.

An important point to remark is that the experiments carried out using glass slides (as we have done in this phase) instead of real GaAs substrate, have the important advantage to prevent an excessive waste of GaAs sample, but the value obtained with them are not automatically valid also for GaAs substrate; in other words, it is not the same to deposit ITO on glass or on GaAs material. However, the differences are not enormous; namely, they are little enough to justify the use of microscope glass slide at this stage.

4.4 Ohmic contact

4.4.1 Definition of the main parameters and Au/Zn ohmic contact

The contact resistance is not always clearly defined. It is a concept pretty easy to understand, but less easy to define. In particular, is not always clear what component of resistance it includes: it certainly includes the resistance of the metal-semiconductor contact (also called “specific interfacial resistivity”, ρ_i), but it also includes a portion of the metal immediately above the metal-semiconductor interface, and a portion of semiconductor immediately below such junction. Moreover, it can include interfacial oxides and intermediate layer that may be present between the metal and the semiconductor.

The current density J of a metal-semiconductor contact depends on the applied voltage V , the barrier height ϕ_B and the doping density N_D [14], so that we can write the current density as a general function depending on said variables:

$$(4.7) \quad J = f(V, \phi_B, N_D)$$

Apart from the contact resistance (measured in ohm), we can define the specific contact resistivity, ρ_c (ohm·cm²), obtained dividing the contact resistance by the area (A) of the contact. We can also define a specific interfacial resistivity ρ_i (ohm·cm²) as follows:

$$(4.8) \quad \rho_i = \left. \frac{\partial V}{\partial J} \right|_{V=0}$$

also defined as:

$$(4.9) \quad \rho_i = \left. \frac{\partial V}{\partial J} \right|_{A \rightarrow 0}$$

where A is the contact area. The difference between ρ_c and ρ_i is that the last one includes the resistance of the metal-semiconductor interface only, whereas the first one includes the resistance of the metal-semiconductor contact, but also a portion of metal and semiconductor close to the junction. Despite ρ_i seems to represent more faithfully the quality of an ohmic contact, it is not actually measurable. The parameter that is

measurable is the specific contact resistivity. For this reason, it is used to find ρ_c to determinate the quality of an ohmic contact.

4.4.3 Experimental process of deposition

Unlike the schottky contact, the I-V characteristic of an ohmic contact has a linear (or quasi-linear) trend. In order to obtain such a figure, we have deposited a layer of Zn on the back side of the GaAs substrate, and on it, a second layer of Au. Both depositions have been carried out with sputtering machinery. In reality, the only Zn deposition is enough to establish an ohmic contact (while Au directly deposited on p-GaAs substrate does not give an ohmic contact), but the Au layer is fundamental for ensuring a protection to the Zn-GaAs ohmic contact and, moreover, for reducing such resistance (of about an order of magnitude) [31]. It is important to say as the behaviour of Zn and Au in reality depends on the GaAs substrate used. In our case the Zn has the role to improve the Au adhesion, because it is not generally good if such Au covering is not present.

The Zn deposition has been carried out on a p-GaAs substrate, using an ESM100 Edwards & RFS5 Generator-300 W sputtering system with the following conditions: pressure equal to $5 \cdot 10^{-3}$ mbar; Ar flux equal to 10 sccm; RF input power equal to 50 W; T_D (deposition time) = 1 minute. The Au deposition has been done with the same equipment (without opening the sputtering camera) and with the following conditions: pressure equal to $5 \cdot 10^{-3}$ mbar; Ar flux equal to 10 sccm; RF input power equal to 50W; $T_D=15$ minutes. Before the Zn deposition an inverse sputtering is carried out (to clean the GaAs surface), lasting 5 minutes and with pressure = $8 \cdot 10^{-3}$ mbar, Ar flux = 10 sccm and RF input power = 50W. Irregularity caused by the inverse sputtering do not affect badly the ohmic contact quality, but in general a GaAs surface with some irregularity, unlike the schottky contact, is even able to lead to better ohmic contact. As final step, after the Au-Zn layer deposition, a thermal annealing (at $T=400^\circ\text{C}$) is made to finally establish the ohmic contact.

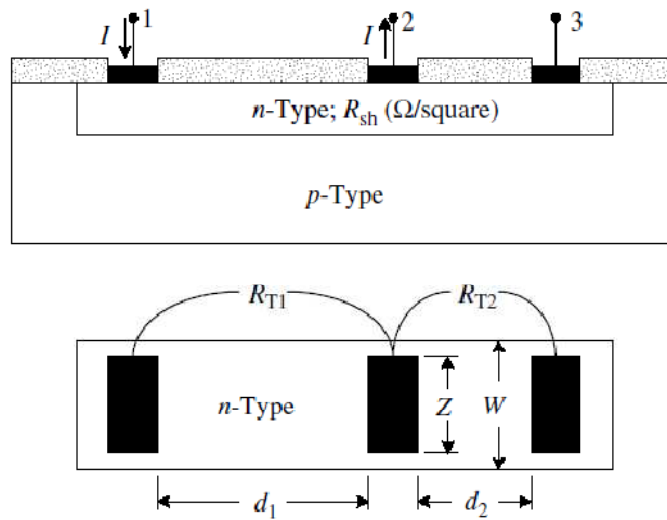


Figure 4.10: Multiple-contact, two-terminal contact resistance test structure (Z =contact width, contact length= L , diffusion width= W).

4.4.2 Method of measurement and results

For ohmic contact measurements, there are four main techniques: two-contact two terminal, multiple-contact two-terminal, four-terminal, and six-terminal methods. As said, none of these methods is capable of determining the specific interfacial resistivity ρ_i , but they determinate the specific contact resistivity ρ_c . It is, therefore, difficult to compare theory with experiments because theory cannot predict ρ_c accurately and experiments cannot determine ρ_i accurately.

The method we used for our experimental measurements is the TLM (transmission line method), that is a multiple-contact two-terminal method. In particular, we have modified such method to be able to measure contact resistance fabricated on a thick surface (that is our case). Before introducing the description and the results of our modification, we refer the characteristics of a general TLM as reported by Schroder in [14].

In a multiple-contact two-terminal method, in its most general form, three identical contacts are made (Figure 4.10). The distances between each contact are d_1 and d_2 .

Assuming identical contact resistances, as approximation, for each one of the three contacts, we can calculate the total resistance as follows:

$$(4.10) \quad R_{Ti} = \frac{R_{sh}d_i}{W} + 2R_c$$

Where R_T is the total resistance measured between two contacts, d is their distance, R_{sh} is the sheet resistance of the substrate, W is the diffusion width, R_c is the contact resistance, $i= 1$ for distance 1 and 2 for distance 2. Solving for R_c gives:

$$(4.11) \quad R_c = \frac{(R_{T2}d_1 - R_{T1}d_2)}{2(d_1 - d_2)}$$

When current flows from the semiconductor to the metal, it encounters the contact resistance R_c and R_{sh} . Therefore, the potential distribution under the contact, determined by both ρ_c and R_{sh} , is equal to:

$$(4.12) \quad V(x) = \frac{I\sqrt{R_{sh}\rho_c}}{Z} \frac{\cosh[(L-x)/L_T]}{\sinh(L/L_T)}$$

where L is the contact length, Z the contact width, x a general point of the contact length (with $x=0$ in the middle) and I the current flowing into the contact. According with equation (4.12), the voltage is higher near the point $x = 0$ and drops exponentially with the distance from that point. The “1/e” distance of the voltage curve is defined as the transfer length L_T :

$$(4.13) \quad L_T = \sqrt{\rho_c / R_{sh}}$$

The transfer length can be thought of as that distance over which most of the current transfers from the semiconductor into the metal or from the metal into the semiconductor [14]. In fact, it can occur that only a minimum part of the total ohmic contact surface is involved in this current transference ($L_T < L$), but it is also possible the case in which the current is almost the same for all the ohmic contact surface ($L_T \geq L$).

We will now consider the contact measurement configurations of Figure 4.11, with the current flowing from contact 1 to contact 2 and with the voltage measured at the same points. With R_{cf} (contact front resistance) we refer to the resistance calculated between two general contacts.

Considering equation (4.12), we obtain (providing $Z=W$ as approximation):

$$(4.14) \quad R_{cf} = \frac{V}{I} = \frac{\sqrt{R_{sh}\rho_c}}{Z} \cosh(L/L_T) = \frac{\rho_c}{L_T Z} \coth(L/L_T)$$

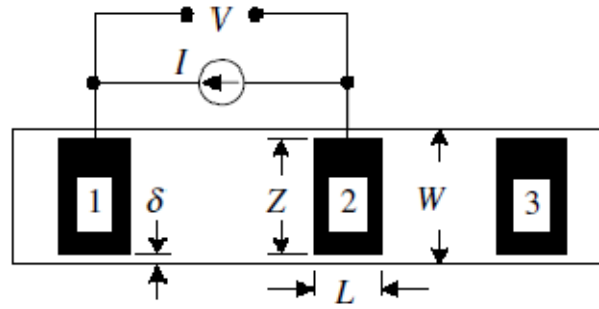


Figure 4.11: contact measurement configurations.

The expression R_{cf} is usually referred to simply as the contact resistance R_c . Two cases lead to simplifications of equation (4.14). For $L \leq 0.5 \cdot L_T$, $\coth(L/L_T) \sim L_T/L$ and then,

$$(4.15) \quad R_c \approx \frac{\rho_c}{LZ}$$

and for $L \geq 1.5 \cdot L_T$, $\coth(L/L_T) \sim 1$ and

$$(4.16) \quad R_c \approx \frac{\rho_c}{L_T Z}$$

The effective contact area is the actual contact area $A_c = L \cdot Z$ for the first case. But in the second case the effective contact area is $A_{c,eff} = L_T \cdot Z$.

Equation (4.14) is derived under the assumption that $\rho_c > 0.2 \cdot R_{sh} \cdot t^2$ (where t is the layer thickness). The TLM method must be modified if that conditions are not satisfied. Particularly, it is used a different structure with more than three contacts (Figure 4.12). The structure of Figure 4.12 is the one used in our experimental measurements.

For contacts with $L \geq 1.5 L_T$ and for a front contact resistance measurement of the structure in Figure 4.12, the total resistance between any two contacts is:

$$(4.17) \quad R_T = \frac{R_{sh} d}{Z} + 2R_c \approx \frac{R_{sh}}{Z} (d + 2L_T)$$

where:

$$(4.18) \quad R_c = \frac{\rho_c}{L_T Z} = \frac{L_T^2 R_{sh}}{L_T Z} = \frac{L_T R_{sh}}{Z}$$



Figure 4.12: TLM structure with more than two points.

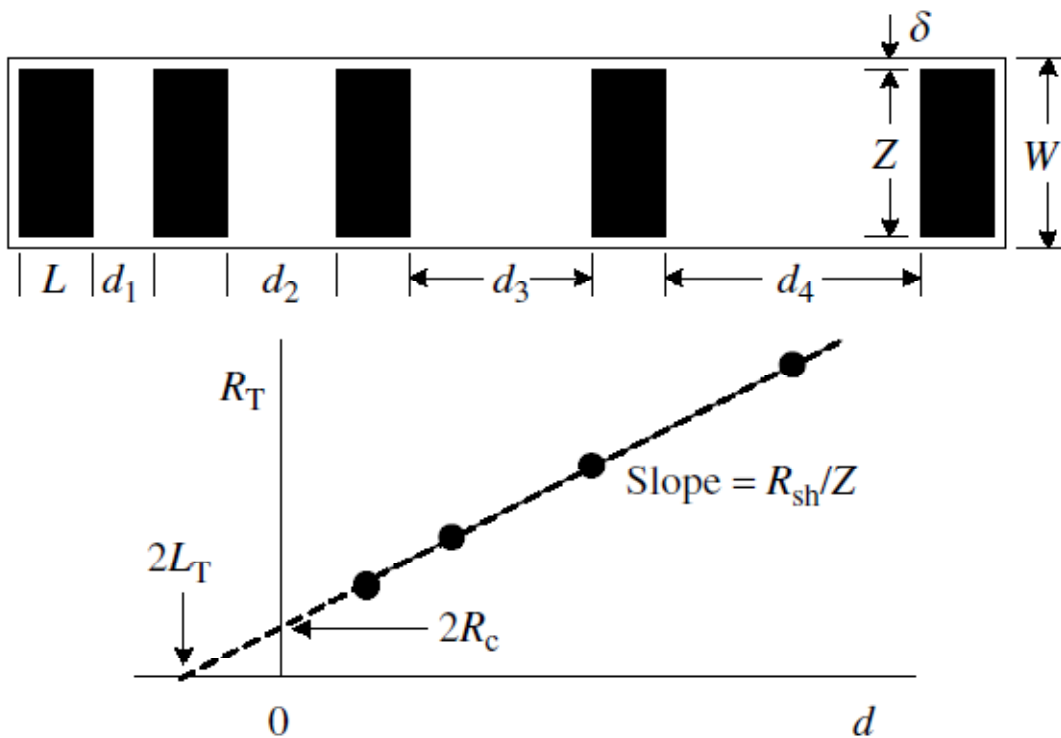


Figure 4.13: graph resulting by using the TLM structure with more than two points.

With this TLM structure, a resistance measurement is done for each ohmic contact distance d_i ; the values obtained are plotted in a $R_T - d$ graph, and the linear figure interpolating the points is drawn (Figure 4.13). Said line gives important information to us, in particular, as reported by equation (4.17), the slope (R_{sh}/Z) leads to the sheet resistance with the contact width Z independently measured. The intercept at $d=0$ is $R_T=2R_c$ giving the contact resistance. The intercept at $R_T = 0$ gives $-d=2L_T$ (if $L \geq 1.5 L_T$). Therefore, the transfer

length method gives a complete characterization of the contact by providing the sheet resistance, the contact resistance and the specific contact resistivity.

This method is commonly used, but it has its own problems. Among which, the most serious for our measurements, has been to assure a tight substrate. In fact, the TLM can be applied when the carrier distribution does not depend on the thickness (t) of the substrate upon which the ohmic contacts are realized and, particularly, said distribution cannot vary with the different distances d_i . This condition is never theoretically achievable because always the carrier distribution varies long the thickness direction, but practically, if the sample is tight enough, we can assume that the current is equal in each point of the t -axes (for each distances d_i). In other words, to apply the TLM, we have to make the ohmic contact on a layer of about $1\ \mu\text{m}$ or less (probably deposited on a thicker isolated substrate, acting just as structural support). This is possible when we are able to deposit tight layer of material used as substrate in the final process but, in our case, it was not possible. We had some GaAs wafer thick about $600\ \mu\text{m}$, and we wanted to characterize an ohmic contact fabricated on such a wafers. It was not possible for us to realize $1\ \mu\text{m}$ of perfectly equal material on a substrate acting as support.

In order to overcome the problem, a constant magnetic field has been applied to the sample during the measurement process, in direction perpendicular to the carrier flow and parallel to the sample surface. Said magnetic field acts generating a force going from the bottom side of the sample toward the upper one, hence, the carriers result to be confined in a tighter thickness of the substrate by reason of the generated force. This means that the carrier distribution will be almost completely equal along the t dimension, for each pair of points with different distance d_i (that corresponds to each point of the R_T - d curve).

To verify our measurement technique, we have carried out two different measurements on the same sample showed in Figure 4.14. As shown in Figure 4.15, that is a zoom of one of the four ohmic contacts of Figure 4.14, we can assume $Z=W=L=10^{-3}\ \text{m}$. The distance values are: $d_1=0.9609\ \text{mm}$, $d_2=1.3879\ \text{mm}$, $d_3=3.3630\ \text{mm}$, $d_4=52.3130\ \text{mm}$. The first measurement process has been done without magnetic field applied, the second one with a constant magnetic field applied in the condition described above.



Figure 4.14: Sample used in our experimental measurement for R_c determination.

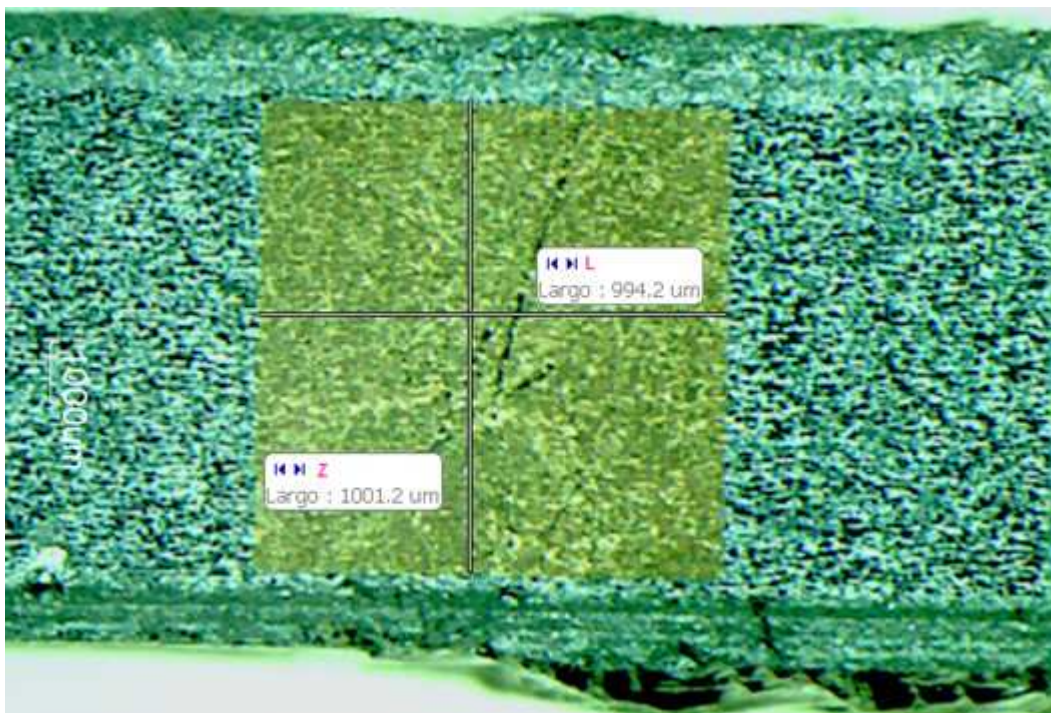


Figure 4.15: L and Z of a general ohmic contact of the sample used in our experimental measurement for R_c determination.

The results of the first measurement process are reported in Figure 4.16 (reporting also the equation of the interpolating linear curve). It is easy to understand as the plotted points of the graph cannot allow a reliable analysis, because the line interpolating the points is too distant from them. Actually, there is no liner curve intercepting the points, able to give us information from its equation. Moreover, according with the graph of figure 4.16, the R_T value for the distance d_1 is higher than the R_T value in correspondence to d_2 , and this result is senseless considering that for hither distances, the R_T value should be higher. We can explain this apparent senseless result, imagining that the carrier distribution between contacts 1 and 2 (distance d_1) is considerably different than the carrier distribution between contacts 2 and 3 (distance d_2). In particular, in the case of d_2 , the current flows through a greater portion of the total substrate thickness, so that the effect of the longer distance (that increase the resistance value) is overcome by the effect of the bigger portion of substrate thickness used (that decreases the resistance value).

As final consideration about the measurement reported above, we can assess that a graph similar to the one shown in Figure 4.13 is not obtained, and no analysis is possible on such graph.

The results of the measurement carried out with magnetic field applied are reported in Figure 4.17. The linearity of the plotted point is much more evident, and no ambiguous results are present. The distance of the points from the ideal condition (interpolating curve) is little enough to ascribe such error to the measurement process (observational error). As final consideration, we can state that the data obtained are suitable to be analyzed, comparing them with equation (4.17). In particular from the equation shown in Figure 4.17, we obtain:

$$R_T = \frac{R_{sh}d}{Z} + 2R_c = 1.21411 \cdot 10^3 d + 4.55781$$

Then, we can calculate the R_{sh} value as follows (considering $Z=10^{-3}$ m as reported in Figure 4.15):

$$\frac{R_{sh}}{Z} = 1.21411 \cdot 10^{-3} \rightarrow R_{sh} = 1.21411 \cdot 10^{-3} \cdot Z = 1.21411 \cdot 10^3 \cdot 10^{-3} = 1.21411 \Omega$$

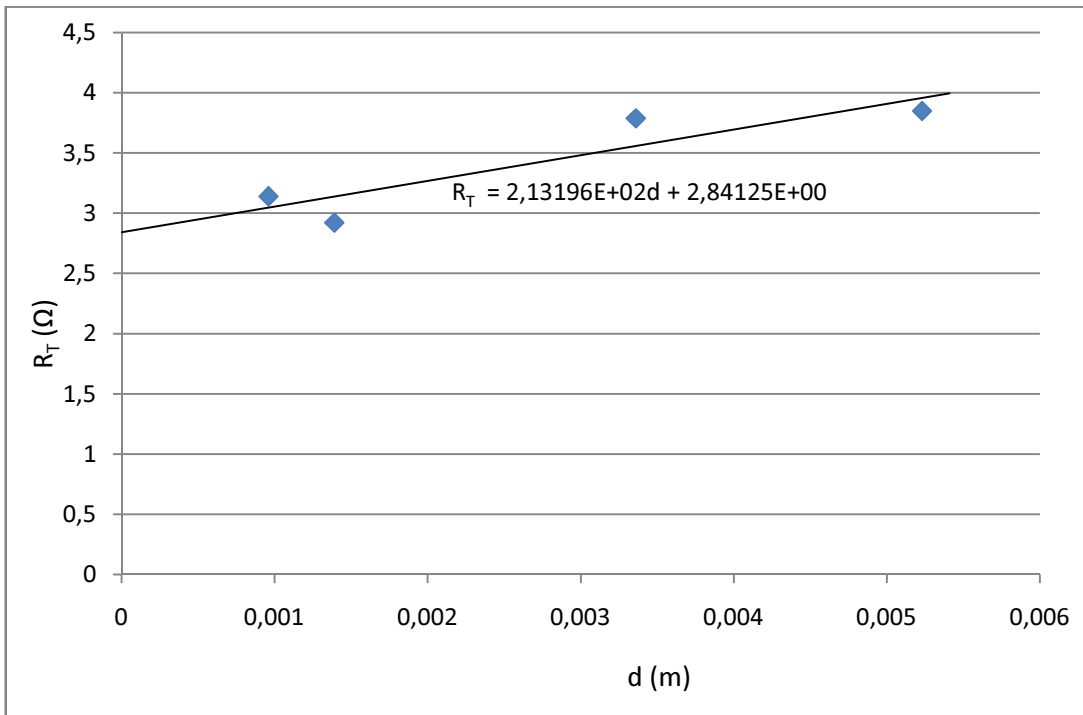


Figure 4.16: $R_T - d$ curve obtained with the standard TLM (more than two points).

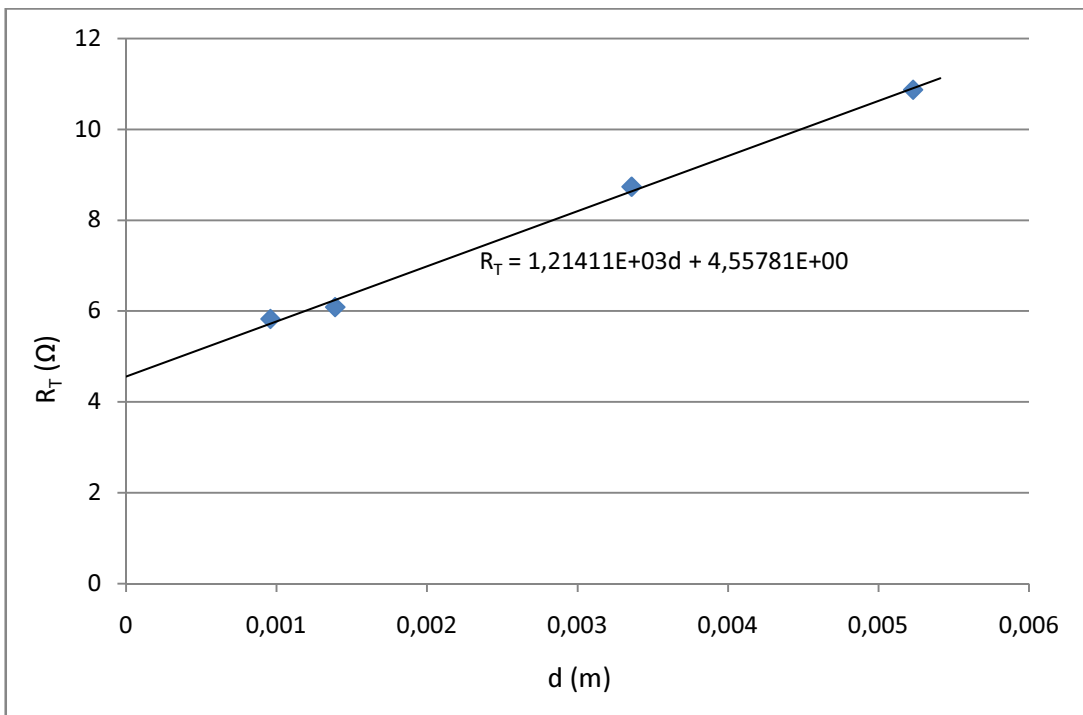


Figure 4.17: $R_T - d$ curve obtained with the TLM (more than two points) with magnetic field applied.

And also the R_c value:

$$2R_c = 4.55781 \rightarrow R_c = \frac{4.55781}{2} = 2.27891\Omega$$

Assuming the condition $L \geq 1.5 L_T$, and then valid the approximation of equation (4.17) we can write:

$$1.21411 \cdot 10^3 d + 4.55781 = 0 \rightarrow d = -2L_T = -\frac{4.55781}{1.21411 \cdot 10^3} \rightarrow L_T = 0,0019m$$

As we have actually obtained $L_T \sim 2 L$, we can use the equation (4.15) for calculating the ρ_c value:

$$\rho_c = R_c LZ = 2.27891 \cdot 10^{-3} \cdot 10^{-3} = 2.27891 \cdot 10^{-6} \Omega m^2$$

And the real L_T value is then calculated using the equation (4.13):

$$L_T = \sqrt{\rho_c / R_{sh}} = \sqrt{2.27891 \cdot 10^{-6} / 1.21411} = 1.37 \cdot 10^{-3} m$$

Therefore, with the proposed variation (application of a magnetic field to the sample under measurement process), we have been able to characterize our ohmic contact, calculating the most relevant parameters.

As we will see later, we have developed a room temperature process. In reality, this process uses the thermal annealing to make the ohmic contact, that is to provide high temperature values to the solar cell. To solve this problem, we have thought to substitute the thermal annealing with a laser treatment. Despite it is out of our scope to provide a wide study about the laser solution, we think is interesting to report the results of the first experiments carried out. One of the first problems of a laser treatment is that it provides a high power in a small area. This means that the Au-Zn layer can be performed by the laser, and then, the ohmic contact damaged. For example, it is clear as the spots present in Figure 4.18, resulting from a laser treatment, show the substrate material (GaAs) at the bottom of them, namely, the ohmic contact layers have been perforated. In this case the treatment conditions have been: pulsed, $f_{rate}=4KHz$, pulse intensity equal to 16 A, pulse width equal to 120 nm.

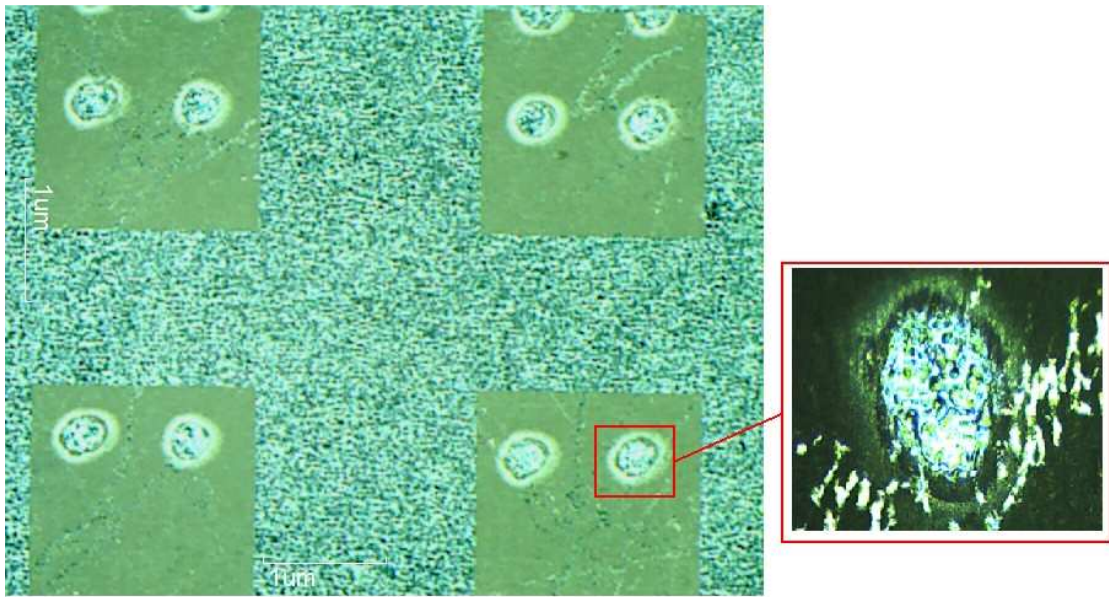


Figure 4.18: Ohmic contact after laser treatment with the following condition: pulsed, $f_{rate}=4KHz$, $I=16A$, pulse width=120nm.

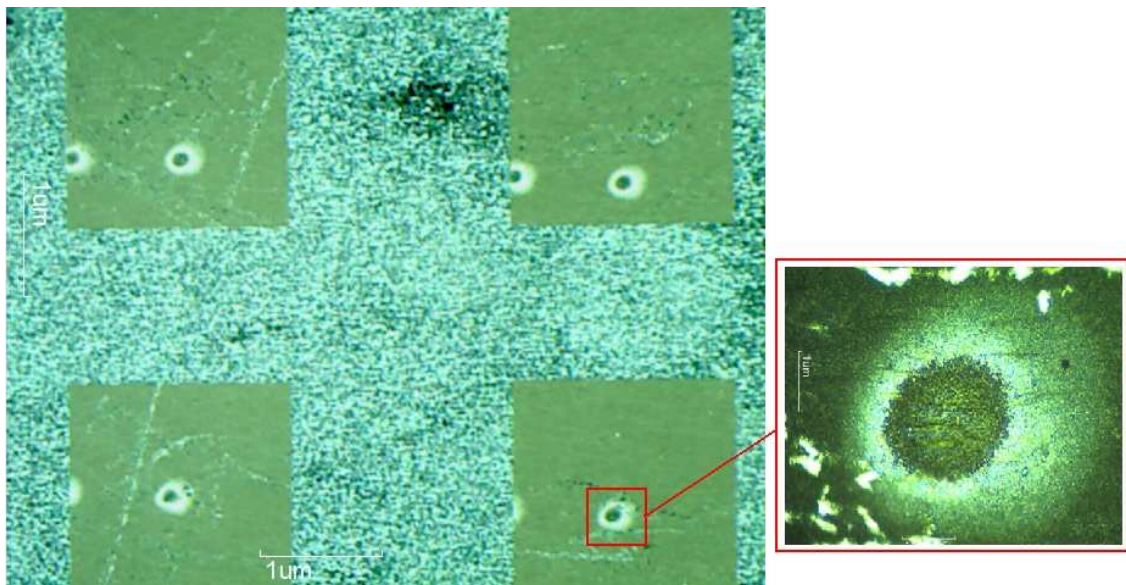


Figure 4.19: Ohmic contact after laser treatment with the following condition: pulsed, $f_{rate}=20KHz$, $I=16A$, pulse width=600nm.

To overcome the perforation problem, less energetic pulses have to be set. In particular in Figure 4.19 we can see the imagine of a sample treated with the following condition: pulsed, $f_{rate}=20$ KHz, pulse intensity equal to 16 A, pulse width equal to 600 nm. Under this condition no hole is caused by the laser. In this case, the higher pulse width is the cause of the fall of the pulse energy.

Certainly less energetic pulse generate a more resistive ohmic contact, so that a compromise has to be find about the energy pulse to obtain the right laser configuration giving the lowest ohmic resistance without perforating the Zn-Au layers.

4.5 Cleaning and passivation

The wafer cleaning is of crucial importance in order to obtain a “good” solar cell. In this view a lot of papers and scientific documentations, have been examined to determinate some chemical cleaning candidate to be used in our process. In paper [15] has been examined the potential distribution on the surface of n-GaAs wafers, subjected to various types of chemical treatments. It reports that, the use of concentrated hydrochloric acid in solutions of ethanol and isopropanol with $pH < -1$ leads to the formation of amorphous arsenic on the GaAs surface. Afterwards, the arsenic layer can be removed by heating the sample in ultrahigh vacuum at $T \leq 400^\circ C$, in order to obtain a clean surface. In particular in [15], two different treatments are proposed but, before to see the phases involved in them, we have to underline as the cleaning processes (we will mention hereinafter) always implicate two main steps: surface degreasing (for removing contaminants such as metal ions or organic compounds) and surface passivation. The problem of passivation involves the removal of the layer of native oxide and the formation of a thin protective layer on the semiconductor surface to prevent surface oxidation in the atmosphere. The ideal GaAs surface is supposed to be free of surface states within the bandgap, but this is not the case of real devices. The scope of the passivation process is to minimize the formation of energy states between the valence band and the conduction band that occurs at the surface [25]. This problem is not particularly important for Si-devices, because the native oxide of Si (SiO_2), unlike the one of GaAs, leads to the formation of an extremely low density of

interface states. In this view, for GaAs wafers, it is important to replace the native oxide with an alternative layer on the surface because the formation of the native oxide itself can generate defects that badly affect the electronic behavior.

The first treatment (or itinerary) of [15] involves the following steps: preliminary chemical cleaning (mainly for degreasing) via sequential treatments in monoethanolamine (C_2H_7ON), dimethylformamide (C_3H_7ON), and isopropanol (C_3H_7OH); subsequently, in order to remove the native oxide, has been used a solution of $H_2SO_4 : H_2O = 1 : 10$ ($pH=-0.5$) where the sample has been soaked for a time of 10 seconds; after, a protective silicon oxide (SiO_2) layer 100 nm thick has been deposited plasmochemically (by decomposition of monosilane) at $T=280\text{ }^\circ C$; the following step was the realization of the ohmic contact on the substrate (that is the final aim for which the cleaning process is carried out); eventually, traces of deposition of SiO_2 have been removed in a 5% HF solution in the etchant $H_2SO_4 : H_2O_2 : H_2O = 3 : 1 : 1$. The second itinerary [15] differs from the first one only in the finishing treatment of the surface, where ammonia was used instead of counteretch. In particular, this second itinerary involves a treatment with aqueous solution of NH_4OH ($pH=12$, concentration=25%) followed by a washing in isopropanol. The first itinerary registered a high degree of non uniformity on the surface, however the second one gives better results. Particularly, the absolute value of the surface potential is about 0.2 V lower than the case of the first itinerary, and its roughness decreases even more (more than an order of magnitude). Overall, an important data reported in the paper, is that the distribution of the profile and phase contrast over the area is close to the ideal Gaussian distribution.

Also in [16] is reported a surface preparation process using an ammonium hydroxide (NH_4OH) to remove the native oxide present on the GaAs. The paper proposes four different itineraries, each one having the same degreasing process (involving the use of acetone, methanol, and isopropanol), and differing in the second step, namely, in the passivation process. The first treatment use NH_4OH solution (29%) in which the sample is soaked for 3 minutes to remove the native oxide. This phase is followed by a drying process using a N_2 blowgun. The NH_4OH etching step removes arsenic and gallium oxides from the surface and said surface becomes covered by elemental arsenic and a tiny amount of

gallium suboxide. In this way, the GaAs surface becomes hydroxylated and ready for the ALD (atomic layer deposited) of high-K dielectric. The ALD process results in the disappearance of elemental arsenic and a self cleaning of the GaAs surface. The second treatment uses a HCl : H₂O = 1 : 1 solution (in which the sample is soaked for 1 minute) to remove the native oxide. Afterwards the sample is dipped in (NH₄)₂S solution for 10 minutes at room temperature and, finally, dried using an N₂ blowgun. The third itinerary is the “HF treatment”. It is carried out by soaking the sample in diluted 1% HF solution for 1 minute, cleaning it with deionized water and finally drying the sample using N₂ blowgun. In the fourth treatment the sample is dipped in a HCl : H₂O = 1 : 1 solution for 1 minute, subsequently, in deionized water and finally is dried with a N₂ blowgun. The final step consists in loading the samples into an ASM F-120 ALD system (this is done for all the samples of each treatment).

Another work [17] describes the use of acetone in the degreasing process (in which the sample is dipped for 5 minutes), ethanol (in which the sample is dipped for other 5 minutes) and deionised water (other 5 minutes). The degreasing process is capable to remove a layer of oxides 1.7 nm thick, as measured by ellipsometry. Like in paper [16] said degreasing is followed by an etching in (NH₄)₂S_x solution (for 30 minutes at T=40 °C). Hence, the samples were rinsed for 10 seconds using deionized water. Unlike the [16], in this case The (NH₄)₂S_x passivation has been additionally improved using alcohol solution of the ammonia sulfide. The results from a potential distribution analysis show that, the band bending and depletion layer decreases upon subsequent steps of treatment. In a single run procedure (giving the best results in term of band bending reduction) the substrates were wet during all the process, and they have been blown with dry nitrogen only once before the measurement.

In [23] is used a solution of (NH₄)₂S in *i*-C₃H₇OH for the surface passivation of GaAs wafers. According to the paper, the sample has been dipped for 1-120 seconds (has been found that the optimal treatment time is for approximately 1 minute) at room temperature with illumination (using a 200-W incandescent lamp) and, as final step, the samples were air-dried. Different ratios of the volume concentrations of (NH₄)₂S : (*i*-C₃H₇OH) were used: 1 : 0 (pure (NH₄)₂S solution), 1 : 10, 1 : 50, and 1 : 100. A reduction in leakage current has

benne registered for both pure $(\text{NH}_4)_2\text{S}$ and $(\text{NH}_4)_2\text{S}$ solutions (in isopropyl alcohol) treatments, however the greatest reduction in the leakage currents has been obtained in a $(\text{NH}_4)_2\text{S} : i\text{-C}_3\text{H}_7\text{OH}$ with volume concentrations 1:10.

In [18] S. Arabasz reports the results of systematic XPS (X-ray Photoelectron Spectroscopy) studies of wet sulfided epi-ready samples. The passivation process is similar to the one used in processes [16] and [17] (realized by dipping for 30 minutes the samples in $(\text{NH}_4)_2\text{S}_x$ solution both at room temperature and at $T=40\text{ }^\circ\text{C}$). But in this case, some samples additionally were subjected to UHV flash annealing at $400\text{ }^\circ\text{C}$, followed by a second subsequent flash at 500°C . The paper gives information about the preparation of the $(\text{NH}_4)_2\text{S}_x$ solution: it was prepared adding slowly, 1.25 ml of 37% HNO_3 solution into 10 ml of 20% $(\text{NH}_4)_2\text{S}$ solution in the nitrogen atmosphere, and finally completed by 100 ml of deionized water. The results of [18] show a dependence of the sulfidation mechanism on the $(\text{NH}_4)_2\text{S}_x$ solution temperature: better results were obtained for solution at $40\text{ }^\circ\text{C}$ than at room temperature. The UHV flash annealing seems to be useful, in fact, the authors claim that the residual contaminants are removed using this treatment. Particularly, the amount of As-S bondings is significantly reduced, whereas Ga-S bondings (that are more stable) remain unchanged.

V.L. Alperovich in [19] proposes a surface passivation of GaAs substrates using a HCl-isopropanol solution. In the context of these studies is important to state that has been shown as the properties of the GaAs surface, treated in aqueous HCl solutions, critically depended on the HCl concentration. In the process, GaAs (crystal orientation: 100) samples were etched in $\text{H}_2\text{SO}_4 : \text{H}_2\text{O}_2 : \text{H}_2\text{O} = 20 : 1 : 1$ for 1 minute at $40\text{ }^\circ\text{C}$ and then treated in 20% solution of HCl-iPA for 3 minutes at $18\text{ }^\circ\text{C}$. The HCl-iPA solution was prepared with 100 ml of high-purity doubly distilled iPA put in a 3 liters desiccator filled with 300 ml of hydrochloric acid (concentrated 37%). Surface treated in the solutions of HCl in isopropyl alcohol are studied by XPS (X-ray photoelectron spectroscopy), LEED (Low-energy electron diffraction) and AFM (Atomic force microscope), and the results coming out from these analysis prove the fact that an accumulation of amorphous arsenic on the GaAs surface occurs under the HCl-iPA treatment. Said treatment leads to the formation of

As-stabilized layers on the GaAs surface, therefore has been obtained a chemical passivation of the surface by submonolayer of excess arsenic.

In [24] has been studied the composition, stoichiometry, and atomic structure of GaAs surface after treatment in HCl-isopropanol solution. As important statement, the paper reports that native oxides and carbon contaminations can be removed from the GaAs surface using a solution of HCl : ethanol under nitrogen atmosphere. Has been carried out a x-ray photoelectron spectroscopy (XPS) analysis showing that, a thin layer of elemental As^o remains on the surface after the HCl : ethanol treatment. An additional annealing of GaAs at 350 °C in ultrahigh vacuum (UHV) removed the excess arsenic. Despite some researchers observed the presence of carbon layer on the GaAs surface treated in HCl-alcohol or HCl deoxidized water, this carbon contamination is easily removed from the surface by annealing step.

Jun-Kyu Yang in [20] proposes a Gd₂O₃/GaAs interface improvement by sulfur passivation. The cleaning process is almost the same of the second treatment of [16]: degreasing has been carried out by immersing the sample in boiling acetone for 10 minutes, afterwards in methanol for 5 minutes, and eventually in deionized water for 1 minute; in order to remove the surface oxides of the substrate has been used a HCl solution (3 minutes of dipping) and finally the cleaned sample of GaAs were passivated by immersing them in the (NH₄)₂S solution for 10 minutes (so, in this case, HCl and (NH₄)₂S has been used together in the same process). As final step, Gd₂O₃ films were deposited on the GaAs substrates by evaporation from a polycrystalline source under a pressure of 2·10⁻⁷ Torr at room temperature. In the paper it is shown that the sulfur passivation causes a decrease of the interface-state density and, consequently an improvement of the C-V characteristics of the junction.

In [21], Konenkova quotes about the modification of GaAs surfaces by treatment in alcoholic sulfide solutions. According to the cleaning and passivation process used in the paper, prior to sulfur treatment, the wafer was etched in HCl for 100 seconds at room temperature. Hence, Sulfide treatment was carried out in different solutions (reported later) with simultaneous illumination (using a 200 W incandescent lamp). The used solutions are: pure ammonium sulfide (NH₄)₂S (20%) in water; saturated solution of sodium

sulfide $\text{Na}_2\text{S}_x : \text{H}_2\text{O}$; solutions of ammonium sulfide $(\text{NH}_4)_2\text{S}$ (20%) in isopropanol ($i\text{-C}_3\text{H}_7\text{OH}$) and tert-butanol ($t\text{-C}_4\text{H}_9\text{OH}$) with 10% (percent by volume); supersaturated solutions of sodium sulfide $\text{Na}_2\text{S}_x : \text{H}_2\text{O}$ in isopropanol and tert-butanol. The residual solution was removed from sample after finishing the surface treatment by spinning at 1000 rpm. The results show that, the best case (among the treatment using different solutions) was the one involving sodium sulfide solutions and, subsequently, ammonium sulfide solutions (ammonium sulfide in isopropanol with a concentration ratio of 1 : 10).

In paper [22] is presented another passivation method for GaAs surfaces. According to it, an initial degreasing process has been carried out, using CCl_4 and boiling toluene (as alternative to the CCl_4). Hence, the sample was polished chemically in an $\text{H}_2\text{SO}_4 : \text{H}_2\text{O}_2 : \text{H}_2\text{O}$ solution (3 : 1 : 1) at 50-60 °C for 3 minutes. Some samples, before the degreasing process, were also polished chemomechanically with an NaClO solution. After said steps, the GaAs substrates were treated in known acidic and alkaline etchants containing H_2O_2 or aqueous NaClO (that are used as an oxidizer); finally, the samples were soaked in deionized or bidistilled water or isopropanol and dried with N_2 flow. As final consideration, the authors claim that has been proved the possibility to passivate the GaAs surface with elemental arsenic via selective dissolution in highly acidic ($\text{pH} < -0.3$) or alkaline ($\text{pH} > 11$) solutions.

Baca and Ashby [25] give a broad description of the cleaning and passivation problem of GaAs surface. It tackles the two different aspects explaining what processes can meet some specific problems. It divides the cleaning problem, in three main aims: removal of organic contaminations, removal of metal contaminations, removal of the native oxide, passivation. In order to remove organic contaminants, it suggests to use the following process, involving the use of different organic solvents: boil the sample for 10 minutes in 1 : 1 : 1-trichloroethane (TCE); boil for other 10 minutes in acetone; dip in methanol for 10 minutes; and finally soak in isopropanol for 10 minutes. Ultrasound can also be used as an alternative to boiling. In order to remove the native oxide, [25] suggests to heat the sample up to around 600-700 °C, for about 15 minutes, under gas flow (such as AsH_3). The removal of metal ions can be achieved by using ammonium hydroxide solutions such as NH_4OH (obtained mixing NH_3 to water). A concentration from 1 : 20 to 1 : 10 of $\text{NH}_4\text{OH} : \text{H}_2\text{O}$ has also the function of remove the native oxide on the surface. In [25] is reported that,

although acidic clearing solutions can be used, such as HCl and H₃PO₄, they tend to leave the surface with As element predominance on it and, if the cleaning process is carried out in a nitrogen atmosphere, the As remains unoxidised. This is not a good result considering that a surface excess of As can be highly undesirable from an electronic perspective. On the other hand, NH₄OH solutions preserve the stoichiometry of the surface (leaving almost an equal quantity of As and Ga elements). Alternatively, if HCl is diluted with ethanol instead of deionized water the results are better in terms of element concentration, and are really close to the ones obtained using NH₄OH in water. Concerning the native oxide, it is important to state as, after its removal, it will start to growth another time on the GaAs surface, therefore some unwanted reoxidation is inevitable.

Obviously, other solution for GaAs passivation are available in the scientific literature, but we have focused just in the treatment involving (NH₄)₂S and few more compounds. This was for focusing our research in a well determined path, that however seems to be one of the most accredited together with passivation method using S₂Cl₂.

We did not prove all the cleaning process reported above, but it is clear that, most of the times they have common points. In this view, our scope was to extrapolate from the information given in the related papers, the treatment better meeting our needs, and more suitable for our sources. The cleaning treatment effectively used in the fabrication, are reported in the sections related to the different process we have carried out.

4.6 Process P1

4.6.1 Process description

After the stage involving the development of each specific stage of the solar cell making process, we made the first processes as base for further developments.

The first complete process of fabrication we made is what we will call hereinafter simply P1. The process steps showed in Figure 4.20, are the following: GaAs substrate cleaning (10 minutes of Acetone with ultrasound, 10 minutes of Isopropanol with ultrasound, sample rinse in DI water, sample soaking in a solution of HF (5%) in water for

30 seconds); Zn-Au deposition and thermal annealing (ohmic contact); -Deposition of ITO on p-GaAs wafer; -photoresist deposition on the ITO coating; -lithography 1, to define the ITO coating in a square, avoiding that it could reach the back of the substrate creating a short circuit with the ohmic contact layers; -ITO etching; -lithography 2, to make the fingers on the ITO layer; Au deposition for the front contacts (fingers); -photoresist removal.

The ohmic contact fabrication made before the ITO deposition, can let the dust settle on the GaAs substrate, and it should be a problem for the ITO-GaAs interface quality, but we cannot make the ITO deposition before the ohmic contact fabrication, because the thermal annealing (reaching 450°C) certainly will affect the quality of the ITO covering damaging it.

Depositions of both ITO and Au-Zn layers have been carried out with the sputtering equipment quoted in the previous sections. The deposition of the Zn covering has been made with the following conditions: pressure equal to $5 \cdot 10^{-3}$ mbar; Ar flux equal to 10 sccm; RF input power equal to 50 W; T_D (deposition time) = 1 minute. The Au deposition has been done with the same equipment (without opening the sputtering camera) and with the following conditions: pressure equal to $5 \cdot 10^{-3}$ mbar; Ar flux equal to 10 sccm; RF input power equal to 50 W; $T_D=10$ minutes. Before the Zn deposition an inverse sputtering has been carried out (to clean the GaAs surface) for 5 minutes, with pressure = $8 \cdot 10^{-3}$ mbar, Ar flux = 10 sccm and RF input power = 50W. The ITO covering has been deposited as follows: pressure equal to $4 \cdot 10^{-3}$ mbar; Ar flux equal to 10 sccm; RF input power equal to 20 W; $T_D= 15$ minutes. The deposition conditions for the front contact (fingers) have been: pressure equal to $5 \cdot 10^{-3}$ mbar; Ar flux equal to 10 sccm; RF input power equal to 100W; $T_D=20$ minutes.

The size of the solar cell made with process P1 is 1cm X 1cm, therefore the area (A) is equal to 10^{-4} m.

The GaAs substrate is p-doped (with Zn doping agent), with concentration equal to 10^6 cm^{-3} .

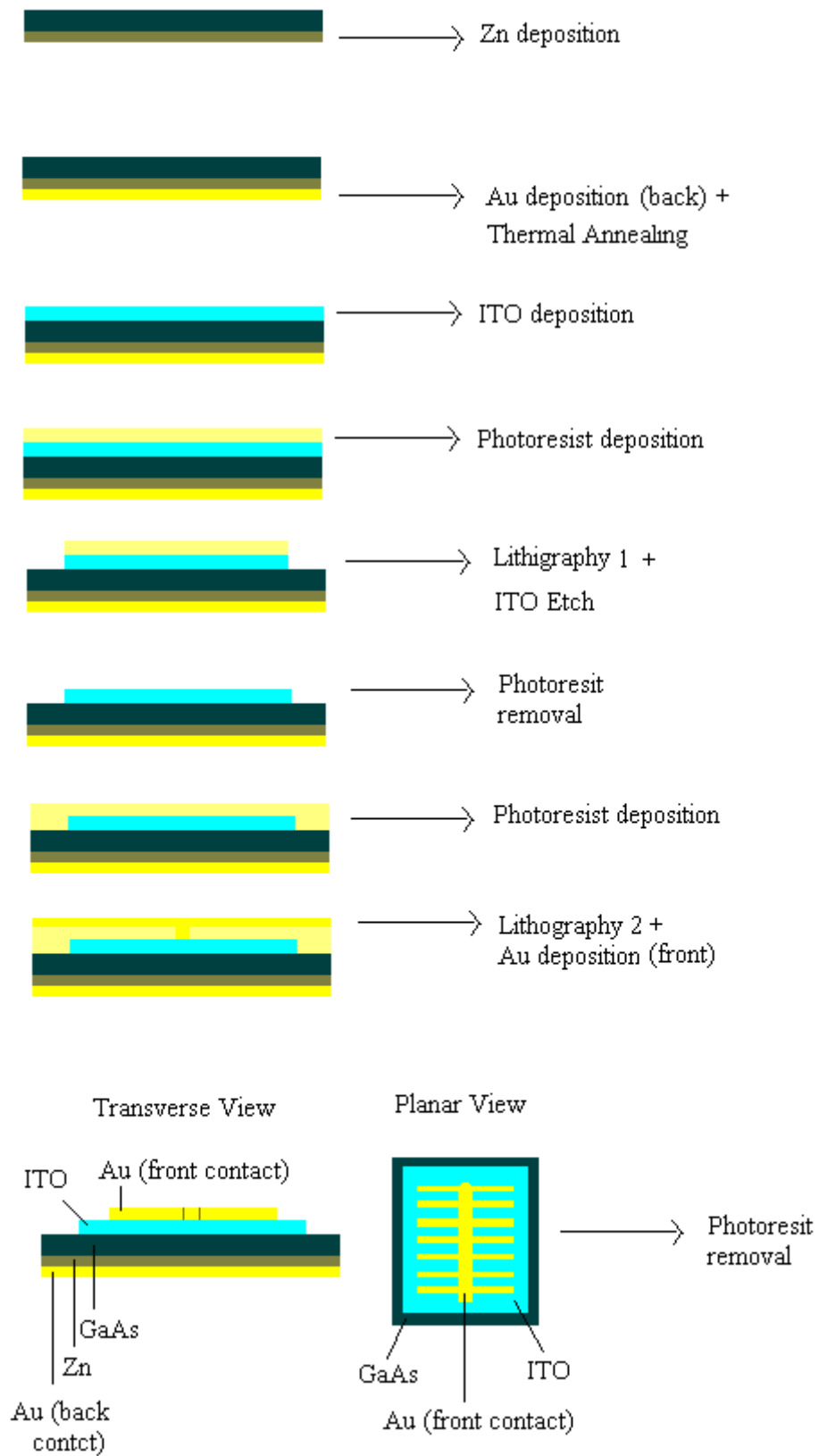


Figure 4.20: Process P1.

4.6.2 I-V Characteristic of P1 cell

The I-V characteristic of the solar cell of P1 (hereinafter P1 cell, for sake of simplicity), is reported in Figure 4.21. The most important point coming out from the graph is that the fabricated P1 cell actually works as a solar cell. In fact, a negative current is generated, together with a positive voltage, when it is illuminated. The I_{SC} value is considerable low, but the V_{OC} value is probably the most relevant problem together with the FF value. Moreover, from the I-V curve, we can see that the shunt resistance (R_{sh}) is probably too low and the low R_{sh} value affect badly also the V_{OC} .

Analyzing the characteristic of Figure 4.21 we can extract the value reported in Figure 4.22. In particular, we can see that $P_{max} = 4,76 \cdot 10^{-5}$ W, which is for $I_m = 1,35 \cdot 10^{-3}$ A and $V_m = 3,52 \cdot 10^{-2}$ V. Moreover, from the same graph come out that $I_{SC} = 2,76 \cdot 10^{-3}$ A and $V_{OC} = 6,83 \cdot 10^{-2}$ V. So that we can calculate the FF value using equation (2.82):

$$FF = \frac{V_m I_m}{V_{OC} I_{SC}} = \frac{3,52 \cdot 10^{-2} \cdot 1,35 \cdot 10^{-3}}{6,83 \cdot 10^{-2} \cdot 2,76 \cdot 10^{-3}} = 0,25$$

That is quite low, as we expected seeing the figure of the graph. Now we can also calculate the efficiency (η) from equation (2.64):

$$\eta = \frac{P_{max}}{P_{in}} = \frac{I_m V_m}{AG} = \frac{4,76 \cdot 10^{-5}}{0,0001 \cdot 1000} = 4,76 \cdot 10^{-4}$$

With $G=1000$ W/m² and $A=10^{-4}$ m.

The characteristic of Figure 4.21 seems to show the low quality of the interface ITO GaAs. The recombination effect is notable and it brings the V_{OC} to a quite low value (0.0067 V). There is the possibility that the linear trend of the P1 cell characteristic is due to the series resistance, but if we consider as main R_s component the ohmic contact (that is a good approximation), we can note that for an area of 1 mm² (10^{-6} m²) we have calculated in section 4.4.2 an $R_C = 2.28 \Omega$, hence for P1 cell, having $A=10^{-4}$ m², we obtain:

$$R_s \approx R_C = \frac{2.28 \cdot 10^{-6}}{10^{-4}} = 0,028 \Omega$$

That is not a value so high to determine the quasi linear trend of Figure 4.21.

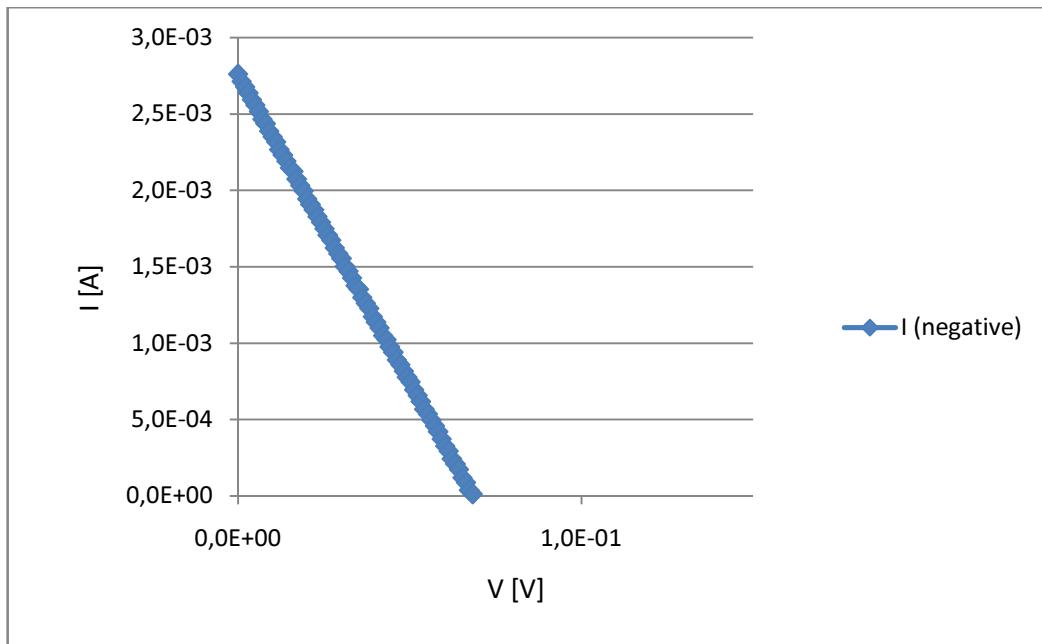


Figure 4.21: I-V characteristic of P1 cell in light conditions.

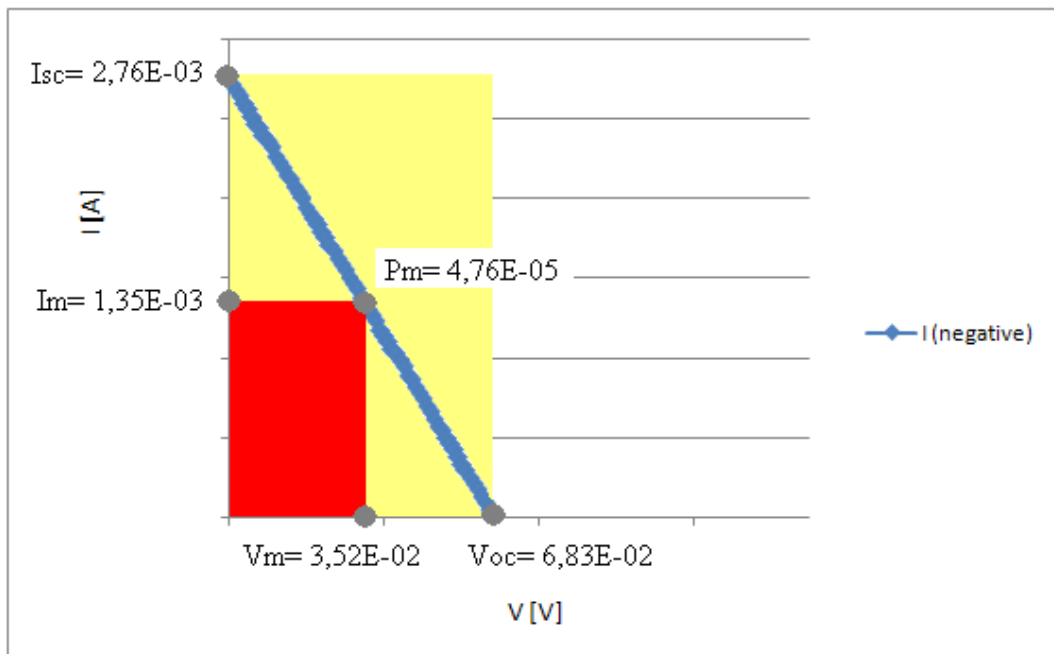


Figure 4.22: I-V characteristic and main parameters of P1 cell.

Therefore we infer that said trend is caused by the low R_{sh} value, due mainly to junction defects and border effects. The low R_{sh} cause both a decrease of the current for an increasing voltage and a lower V_{OC} . This is because, from Figure 2.24 (PSpice equivalent circuit for a solar cell), if R_{sh} is low enough, we have:

$$(4.19) \quad I = I_{sc} - \frac{V}{R_{sh}}$$

And then, from equation 4.19 and from the linear trend interpolating the characteristic of P1 cell (Figure 4.23), we can calculate the R_{sh} value:

$$I = I_{sc} - \frac{V}{R_{sh}} = 2,79757267 \cdot 10^{-3} - 4,1150842610^{-2} \cdot V$$

So that:

$$R_{sh} = \frac{1}{4,11508426 \cdot 10^{-2}} = 24,3 \Omega$$

That is a value too low for R_{sh} . Clearly the calculated R_{sh} value is an approximation of the real one, because we have considered R_s negligible, but actually it should be considered for a more precise calculation.

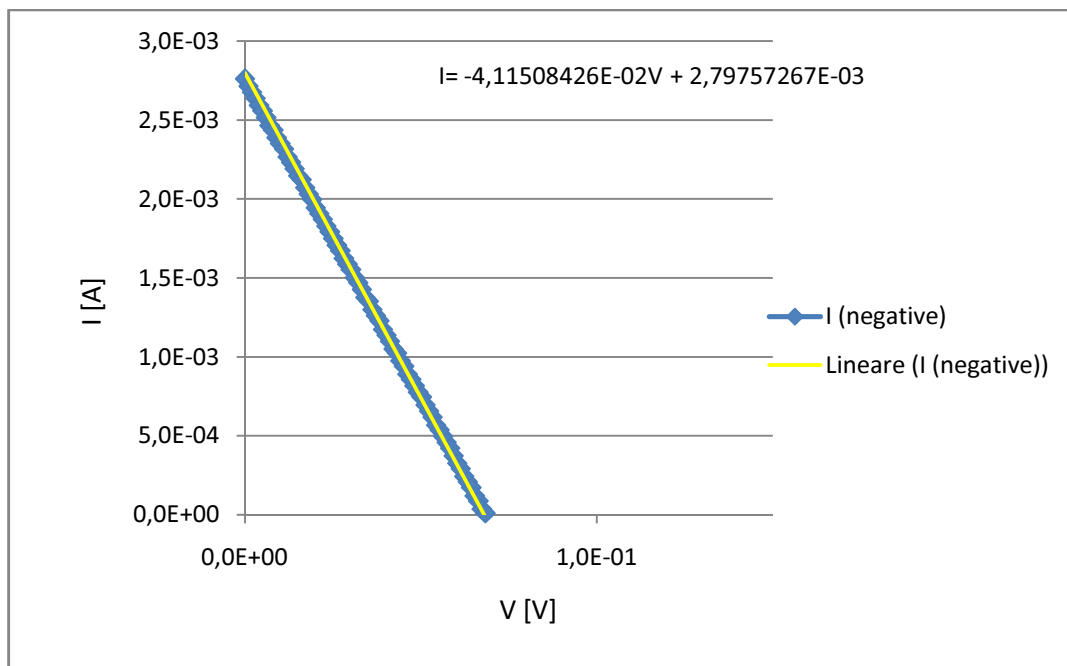


Figure 4.23: I-V characteristic of P1 cell with linear interpolation.

4.7 Process P2

4.7.1 Process variations

The second process we carried out (P2) have important differences relative to the ITO. In fact, in the first process, it has suffered high temperature because of the two lithography processes.

The most important variation in this second process P2, is the use of shadow masks. In the first process, we carried out a lithography on the ITO layer to define the ITO area and to make the fingers. In this way, the ITO quality could be badly affected. Hence, in order to prevent the sample from suffering this thermal stress, we use shadow masks. They are made of metal material, conveniently shaped, and in the solar cell making process, are put on the GaAs surface to deposit ITO before and Au (to make the finger) later. In this way the ITO and Au materials will be deposited only within the open windows of the shadow masks (having the shape of a square in the first case, and of fingers in the second one). At the end of the depositions, the fingers are present on a square of ITO on a GaAs substrate; all without making any photolithography step. The deposition process is shown in Figure 4.24.

The depositions of both ITO and Au-Zn layers have been carried out with the sputtering equipment quoted in the previous sections. The deposition of the Zn covering has been made with the same conditions of process P1. Also for P2 an inverse sputtering is carried out at the same condition of process P1. The ITO covering has been deposited as follows: pressure equal to $4 \cdot 10^{-3}$ mbar; Ar flux equal to 10 sccm; RF input power equal to 16W; $T_D=25$ minutes. The deposition conditions for the front contact (fingers) have been: pressure equal to $5 \cdot 10^{-3}$ mbar; Ar flux equal to 10 sccm; RF input power equal to 50W; $T_D=30$ minutes.

The size of the solar cell P2 is 5mm X 5mm, therefore $A=25 \cdot 10^{-6}$ m.

The main changes have been about the front contact and the ITO power depositions: both have been decreased in order to ensure no damage to the sample. This choice involves the increase of the deposition time to obtain the same thickness for both fingers and ITO covering, for this reason such times have been raised too.

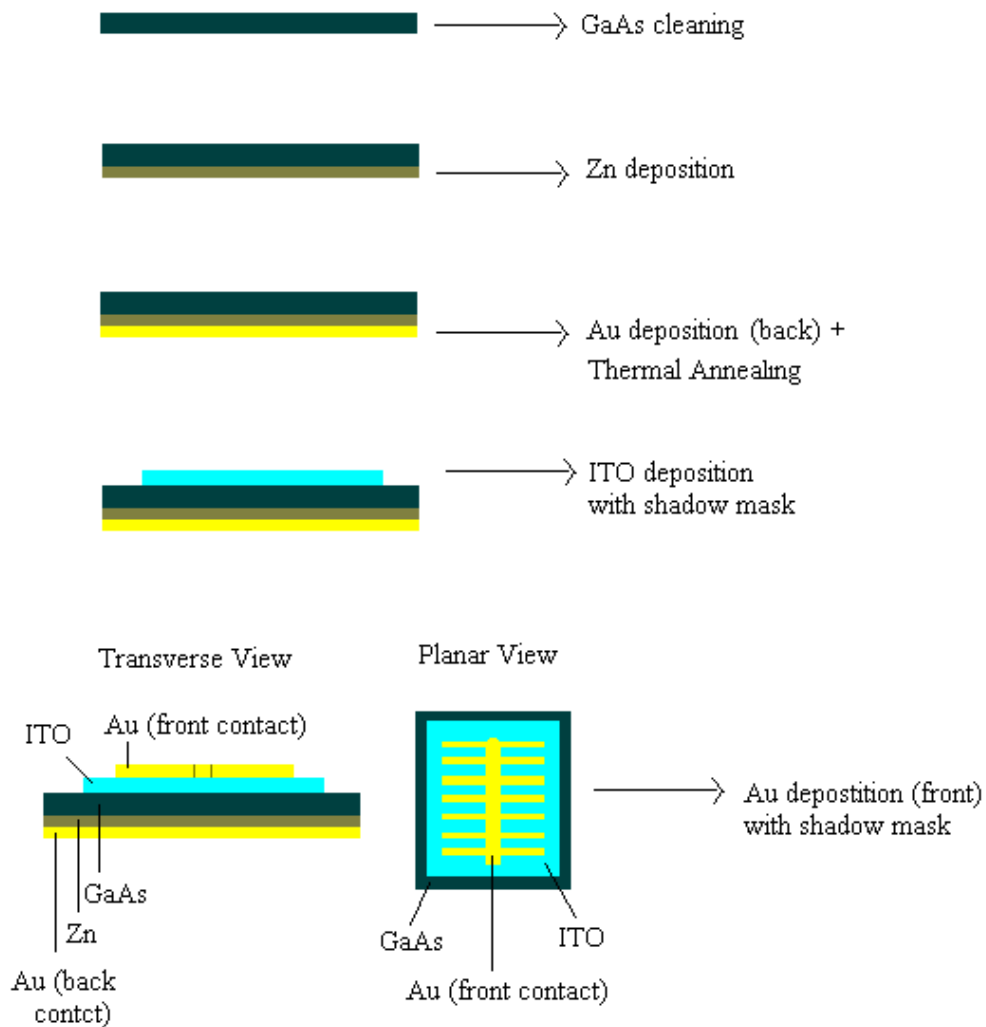


Figure 4.24: Process P2.

It is probably interesting to describe the process with which the shadow masks have been made (Figure 4.25). Said process has been carried out as follows: -glass substrate cleaning; -photoresist deposition (lithography 1); - Cu deposition with thermal evaporator (described in section 3 and represented in Figure 3.8); -lithography 2, to define same areas where Cu have to be etched; -Cu etching; -lithography 3, that is the Cu cleaning (removal of the photoresist presents on Cu surfaces); -Epitaxial growth of Nickel; -Photoresist and glass substrate removal.

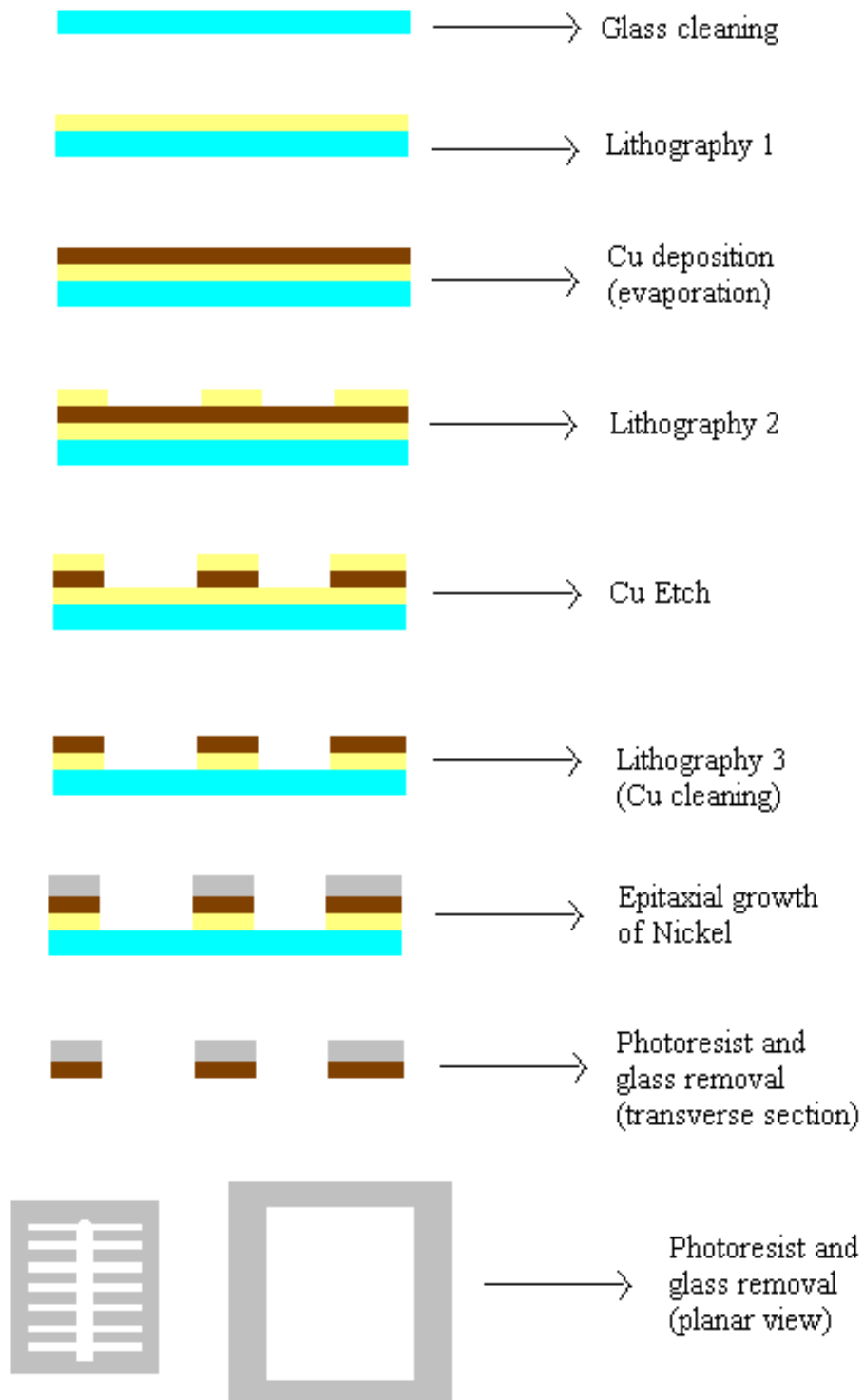


Figure 4.25: Shadow masks making process.

4.7.2 I-V Characteristic of P2 cell

The I-V characteristic of the solar cell of P2 (P2 cell), is reported in Figure 4.26. The characteristic is much better than the one of P1 cell.

From Figure 4.27, as done for P1 cell, we extract the main parameters to calculate FF and efficiency. Particularly, we can see that $P_{\max} = 9,86 \cdot 10^{-5}$ W, that is for $I_m = 1,31 \cdot 10^{-3}$ A and $V_m = 7,53 \cdot 10^{-2}$ V. Moreover, from the same graph come out that $I_{SC} = 1,84 \cdot 10^{-3}$ A and $V_{OC} = 1,15 \cdot 10^{-1}$ V. So that we can calculate the FF value using equation (2.82):

$$FF = \frac{V_m I_m}{V_{OC} I_{SC}} = \frac{7,53 \cdot 10^{-2} \cdot 1,31 \cdot 10^{-3}}{1,15 \cdot 10^{-1} \cdot 1,84 \cdot 10^{-3}} = 0,47$$

Now we can calculate the efficiency (η) from equation (2.64):

$$\eta = \frac{P_{\max}}{P_{in}} = \frac{I_m V_m}{AG} = \frac{9,86 \cdot 10^{-5}}{0,005 \cdot 0,005 \cdot 1000} = 3,94 \cdot 10^{-3}$$

With $G = 1000$ W/m² and $A = 25 \cdot 10^{-6}$ m.

Overall, the parameters for P2 cell are considerably better than the ones of P1 cell. The Voc value is almost doubled, as well as the FF. The efficiency, despite remaining quite low, is dramatically increased for the cell of process P2 (of about one order of magnitude), reaching the value of $3,94 \cdot 10^{-3}$ that is about 0.4%. To compare the current we have to consider the current density, because for P1 cell $A = 10^{-4}$ m and for P2 cell $A = 25 \cdot 10^{-6}$ m. So that we can calculate J_{SCP1} , J_{mP1} , J_{SCP2} , J_{mP2} as follows:

$$J_{sc_{P1}} = \frac{I_{sc_{P1}}}{A_{P1}} = \frac{2,76 \cdot 10^{-3}}{10^{-4}} = 2,76 \frac{mA}{cm^2}$$

$$J_{m_{P1}} = \frac{I_{m_{P1}}}{A_{P1}} = \frac{1,35 \cdot 10^{-3}}{10^{-4}} = 1,35 \frac{mA}{cm^2}$$

$$J_{sc_{P2}} = \frac{I_{sc_{P2}}}{A_{P2}} = \frac{1,84 \cdot 10^{-3}}{25 \cdot 10^{-6}} = 7,36 \frac{mA}{cm^2}$$

$$J_{m_{P2}} = \frac{I_{m_{P2}}}{A_{P2}} = \frac{1,31 \cdot 10^{-3}}{25 \cdot 10^{-6}} = 5,24 \frac{mA}{cm^2}$$

Then I_{SC} has registered a growth of 4.6 A/cm² in process P2 (value close to three times I_{SCP1}), and I_{mp2} is even almost four times greater than the same value obtained with process P1. The results are not still optimal, but the improvements achieved are outstanding.

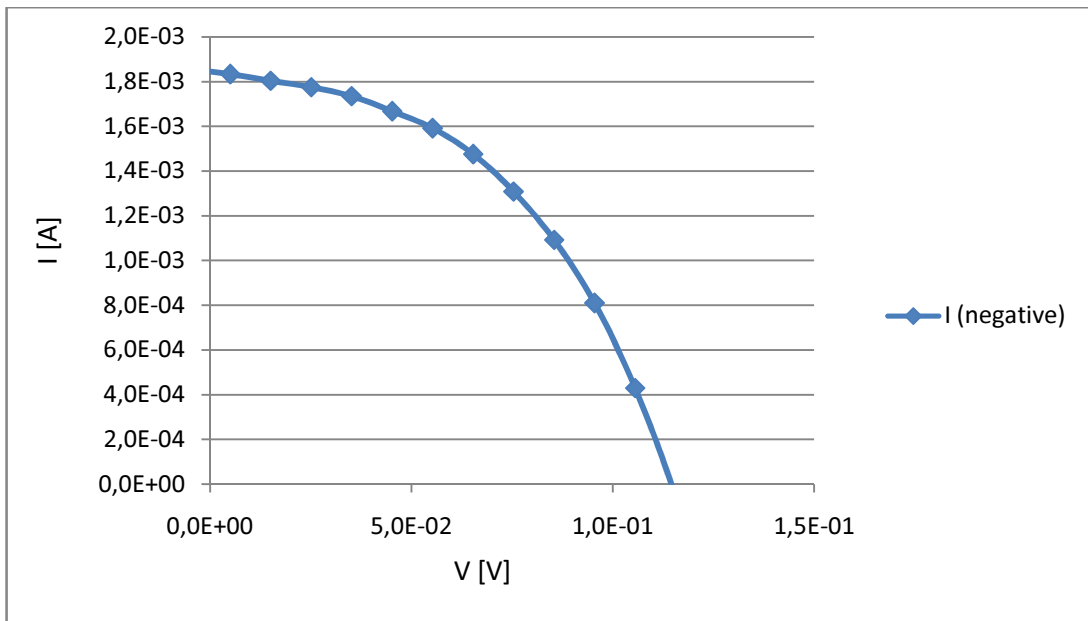


Figure 4.26: I-V characteristic of illuminated P2 cell.

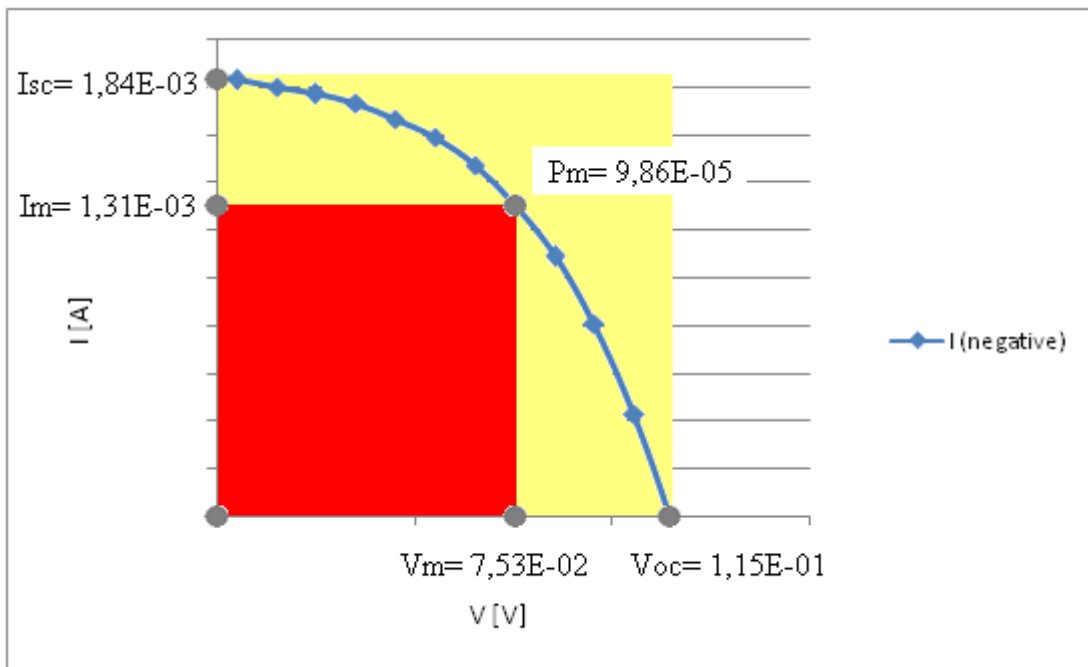


Figure 4.27: I-V characteristic and main parameters of P2 cell.

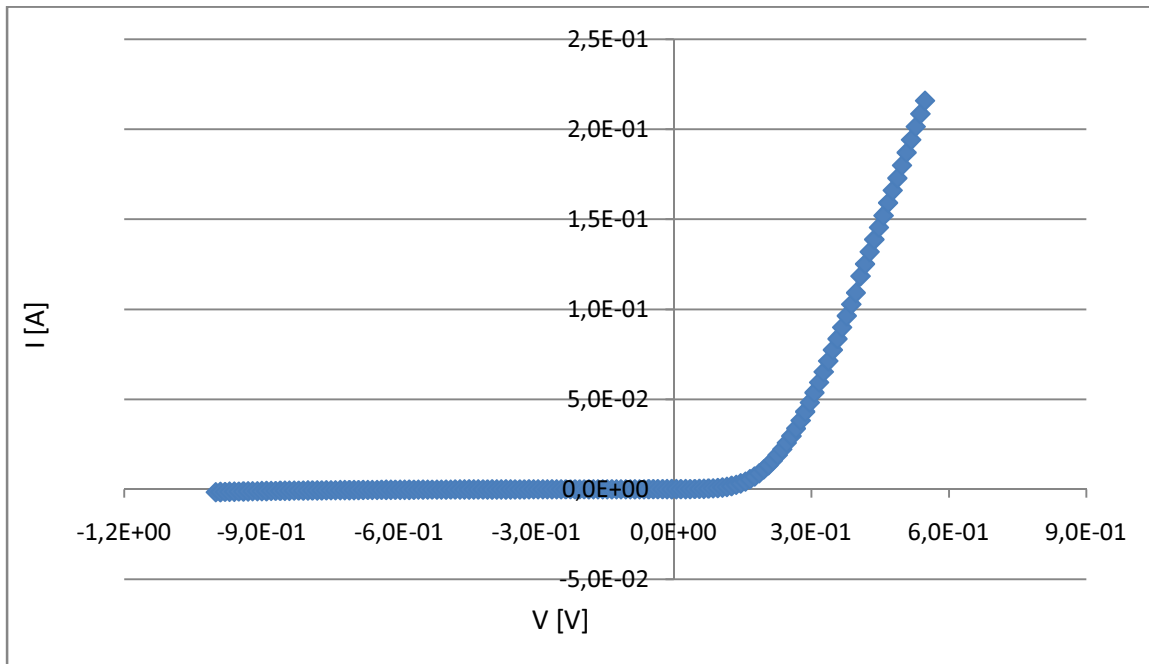


Figure 4.28: dark I-V characteristic of P2 cell.

In Figure 4.28 it is shown the IV characteristic of P2 cell without light. Using equation (2.72) with $I_L=0$ (because we are studying the dark I-V characteristic) we obtain:

$$(4.19) \quad I_0 = \frac{I}{(e^{V/V_T} - 1)}$$

From the graph of Figure 4.27 for $V=1,15 \cdot 10^{-1}$ V, $I=1,28 \cdot 10^{-3}$ A so that we obtain:

$$I_0 = \frac{1,28 \cdot 10^{-3}}{(e^{0,115/0,025} - 1)} = 12,99 \cdot 10^{-6} \text{ A} \approx 13 \mu\text{A}$$

With $V_T=0,025$ V (thermal voltage). Calculating the same value from the light characteristic (for proving the correctness of our calculation), considering equation (2.86), for $V=V_{OC}$ and then $I=0$, we have:

$$(4.20) \quad I_0 = \frac{I_{SC}}{(e^{V_{oc}/V_T} - 1)}$$

Substituting:

$$I_0 = \frac{I_{SC}}{(e^{V_{oc}/V_T} - 1)} = \frac{1,84 \cdot 10^{-3}}{(e^{0,115/0,025} - 1)} \approx 18 \mu\text{A}$$

The I_0 values are really close so we can consider right an I_0 value of about 15 μA .

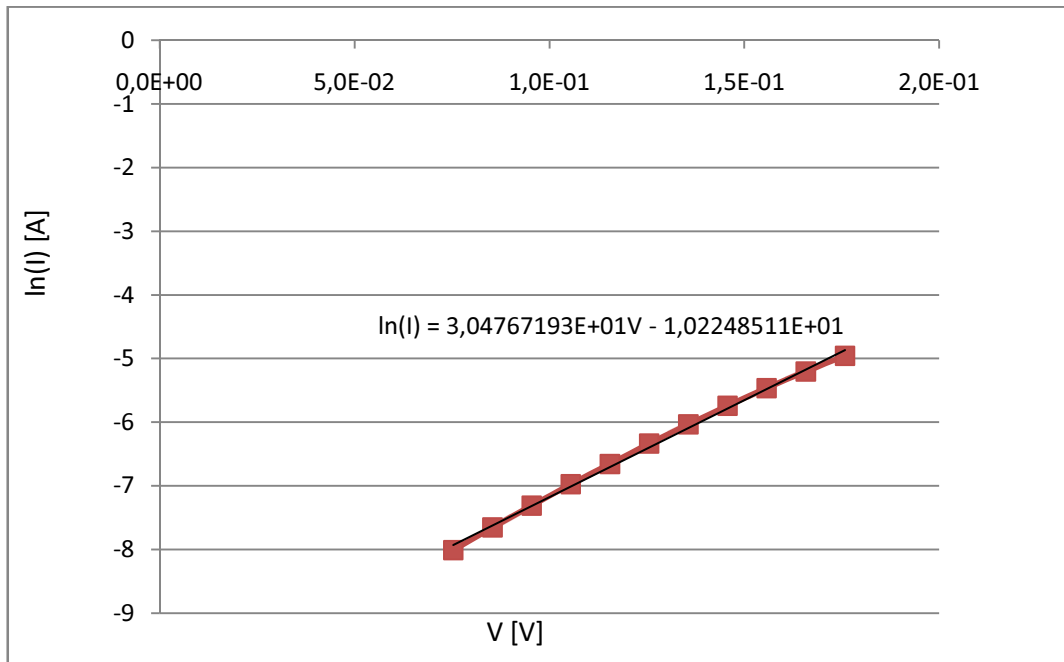


Figure 4.29: dark $\ln(I)$ - V characteristic of P2 cell.

In order to calculate the ideality factor we plot $\ln(I)$ (of the dark characteristic) as reported in Figure 4.29. In fact we have:

$$(4.21) \quad I = I_0 \left(e^{\frac{V}{nV_T}} - 1 \right)$$

And calculating $\ln(I)$ we obtain:

$$(4.22) \quad \ln(I) = \ln(I_0) + \ln\left(e^{\frac{V}{nV_T}} - 1\right) \approx \ln(I_0) + \frac{V}{nV_T}$$

So that, using the equation of the curve of Figure 4.29 we have:

$$\ln(I) = \ln(I_0) + \frac{V}{nV_T} = -10,22 + 30,47 V$$

$$\frac{V}{nV_T} = 30,47 V \rightarrow n = \frac{1}{30,47V_T} = \frac{1}{30,47 \cdot 0,025} = 1,31$$

The value of the ideality factor is then 1,33.

We can now compare the natural logarithm of the previously calculated I_0 value with the value obtained from the graph of Figure 4.29 (we consider $I_0 = 18 \mu\text{A}$).

$$\ln(I) = \ln(18 \cdot 10^{-6}) = -10,9$$

That is really close to the first side of the equation reported in Figure 4.29.

From equation (2.93), considering $I=0$ we obtain:

$$(4.23) \quad 0 = -I_0 \left(e^{\frac{V+I R_S}{V_T}} - 1 \right) + I_L - \frac{I R_S + V}{R_{sh}}$$

But for $I=0$, $V=V_{OC}$ and V_{OC} do not depend on R_S ($I \cdot R_S=0$); taking it into account equation (4.23) becomes:

$$(4.24) \quad 0 = -I_0 \left(e^{\frac{V_{OC}}{V_T}} - 1 \right) + I_L - \frac{V_{OC}}{R_{sh}}$$

And isolating R_{sh} :

$$(4.25) \quad R_{sh} = \frac{V_{OC}}{I_L - I_0 \left(e^{\frac{V_{OC}}{V_T}} - 1 \right)}$$

Considering the values of Figure 4.27 (light characteristic I-V of P2 cell):

$$R_{sh} = \frac{V_{OC}}{I_L - I_0 \left(e^{\frac{V_{OC}}{V_T}} - 1 \right)} = \frac{0,15}{1,84 \cdot 10^{-3} - 4,29 \cdot 10^{-6} \left(e^{\frac{0,15}{0,025}} - 1 \right)} = 1320 \Omega$$

That is a good value for R_{sh} . To calculate R_S we consider equation (2.86) without light ($I_L=0$) for $I=-I_{SC}$:

$$(4.26) \quad -I_{SC} = -I_0 \left(e^{\frac{V - I_{SC} R_S}{V_T}} - 1 \right)$$

$-I_{SC} = -1,84 \cdot 10^{-3} \text{A}$ and for that value the voltage is equal to 0.120 V (graph of the dark I-V curve). Substituting equation (4.20) in equation (4.26) we obtain:

$$(4.27) \quad I_{SC} = \frac{I_{SC}}{\left(e^{V_{OC}/V_T} - 1 \right)} \left(e^{\frac{V - I_{SC} R_S}{V_T}} - 1 \right)$$

And neglecting -1 within the round brackets it becomes:

$$(4.28) \quad e^{V_{OC}/V_T} = e^{\frac{V - I_{SC} R_S}{V_T}}$$

Calculating the natural logarithm of the both sides we obtain:

$$(4.29) \quad \frac{V_{OC}}{V_T} = \frac{V - I_{SC} R_S}{V_T}$$

And isolating R_S :

$$(4.30) \quad R_s = \frac{V - V_{OC}}{I_{SC}}$$

And substituting the $I_{SC}=1,84 \cdot 10^{-3} \text{A}$, $V=0,12 \text{V}$ and $V_{OC}= 0.115$ we can finally calculate the R_s value:

$$R_s = \frac{0,120 - 0,115}{1,84 \cdot 10^{-3}} = 2,71 \Omega$$

Figure references chapter 4

Figures 4.2 is from [28];

Figures 4.3 is from [32];

Figures 4.10, 4.11, 4.12, 4.13 are from [14].

5.

CONCLUSIONS AND DISCUSSION ABOUT POSSIBLE FURTHER DEVELOPMENTS

In the present work we have reported about the fabrication process of Metal-Semiconductor solar cells obtained through the ITO deposition on a p-GaAs(100) substrate. In particular we divided the work in two main parts: the single phase process development and entire process tests. Main conclusions obtained regarding the single phase process development are the following :

- Concerning the first part of our work, we have carried out different ITO depositions on a glass substrates to study the ITO behavior in terms of resistivity and transmittance. We have seen that the resistivity value strongly depend on the deposition power (higher the power, lower the resistivity), but also on the deposition temperature and distance: at 150°C

the resistivity resulted to be lower, as well as for depositions made with lower distances between target and substrate. Despite the higher power and lower distance depositions seem to give better results in terms of resistivity, a compromise must be found because they can bring also bigger damage at the ITO-GaAs interface. A similar observation can be given about the temperature; in fact, despite it come out that 150°C depositions result in lower resistivity values than room temperature depositions, high temperatures (such as 150°C) can lead to interfacial stress and to chemical changes in the ITO composition, badly affecting the solar cell efficiency.

- However, good resistivity values can be reached just bringing the sputtering camera at low pressure ($\leq 4 \cdot 10^{-6}$ mbar) for low power depositions. As the ITO covering thickness is of crucial importance, and as it is assumed to be optimal for values close to 100 nm, from our fabrications and experimental measurement come out that the right time of deposition is about 15-20 minutes.
- Concerning the ITO transmittance, none of the deposition conditions seems to give particular problems, as the results show a good transmittance of the ITO covering for almost every deposition carried out (and, moreover, said transmittances really are similar between them).
- In the first phase of our work we also have studied the ohmic contact Zn-Au in GaAs substrate. In particular, we have been able to develop a new method of measurement, that is an evolution of the TLM, able to allow ohmic contact measurements also for contact made on thicker substrate (that is our case). The introduced evolution involves the use of a magnetic field parallel to the sample surface and perpendicular to the current direction, that have the scope to give to the carriers an equal distribution in the thickness direction for each pair of contacts (having different distance d_i) involved in the measurement process. Unlike the traditional TLM, introducing our evolution in the TLM the results show a linear $R_T - d$ figure (that is what we aspect to obtain). Therefore, we have been capable to

characterize our ohmic contact, in particular calculating the R_c value (2.28Ω), L_T ($1,37 \cdot 10^{-3} \text{m}$) and the contact resistivity ρ_c ($2.28 \cdot 10^{-6} \Omega \text{m}^2$).

The second phase of our work was about the whole process. Two different processes have been tested as base for further development. The first one (P1) involves the use of temperatures higher than 300 K after the ITO deposition, by reason of the lithography processes made on such ITO layer. The second process (P2) prevents the ITO covering from overheating avoiding the lithography steps, through the use of shadow masks. The results show better efficiency values for the solar cell made with P2. This is probably for the reasons reported above about the compositional changes in which ITO is involved when achieves high temperatures (in this case the 100°C achieved in the lithography step). Main conclusions obtained in this second phase are the following :

- The results about P1 and P2 show than that the right choice is to use room temperature processes.

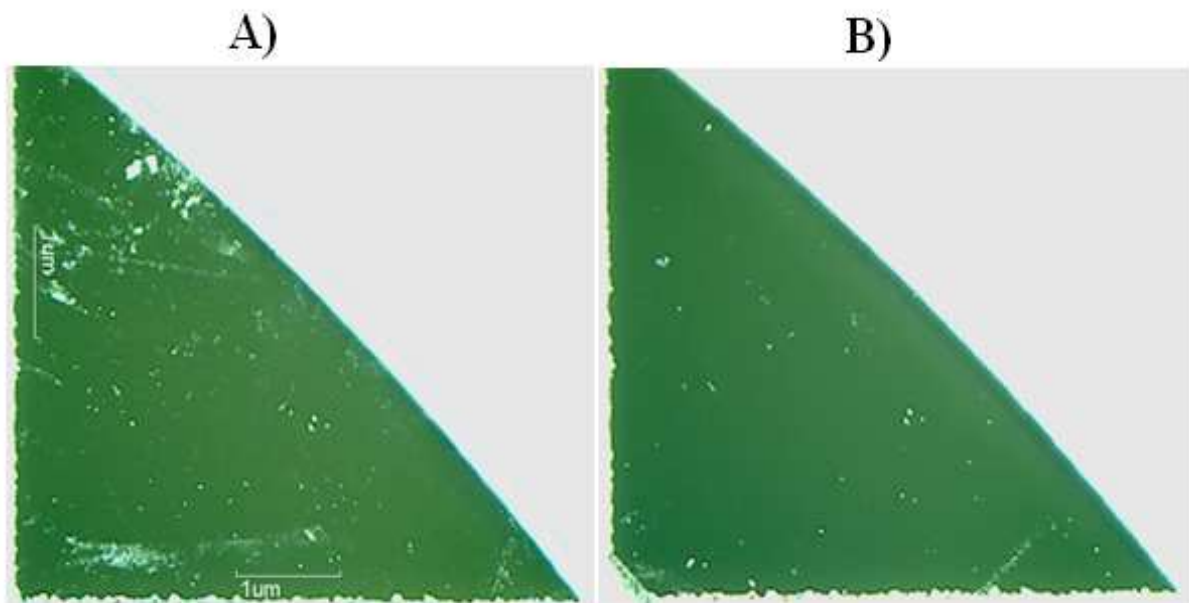


Figure 5.1: GaAs sample; A) before degreasing process; B) after degreasing process.

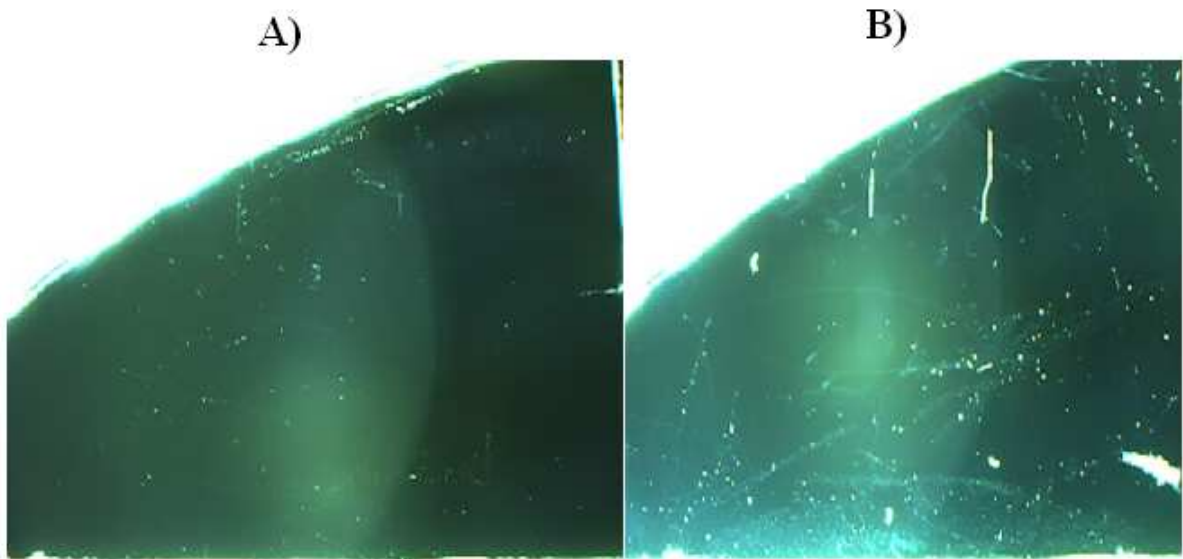


Figure 5.1: GaAs sample; A) before thermal annealing treatment (after degreasing); B) after thermal annealing treatment

- Considering P2 as main road for further development, the step in which is probably possible to work to raise the efficiency, is the cleaning and passivation treatment. In fact, as we have reported in section 4.5, passivation is of crucial importance for the GaAs technology, and then it has to be further investigated. About that, we have made a process including the passivation treatment of the GaAs substrate and such treatment actually gives an improvement of the solar cell characteristic but it was not substantial compared with P2 (for that reason we have not reported such results). So that more passivation processes with different conditions (about compositions, soaking time and temperatures) could be tested to finally improve considerably the solar cell characteristic.
- Beyond the passivation, also the surface degreasing is particular important. As reported in Figure 5.1, the decreasing process used in our process (10 minutes of Acetone with ultrasound, 10 minutes of Isopropanol with ultrasound, sample rinse in DI water, sample soaking in a solution of HF (5%) in water for 30 seconds), do not seem to lead to a completely clean surface.

Each particle remaining on the surface certainly create trap centers and lose of efficiency.

- Another problem of P2 is the thermal annealing. On one hand, doing it before the ITO deposition is of crucial importance by reason of the high temperature reached in this phase (400°C) certainly able to compromise the ITO quality but, on the other hand, do not make the ITO deposition immediately after the GaAs cleaning, brings to the formation of surface irregularity (together with the growth of low quality GaAs native oxide). As a matter of fact, Figure 5.2 shows that after the thermal annealing the surface seems to be covered by more particles than before such treatment; said particles will affect badly the ITO-GaAs interface quality. In this context, it seems to be really important to further develop the laser annealing, in order to avoid the thermal annealing and to deposit the ITO covering just after the cleaning (because the ITO layer is not subjected to high temperatures in laser treatment). Moreover, to increase the GaAs surface cleaning before the ITO deposition, an inverse sputtering process should be carried out on the sample. Despite it seems to be an aggressive treatment, Sheldon in [33] says that it brings to a considerably improvement of the solar cell efficiency, particularly raising the VOC.

Finally, we conclude considering that the best option is to use shadow masks for the sputtering deposition process at room temperature, with no thermal stress on the ITO covering (P2) introduced by the lithography process and, moreover, we believe that the cleaning and passivation treatment is the process phase that should be more investigated to obtain substantial improvement starting from the results of process P2.

References

- [1] W. Shockley, and H. J. Queisser, "Detailed Balance Limit of Efficiency of p-n Junction Solar Cells", *J. Appl. Phys.* 32(3), 510–519 (1961).
- [2] Antonio Luque and Antonio Martí, "The Intermediate Band Solar Cell: Progress Toward the Realization of an Attractive Concept", *Adv. Mater.* 22, 160–174 (2010).
- [3] Luis Castañer and Santiago Silvestre, "Modelling Photovoltaic Systems Using PSpice", John Wiley & Sons, (2002).
- [4] Web site: <http://www.ajaint.com/whatis.htm>.
- [5] G. Lullo, S. Riva Sanseverino, lecture note of "Dispositivi Elettronici", Univesità degli studi di Palermo, (2008).
- [6] Fabrizio Bonani, lecture note of "Dispositivi Elettronici Integrati", Politecnico di Torino, (2009).
- [7] Donald M. Mattox, "The Foundation of Vacuum Coating Technology" Noyes publications/William Andrew Publishing, (2003).
- [8] Web site: http://www.etafilm.com.tw/PVD_Thermal_Evaporation_Deposition.html
- [9] Web site: http://www.etafilm.com.tw/PVD_Sputtering_Deposition.html
- [10] David Artigas García, lecture note of "Laser", Universitat Politècnica de Catalunya, (2009).
- [11] C. Tablero, P. Wahnón, P. Palacios, J. J. Fernandez, "Diseño de nuevos materials fotovoltaicos de banda intermedia", *Bol. Soc. Esp. Ceram. V.*, 43 [2] 345-347 (2004).
- [12] Pablo Palacios, Perla Wahnón, Sara Pizzinato, José C. Conesa, "Energetics of formation of $TiGa_3As_4$ and $TiGa_3P_4$ intermediate band materials", *J. Chem. Phys.* 124, 014711 (2006).
- [13] Luis Castañer, lecture note of "Energia Solar Fotovoltaica", Universitat Politècnica de Catalunya, (2009).
- [14] Dieter K. Schroder, "Semiconductor Material and Device Characterization", John Wiley & Sons, (2006).

-
- [15] V. G. Bozhkov, N. A. Torkhov, I. V. Ivonin and V. A. Novikov, "Study of the Properties of the Surface of Gallium Arsenide by Scanning Atomic Force Microscopy", *Semiconductor*, 42(5), 531–539 (2008).
- [16] Yi Xuan, Hung-Chun Lin and Peide D. Ye, "Simplified Surface Preparation for GaAs Passivation Using Atomic Layer-Deposited High- κ Dielectrics", *IEEE Transactions on electron devices*, 54(8), 1811-1817 (2007).
- [17] T. Błachowicz, G. Salvan, D.R.T. Zahn, J. Szuber, "Micro-Raman spectroscopy of disordered and ordered sulfur phases on a passivated GaAs surface", *Applied Surface Science*, 252, 7642–7646 (2006).
- [18] S. Arabasz, E. Bergignat, G. Hollinger, J. Szuber, "XPS analysis of surface chemistry of near surface region of epitaxial GaAs(1 0 0) surface treated with $(\text{NH}_4)_2\text{S}_x$ solution", *Applied Surface Science* 252, 7659–7663 (2006).
- [19] V.L. Alperovich, O.E. Tereshchenko, N.S. Rudaya, D.V. Sheglov, A.V. Latyshev, A.S. Terekhov, "Surface passivation and morphology of GaAs(1 0 0) treated in HCl-isopropanol solution", *Applied Surface Science*, 235, 249–259 (2004).
- [20] Jun-Kyu Yang, Min-Gu Kang, Hyung-Ho Park, "Chemical and electrical characterization of $\text{Gd}_2\text{O}_3/\text{GaAs}$ interface improved by sulfur passivation", *J. Appl. Phys.*, 96(9), 4811-4816 (2004).
- [21] Elena V. Konenkova, "Modification of GaAs(1 0 0) and GaN(0 0 0 1) surfaces by treatment in alcoholic sulfide solutions", *Vacuum*, 67, 43–52 (2002).
- [22] T. P. Bekezina and G. M. Mokrousov "Preparation of GaAs Surfaces of Desired Composition", *Inorganic Materials*, 36(9), 857-863 (2000).
- [23] V. M. Botnaryuk, Yu. V. Zhilyaev, E. V. Konenkova, "Sulfide passivation of GaAs power diodes", *Semiconductors*, 33(6), 662-664 (1999).
- [24] O. E. Tereshchenko, S. I. Chikichev, A. S. Terekhov, "Composition and structure of HCl-isopropanol treated and vacuum annealed GaAs(100) surfaces", *J. Vac. Sci. Technol. A*, 17(5), 2655-2662 (1999).
- [25] Albert G. Baca and Carol I.H. Ashby, "Fabrication of GaAs devices", *Institution of Engineering and Technology*, London, United Kingdom, (2009).
-

-
- [26] A.V. Mudryi, A.V. Ivaniukovich, A.G. Ulyashin, "Deposition by magnetron sputtering and characterization of indium tin oxide thin films", *Thin Solid Films* 515, 6489–6492 (2007).
- [27] Radhouane Bel Hadj Tahar, Takayuki Ban, Yutaka Ohya, Yasutaka Takahashi, "Tin doped indium oxide thin films: Electrical properties", *J. Appl. Phys.*, 83(5), (1998).
- [28] Product data sheet, Indium Tin Oxide (ITO) $\text{In}_2\text{O}_3 : \text{SnO}_2$, Indium Corporation (2008).
- [29] R. C. Hayward, D. A. Saville & I. A. Aksay, "Electrophoretic assembly of colloidal crystals with optically tunable micropatterns", *Nature*, 404, 56-59 (2000).
- [30] E. Aperathitis, Z. Hatzopoulos, M. Androulidaki, V. Foukaraki, A. Kondilis, C.G. Scott, D. Sands, P. Panayotatos, "RF sputtered indium-tin-oxide as antireflective coating for GaAs solar cells", *Solar Energy Materials and Solar Cells*, 45, 161-168 (1997).
- [31] E. Kaminska, A. Piotrowska, E. Mizera, E. Dynowska, "Evolution of the microstructure of Au(Zn) metallization during formation of an ohmic contact to p-type GaAs", *Thin solid films*, 246, 143-150 (1994).
- [32] Web site: <http://pvcddrom.pveducation.org/CHARACT/4pp.HTM>.
- [33] P. Sheldon, R. E. Hayes, P. E. Russell, R. N. Nottenburg, K. A. Emery, P. J. Ireland, L. L. Kazmerski, "Evaluation of ITO/GaAs solar cells", *J. Vac. Sci. Technol.*, 20(3), 410-413 (1982).